

**Morphophysiological and Microcircuit Development of Hippocampal
Neurons in Type I Lissencephaly**

**Tyler Ekins
BS Brigham Young University, 2015**

A dissertation submitted in partial fulfillment of the requirements for the Degree of
Doctor of Philosophy in the Department of Neuroscience at Brown University

**Providence, RI
February 2021**

© Copyright 2020 by Tyler G. Ekins

**This dissertation by Tyler G Ekins is accepted in its present form
by the Department of Neuroscience as satisfying the
dissertation requirement for the degree of Doctor of Philosophy**

Date _____

Dr. Chris J McBain, Advisor _____

Recommended to the Graduate Council

Date _____

Dr. Claire Le Pichon, Reader _____

Date _____

Dr. Christopher Moore, Reader _____

Date _____

Dr. Timothy Petros, Reader _____

Date _____

Dr. Pablo Castillo, Outside Reader _____

Approved by the Graduate Council

Date _____

Dr. Andrew G. Campbell, _____

Dean of the Graduate school

CURRICULUM VITAE

- EDUCATION**
- Brown University** (Providence, RI) Defense date: Oct 2020
- Ph.D.: Neuroscience
 - Brown/NIH Graduate Partnership Program
 - GPA: 4.0
- Brigham Young University** (Provo, UT) April 2015
- B.S.: Neuroscience
 - Minor: Japanese
 - GPA: 3.51
- EXPERIENCE**
- Thesis Lab** (Chris McBain, NIH/NICHD) Summer 2016 - present
- Inhibitory interneuron morphophysiological development and microcircuit integration in a model of Type I lissencephaly
- Research Rotation** (Julie Kauer, Brown University) Spring 2016
- Molecular basis of transient long-term potentiation in the hippocampus
- Research Rotation** (Karla Kaun, Brown University) Fall 2015
- Alcohol-induced hyperactivity circuits in *drosophila melanogaster*
- Undergraduate Research Assistant** (Scott Steffensen, BYU) 2012 - 2015
- Influence of oxidative stress on methamphetamine-induced modulation of dopamine release
- SKILLS**
- Laboratory Skills**
- Cellular and synaptic neurophysiology
 - Pharmacology
 - Fast-scan cyclic voltammetry
 - Microsurgery
 - Immunohistochemistry
 - Confocal microscopy

PUBLICATIONS

“Emergence of Non-Canonical Parvalbumin-Containing Interneurons in Hippocampus of a Murine Model of Type I Lissencephaly” **Tyler G Ekins**, Vivek Mahadevan, Yajun Zhang, James D’Amour, Timothy Petros, Chris J McBain. *Under revision at eLife*. (Oct 2020)

“Linking epigenetic dysregulation, mitochondrial impairment, and metabolic dysfunction in SBMA motor neurons” Naemeh Pourshafie, Ester Masati, Eric Bunker, Alec R. Nickolls, Parisorn

Thepmankorn, Kory Johnson, Xia Feng, **Tyler Ekins**, Christopher Grunseich, and Kenneth H. Fischbeck. *JCI Insight*. 2020 Jul 9. DOI: [10.1172/jci.insight.136539](https://doi.org/10.1172/jci.insight.136539)

“Aberrant sorting of hippocampal complex pyramidal cells in Type I Lissencephaly alters topological innervation” James A D’Amour, **Tyler G Ekins**, Stuti Ghanatra, Xiaoqing Yuan, Chris J McBain. *eLife*. 2020 Jun 19. DOI: [10.7554/eLife.55173](https://doi.org/10.7554/eLife.55173)

“Paradoxical network excitation by glutamate release from VGlut3+ GABAergic interneurons” Kenneth A Pelkey, Daniela Calvigioni, Calvin Fang, Geoffrey Vargish, **Tyler G Ekins**, Kurt Auville, Jason C Wester, Mandy Lai, Connie Mackenzie-Gray Scott, Xiaoqing Yuan, Steven Hunt, Daniel Abebe, Qing Xu, Jordane Dimidschstein, Gordon Fishell, Ramesh Chittajallu, Chris J McBain. *eLife*. 2020 Feb 13. DOI: [10.7554/eLife.51996](https://doi.org/10.7554/eLife.51996)

“The role of reactive oxygen species in methamphetamine-taking behaviors and dopamine release in the nucleus accumbens” Eun Young Jang, David Hedges, Soo Pil Kim, Jun Yeon Lee, **Tyler Ekins**, Brandon Garcia, Hee Young Kim, Chae Ha Yang, Scott C Steffensen. *Addict Biol*. 2016 Jul 14. DOI: [10.1111/adb.12419](https://doi.org/10.1111/adb.12419)

POSTER PRESENTATIONS

“Morphophysiological development and microcircuit integration of parvalbumin-containing interneurons in a model of classical lissencephaly.” **Tyler Ekins**, Chris McBain. *GRC Inhibition 2019*.

“Parvalbumin-containing inhibitory neuron migration, morphology, and physiology is altered in Lis1 mutant mice.” **T.G Ekins**, C.J. McBain. *SfN 2018*.

“Who versus where: Effects of heterotopia on the development of cellular properties and connectivity of principal cells.” J.D. D’Amour, **T.G. Ekins**, C.J. McBain. *SfN 2018*.

“The impact of Lis1 hemizygous loss on parvalbumin-containing interneuron migration, development and function.” **T.G Ekins**, C.J. McBain. *GRC Synaptic Transmission 2018*.

“Investigation of hippocampal inhibitory interneurons in a model of Type I lissencephaly.” Cameron Paranzino, Ben Eisler, **Tyler Ekins**, Chris McBain. *NIH Summer Poster Day 2018*.

“Interneuron migration, development and function in Lis1 mutant mice.” **T.G. Ekins**, J.A. D’Amour, C.J. McBain. *SfN 2017*.

“Lissencephaly heterotopia and effects on the development of cellular microcircuitry.” J. D’Amour, **T.G. Ekins**, C.J. McBain. *SfN 2017*.

“Developmental characterization of hippocampal VGlut3-expressing interneurons.” C. Fang, **T. Ekins**, K. Auville, D. Calvigioni, R. Chittajallu, C.J. McBain. *SfN* **2017**.

“Lissencephaly heterotopia and effects on hippocampal microcircuitry.” James A. D’Amour, **Tyler G. Ekins**, Chris J. McBain. *NIH/NICHD Fellows Retreat* **2017**.

“Involvement of reactive oxygen species in methamphetamine-induced behavior changes and dopamine release in the nucleus accumbens.” Jang, E., Hedges, D.M., Nelson, A.C., Obray, D.J., **Ekins, T.G.**, Garcia, B.T., Kim, S.P., Lee, J.Y., Kim, N.J., Bitter, B., Song, K.M., Jang, S.J., Kim, H.Y., Heo, C.H., Yang, C.H., and Steffensen, S.C. *SfN* **2016**.

“The effect of reactive oxygen species scavengers in methamphetamine-taking behaviors and dopamine release in the nucleus accumbens.” E. Jang; S. P. Kim; D. M. Hedges; J. Y. Lee; **T. Ekins**; A. Perez; C. Freeman; A. Lamprecht; D. Bradshaw; H. Y. Kim; C. H. Yang; S. C. Steffensen. *SfN* **2015**.

“Basic Characterization of VGlut3-expressing interneurons in the hippocampus.” Kurt Auville, **Tyler Ekins**, Calvin Fang, Xiaoqing Yuan, Geoff Vargish, Ramesh Chittajallu, Ken Pelkey, and Chris McBain. *NIH Summer Poster Day* **2015**.

“Rapid adaptation of dopamine D2 receptors in the brain and blood following acute ethanol administration.” Eun Young Jang, Ryan J. Folsom, **Tyler G. Ekins**, Hyun Jung Park, Joseph R. Linzey, Jin Gyeom Lee, Chae Ha Yang, Hee Young Kim, Gregory F. Burton, Sandra Burnett, and Scott C. Steffensen. *SfN* **2014**.

ADDITIONAL EXPERIENCE AND AWARDS

NIH Summer intern mentoring (2018). Mentored two high school interns in immunohistochemistry and confocal microscopy experiments and analysis, and electrophysiology data analysis and interpretation.

NIH Neurobiology Interest Group Committee Member (2018). The Neurobiology Interest Group is a bimonthly seminar series for fellows and senior graduate students in the NIH to present well-developed projects.

NIH 2018 FARE Award Recipient. Project title: Hippocampal interneuron migration and inhibitory network organization in Lis1 mutant mice

BYU ORCA Award Recipient: Project title: Role of reactive oxygen species in methamphetamine modulation of dopamine release in the nucleus accumbens

Acknowledgments

This work would not have been possible without the great mentoring I received from Dr. Chris McBain. Chris gave me the opportunity of a lifetime. I couldn't be happier with every aspect of my experience in his lab. Chris was exactly the kind of mentor that I needed – he gave me freedom to figure things out for myself but was always there to help whenever I needed it. Throughout this entire journey I have had nothing but positive things to say about Chris, his mentorship style and the way he runs the lab.

One of the many benefits of doing research at the NIH is the ability to work directly with extraordinarily skilled full-time experimentalists. I was extremely lucky to receive training in whole-cell electrophysiology from one of the experts: Dr. Ken Pelkey, a staff scientist in the McBain lab. Through Ken's masterful teaching, I was able to learn patch-clamping with minimal stress and eventually accomplish much more than I thought possible. I also was fortunate to have many insightful conversations with and learn from Dr. Ramesh Chittajallu, another staff scientist in the McBain lab. I can't imagine a better environment to learn cellular and synaptic physiology. Many other members of the McBain lab have helped me through these past years, in particular, Dr. Jim D'Amour, a postdoctoral fellow in the lab. Jim brought the Type I lissencephaly mouse back to the McBain lab to reinvestigate and chapter 2 of this thesis is a publication resulting from our collaboration.

I want to thank Dr. Vivek Mahadevan, postdoc in the lab, for his amazing work on the single-nuclei RNA-seq analysis. During an extremely busy and stressful time, he was still able to make time for this project, for which I am truly thankful. I am grateful for the other exceptional members of the McBain lab that were essential to accomplishing this work. I thank Steve Hunt

for his indispensable work in genotyping and processing a large number of recorded cells for confocal microscopy. I thank former lab member Dr. Carolina Bengtsson-Gonzales for being kind enough to share her custom-designed code for unbiased cluster analysis, which catalyzed a major breakthrough in the way I thought about subtypes of PV+ interneurons and led to new experiments which are presented in chapter 3. I want to thank Daniel Abebe for his expertise with animal care, for helping me collect tails for genotyping and for always being so willing and able to help with everything and anything. I also want to thank other current and former members of the McBain lab for the great memories throughout my time at the NIH and for their direct and indirect help for this project: Xiaoqing Yuan, Connie MacKenzie-Gray Scott, Dr. Geoff Vargish, Dr. Jason Wester, Dr. Gulcan Akgul and Calvin Fang.

I thank my committee for their guidance and support: Dr. Tim Petros, Dr. Claire Le Pichon and Dr. Chris Moore. I am grateful to have always enjoyed meetings with you all! I thank Dr. Pablo Castillo for taking time out of his schedule to be the external examiner. I want to thank Tim Petros and Yajun Zhang for their expertise and for making possible the RNA-seq experiments. I also want to thank Tim for taking lots of time to meet with me throughout these years to discuss various science topics both related and unrelated to my thesis. I thank the Department of Neuroscience at Brown University and the NIH/Brown University Graduate Partnerships Program for accepting me and giving me this incredible opportunity. I also want to thank my undergraduate research advisor, Dr. Scott Steffensen for changing the trajectory of my career and I want to thank Dr. Jeff Edwards for encouraging me to apply to this program.

Finally, I thank my family for all of their support. My wife, Alison Snow, could not have been more supportive, and would constantly help by discussing this project, reading my writing,

looking at figures I made, listening to me practice presenting and much more. I am thankful to my parents for instilling a love of nature, science, and mystery from an early age. I could not have accomplished this without the help and support of so many people.

Table of Contents

Curriculum Vitae	iv
Acknowledgements	vii
List of Figures and Tables	xii
Chapter 1. Introduction to Inhibitory Interneurons, Microcircuits and Circuit Disorders	
1.1 Overview of inhibitory interneuron diversity and function	1
1.1.1 Developmental origins and cellular migration	1
1.1.2 Molecular markers	2
1.1.3 Cellular morphology	3
1.1.4 Action potential firing	6
1.1.5 Transcriptomics	7
1.1.6 Microcircuitry	8
1.1.7 Oscillations and network interactions	10
1.2 Disorders involving dysfunctional inhibition	12
1.2.1 Neurodegenerative disorders	12
1.2.2 Neurodevelopmental psychiatric disorders	13
1.2.3 Cortical malformation disorders	14
1.3 Project Overview	16
1.4 References	18
Chapter 2. Aberrant Sorting of Hippocampal Complex Pyramidal Cells in Type I Lissencephaly Alters Topological Innervation	
Abstract	26
Introduction	27
Results	30
Discussion	59
Materials and methods	66
Acknowledgements	74
References	74
Chapter 3. Emergence of Non-Canonical Parvalbumin-Containing Interneurons in Hippocampus of a Murine Model of Type I Lissencephaly	
Abstract	80
Introduction	81
Results and discussion	85
Conclusions	109
Methods	111
Acknowledgements	120
References	121
Chapter 4. Discussion	
4.0 Overview	138

4.1	The Type I lissencephaly mouse model as a proxy for the human condition.....	138
4.2	Impact of <i>LIS1</i> heterozygous loss on hippocampal lamination and connectivity.....	139
4.3	Characterization of PV+INT subtypes and emergence of IS cells.....	140
4.4	Synaptic transmission, depolarization block and implications for network dynamics and epileptiform activity.....	142
4.5	Outstanding questions and future directions.....	144
4.6	Conclusion.....	147
4.7	References.....	148

List of Figures & Tables

Chapter 1

Figure 1. Hippocampal interneuron subtypes.....	3
Table 1. Summary of murine models of brain malformation disorders.....	15

Chapter 2

Figure 1. Lis mutants display heterotopic banding and ectopic positioning of calbindin-expressing principal cells.....	33
Figure 2. Cellular birth-dating indicates ectopic calbindin cells in Lis mutants are the same late-derived embryologic population.....	36
Figure 3. Lis1-MUT calbindin-expressing PCs retain relatively complex morphologies....	41
Figure 4. Physiological properties of calbindin positive and negative morphological clusters.....	45
Figure 5. CCK-expressing basket cells have decreased innervation preference with ectopic calbindin-positive principal cells.....	49
Figure 6. Physiological assays of network function within CA1.....	54
Figure 7. Lis mutants display robust carbachol-induced oscillations.....	56
Figure 8. Carbachol oscillations in Lis1 mutants are less synchronous across CA1 heterotopias.....	58

Chapter 3

Figure 1. Cell-autonomous and non-autonomous effects of LIS1 heterozygous loss on radial migration of PV+INTs.....	86
Figure 2. Morphological reconstructions and firing profiles of WT/GlobalLis PV+INTs....	88
Figure 3. WT PV+INTs consist of two physiological subtypes: FS/NFS cells.....	92
Figure 4. GlobalLis PV+INTs consist of three physiological subtypes: FS/IS/NFS cells....	95
Table 1. Membrane, firing and morphological properties of PV+INTs.....	98
Figure 5. Connectivity and microcircuitry PV+INTs.....	100
Table 2. Unitary transmission properties by PV+INT subtype.....	101
Figure 6. Depolarization block in PV+INTs.....	104
Figure 7. Examination of LIS1 haploinsufficiency on PV+INTs using snRNAseq.....	108
Figure 2—Supplement 1. PV-TdTomato/PV-IHC colocalization.....	128
Figure 2—Supplement 2. Morphological analysis of PV+INT physiological subtypes....	129
Figure 3—Supplement 1. Cluster analysis and morphophysiology of EmxLis PV+INTs..	131
Figure 4—Supplement 1. Cluster analysis and morphophysiology of NkxLis PV+INTs...	133
Figure 4—Supplement 2. Membrane, firing, and morphological properties of PV+INT physiological subtypes.....	135
Figure 7—Supplement 1. Integrated analyses of single-cell/nucleus transcriptomes from PV+INTs from Lis1+/+, Lis1+/-, and reference datasets.....	136
Figure 7—Supplement 2. Annotation of PV+INT subtypes based on discrete marker gene expressions.....	137

Chapter 4

Figure 1. Spontaneous excitatory inputs to PV+INTs.....	146
--	------------

Chapter 1.

Introduction to inhibitory interneurons, microcircuits and circuit disorders

1.1 Overview of inhibitory interneuron diversity and function

Hippocampal and cortical networks are composed of two broad classes of neurons: excitatory pyramidal cells (PCs) which utilize the neurotransmitter glutamate and project between brain regions, and local circuit inhibitory interneurons which release the neurotransmitter *gamma*-aminobutyric acid (GABA). Despite representing only 10-15% of the total neuronal population in the hippocampus and cortex, GABAergic interneurons have remarkable diversity and are responsible for regulating essentially all aspects of neural circuit dynamics. Inhibitory interneuron classification is dependent on morphological, electrophysiological, biochemical and connectivity properties, and at least 15 distinct subtypes have been identified in the hippocampus (Pelkey et al., 2017).

1.1.1 Developmental origins and cellular migration

Inhibitory interneurons have a common origin in the developing ventral telencephalon (Anderson et al., 1997; Pelkey et al., 2017). On embryonic days 9-16, hippocampal interneurons are generated from progenitors in the medial ganglionic eminence (MGE) and caudal ganglionic eminence (CGE; Tricoire et al., 2011). After neurogenesis, interneurons engage in tangential migration to reach their cortical or hippocampal destinations, navigating through numerous of cellular environments and interacting with many diffusible and contact-dependent cues which influence their development (Petros & Anderson, 2013). Tangentially migrating interneurons

follow two different migratory streams: the marginal zone and the intermediate/subventricular zone. Upon arrival in their cortical or hippocampal destination, interneurons exit these streams and migrate along radial glial cells (radial migration) to reach their target laminar position (Petros & Anderson, 2013).

Cellular migration is a dynamic process involving cycles of rapid extension and retraction of a guidance-cue sensitive leading process followed by nucleokinesis (Petros & Anderson, 2013). This process of microtubule remodeling requires coordinated interactions of microtubules with dynein and microtubule-associated proteins such as LIS1, Ndel1, and Dcx (Tsai and Gleeson, 2005). Consequently, mutations to genes coding for these and related proteins cause neuronal migration and neurodevelopmental disorders (Kato & Dobyns, 2003).

1.1.2 Molecular markers

Molecular markers provide a convenient way to genetically identify types of neurons. MGE-derived interneurons express Nkx2.1 and subtypes of these cells have relatively unique expression patterns of molecules such as parvalbumin (PV), somatostatin (SST), calretinin (CR), calbindin (CB), and neuronal nitric oxide synthase (nNOS). CGE-derived interneurons express 5-HT3aR and subsets of these cells express cholecystokinin (CCK), vesicular glutamate transporter 3 (VGLUT3), vasoactive intestinal peptide (VIP), neuropeptide Y (NPY), CR, or reelin (Pelkey et al. 2017; Lim et al., 2018; Harris et al., 2018). These and other molecular markers have been utilized

to generate genetic lines to selectively target and manipulate subtypes of neurons in mice.

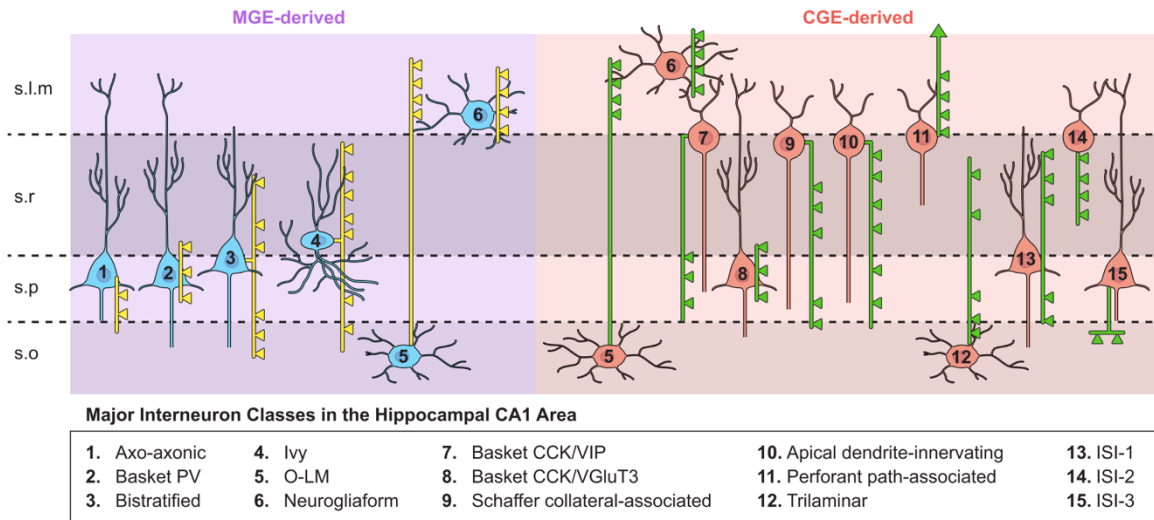


Figure 1. Hippocampal interneuron subtypes. Schematic representation of hippocampal interneuron subtypes highlighted in this review. In-terneuron subtypes are parsed according to origin within the medial ganglionic eminence (MGE) or caudal ganglionic eminence (CGE). Cells with dual origins are represented in both cohorts. Somato-dendritic profiles are represented in uniform color (blue for MGE, red for CGE). Thinner axon trajectories are illustrated in yellow (MGE-derived cells) and green (CGE-derived cells) with boutons (triangles) illustrating the dominantly targeted domains of CA1 pyramidal cells innervated by each interneuron subtype (From Pelkey et al., 2017).

1.1.3 Cellular morphology

In contrast to the relatively uniform pyramidal cells (PCs), interneurons have a remarkable diversity of forms. Interneurons inhabit and send dendrites and axons throughout all of the layers of the hippocampus (Pelkey et al., 2017). Hippocampal interneurons have been historically characterized by a combination of axonal and dendritic morphology. A brief overview of the main hippocampal interneuron morphological subtypes follows.

Axo-axonic (or chandelier) cells selectively innervate the axon initial segment of PCs. Axo-axonic cells are MGE-derived and express the calcium-binding protein PV. These cells predominately reside in or close to stratum pyramidale s.p. and have typically dendrites spanning

all hippocampal layers (Pawelzik et al., 2002; Pelkey et al., 2017). An additional subset of these cells residing in stratum oriens (s.o.) have horizontally oriented dendrites (Ganter et al., 2004).

Basket cells are named for the “basket”-like structure made by innervating the perisomatic region of PCs. Basket cells arise from progenitors in both the MGE and CGE. The MGE cohort express PV and mainly reside in s.o. and s.p. CGE-derived basket cells express CCK (with a subset co-expressing VGlut3) and are frequently found in s.p. and stratum radiatum (s.r.; Armstrong & Soltesz, 2012; Pelkey et al., 2017). PV+ and CCK+ basket cells differ in their action potential firing patterns and synaptic transmission dynamics due to differences in ion channel expression (discussed in the following sections).

Bistratified cells are the third morphological type of PV-expressing hippocampal interneuron. The majority of these cell bodies are found in s.o. and s.p. while dendrites normally span from s.o. to s.r., however, there are bistratified cells found in the deeper regions of s.o. with horizontal dendritic trees confined to this layer (Maccaferri et al., 2000; Pelkey et al., 2017). Bistratified cell axons have characteristic morphology extensively ramifying in s.r. and s.o. and avoiding s.p., innervating PC apical and basal dendrites but avoiding cell bodies (Pawelzik et al., 2002; Muler & Remy, 2014). In contrast to PV+ axo-axonic and basket cells, bistratified cells co-express SST and NPY (Pelkey et al., 2017).

Oriens-Lacunosum moleculare (O-LM cells) are named for their characteristic morphology with cell bodies and dendrites confined to s.o. and axons projecting to and ramifying in stratum lacunosum moleculare (s.l.m.), connecting with distal dendrites of PCs (McBain et al., 1994; Pelkey et al., 2017). A small percentage (~10%) of O-LM cell axons innervate other interneurons residing in s.o., near the s.r./s.l.m. border and in s.l.m. (Muler & Remy, 2014; Pelkey et al., 2017).

O-LM cells frequently express SST and reelin, and some express low levels of PV (MGE-marker), while others express the 5-HT_{3a} receptor (CGE-marker). Other molecular markers useful for identifying O-LM cells include mGluR1 α and Efn1 (Muler & Remy, 2014; Pelkey et al., 2017).

The CGE gives rise to at least three distinct subtypes of CCK-expressing, dendrite targeting interneurons: Schaffer collateral-associated cells, apical dendrite targeting interneurons, and perforant path-associated interneurons. Schaffer collateral-associated cells provide inhibitory input to balance the excitatory input from CA3 by synapsing onto PC apical and basal dendrites (Pawelzik et al., 2002; Ali, 2007). Axons of apical dendrite targeting interneurons are morphologically similar to Schaffer collateral associated cells, however they avoid PC basal dendrites and do not collateralize in s.o. or s.p. (Klausberger et al., 2005). Perforant path-associated interneurons send their axon to s.l.m., synapsing on the most distal portions of PC apical dendrites, as well as cross over the hippocampal fissure to innervate granule cells in the dentate gyrus (Pawelzik et al., 2002; Klausberger et al., 2005; Pelkey et al., 2017).

Neurogliaform cells are named for their small round cell bodies and short dendrites, resembling glial cells. They are mostly found in s.l.m., but a smaller number of these cells can be found at the s.r./s.l.m. border and in s.r. (Tricoire et al., 2010; Armstrong et al., 2012). Axons of neurogliaform cells completely envelop the cell body and dendrites in a dense cloud spread from superficial s.r. to the molecular layer of the dentate gyrus (Price et al., 2005; Tricoire et al., 2010). Contrasting to the other morphological type of interneurons with subcompartment-specific targeting, neurogliaform cells make a large number of en passant boutons without direct postsynaptic targets, enabling bulk neurotransmitter release (Pelkey et al., 2017). Molecular expression profiles of neurogliaform cells are less clear than other interneuron subtypes, with

neurogliaform cells expressing combinations of markers such as NPY, reelin, nNOS, COUPTF2, CR, CCK, and SST and CB (Price et al., 2005; Tricoire et al., 2010; Pelkey et al., 2017).

Ivy cells are named for their dense network of thin axons, which predominately innervate basal dendrites of PCs in s.o. (Fuatealba et al., 2008). The majority of ivy cells bodies and dendrites are found from s.o. to s.r., with the highest density in s.p. Both dendrites and axons of ivy cells are similar to those of neurogliaform cells, however ivy cells often have dendrites that extend beyond their axonal arbors (Tricoire et al., 2010; Pelkey et al., 2017). The molecular expression profiles of ivy cells are similar neurogliaform cells including NPY, nNOS, and COUPTF2, but not reelin (Tricoire et al., 2010; Armstrong et al., 2012; Pelkey et al., 2017).

Most interneuron connections are with PCs and other interneurons of the same subtype, however there are at least three identified morphological subtypes of hippocampal interneuron-selective interneurons (ISIs): ISI-1, ISI-2, and ISI-3. These cells selectively express CR (ISI-1), VIP (ISI-2), or both CR and VIP (ISI-3), and selectively inhibit different types of interneurons throughout the hippocampal subfield, providing various forms of disinhibition to hippocampal circuits (Gulyas et al., 1996; Tyan et al., 2014; Pelkey et al. 2017).

1.1.4 Action potential firing

Interneurons differ in their compositions of ion channels and associated proteins, which interact to create a diverse landscape of physiological properties. Patterns of action potential firing in response to current injections have been extensively used to classify subtypes of neurons including categories such as fast-spiking, late-spiking, and regular-spiking.

The “fast-spiking” phenotype refers to the pattern of repetitive action potential firing at high frequencies (>100 Hz) with minimal spike-frequency adaptation/accommodation and requires expression of the Kv3 subfamily of voltage-gated potassium channels (Rudy and McBain, 2001; Pelkey et al., 2017). Kv3 channels are activated when neurons are depolarized to above -20 mV and play a key role in keeping action potentials short through rapid membrane potential repolarization (Rudy and McBain, 2001). In the hippocampus, the fast-spiking pattern is found in the PV-expressing axo-axonic, basket and bistratified cells (Tricoire et al., 2011; Pelkey et al., 2017).

Neurogliaform and ivy cells frequently exhibit a “late-spiking” phenotype. In response to a sustained depolarizing input, these cells continually increase membrane voltage for several hundred milliseconds before initiating action potentials (Tricoire et al., 2010). These cells have low amplitude action potentials with large afterhyperpolarization amplitudes, and often have an “accelerating” pattern of action potential firing, with inter-spike-interval decreasing over time (Tricoire et al., 2010; Tricoire et al., 2011).

Many other types of interneurons including SST+ and CCK+ cells have a “regular-spiking” firing pattern (Pawelzik et al., 2002; Tricoire et al., 2011). Regular-spiking cells have a characteristic accommodating/adapting (decelerating) pattern of discharging action potentials over time and typically fire no faster than 50 Hz (Pelkey et al., 2017).

1.1.5 Transcriptomics

Advances in transcriptomics, in particular the emergence of single-cell RNA-sequencing (scRNA-seq), allow automated quantification of genome-wide gene expression in large populations of

individual neurons. Enormous diversity in transcriptomic clustering of interneuron subtypes has been revealed through scRNA-seq (Tasic et al., 2018). Recent studies have combined scRNA-seq with morphology and physiology to allow comprehensive characterization of morpho-electric-transcriptomic neuronal subtypes and at least 20 distinct subtypes of cortical interneurons were identified (Gouwens et al., 2020). Beyond classification, single-cell transcriptomics can be used to identify molecular disruptions to subtypes of cells in disease conditions (Hook et al., 2018; Brenner et al., 2020; Zhang et al., 2020). snRNA-seq is a complex topic and will be discussed in more detail in chapter 3.

1.1.6 Microcircuitry

The morphophysiological diversity of inhibitory interneurons allows them to control all aspects of network dynamics, providing various forms of inhibition based on their connectivity. In addition to differences in subcompartment-specific targeting of PCs, interneurons further distinguish between PCs, preferentially connecting based on PC position, morphology, and axonal projection target. Subtypes of interneurons also differ in their presynaptic release properties and synaptic transmission dynamics during trains of action potentials (Pelkey et al., 2017).

PV-containing interneurons are equipped with synaptic release machinery such as P/Q-type calcium channels and synaptotagmin-2, enabling fast-acting and synchronous neurotransmitter release (Hefft & Jonas, 2005; Armstrong & Soltesz, 2012). During trains of action potentials, PV+ interneurons have short-term depression of neurotransmitter release (Hefft & Jonas, 2005; Kohus et al., 2016). Regional differences have been found between subtypes of PV+ interneurons such hippocampal basket cells, which have been shown to evoke

larger amplitude unitary inhibitory post synaptic currents (IPSPs) in deep PCs (relative to superficial PCs) and cortical PV+ basket cells, which have higher connectivity with and provide stronger inhibition to PCs with reciprocal excitatory connections (Lee et al., 2014, Yoshimura & Callaway, 2005).

Due to expression of N-type calcium channels, CCK+ interneurons release GABA with less precision and reliability than do PV+ cells (Armstrong & Soltesz, 2012). CCK+ cells have the property of a transmission from synchronous to asynchronous neurotransmitter release over trains of action potentials. Initially, neurotransmitter release is time-locked to the presynaptic action potential, however as the cell continues to fire GABA becomes randomly released and continues to do so for a short period of time after the firing subsides (Hefft & Jonas, 2005). CCK+ interneurons can have facilitating synapses, where the IPSC amplitude increases on successive pulses, however mildly depressing synapses are also observed (Hefft & Jonas, 2005; Savanthrapadian et al., 2013; Kohus et al., 2016).

While not as much work has been done on SST+ interneuron microcircuitry as on PV+ and CCK+ cells, some information has been gathered on their synaptic physiology through utilizing whole-cell recordings. During trains of action potentials, SST+ interneuron outputs can be either facilitating, depressing, or facilitating and then depressing. (Bartely et al., 2008; Savanthrapadian et al., 2013). In the cortex, a subtype of SST+ interneurons called Martinotti cells have been shown to mediate disynaptic inhibition between recurrently connected PCs in the cortex (Silberberg & Markham, 2007).

As mentioned earlier, the extremely dense axonal plexus of neurogliaform cells enables bulk transmission of GABA, providing nonspecific inhibition to neurons in range (Pelkey et al.,

2017). Unitary IPSCs from neurogliaform cells have slow rise and fall kinetics compared to IPSCs from PV+ interneurons (Szabadics et al., 2007). Contrasting other cell types, outputs from neurogliaform cells activate GABA_B receptors in addition to activating GABA_A receptors (Tamas et al., 2003). Similar to neurogliaform cell connections, paired recordings between ivy cell and PCs reveal unitary IPSCs with slow kinetics (Fuentelba et al., 2008).

1.1.7. Oscillations and network interactions

Synchronized firing of ensembles of neurons creates waves of electrical activity known as neuronal oscillations. Neuronal oscillations are often named by their frequency bands including slow oscillations (<1 Hz), theta oscillations (4-10 Hz), and gamma oscillations (30-90 Hz; Pelkey et al., 2017).

Gamma oscillations are commonly seen throughout the brain and are correlated with processes including memory storage and retrieval, spatial navigation, sensory binding, and working memory (Bartos et al., 2007; Pelkey et al., 2017). Gamma oscillations depend on GABAergic neurotransmission and can be blocked by GABA_AR antagonists (Pelkey et al., 2017). PV+ basket cells in particular have been implicated in generating gamma oscillations; however, this depends on the brain region, as CA3 PV+ basket cells have a strong preference for firing at the peak of gamma oscillations, while CA1 PV+ basket cells have no phase preference (Craig & McBain, 2015). Further evidence for the role of PV+ interneurons in gamma oscillations comes from optogenetic studies which demonstrated that activating (all subtypes of) PV+ interneurons drives gamma oscillations while inhibiting these cells impairs gamma activity (Sohal et al., 2009; Cardin et al., 2009).

Theta oscillations are present in the hippocampus during voluntary movements and REM sleep. Gamma oscillations are frequently nested within theta cycles, and optogenetic stimulation at theta frequencies can drive gamma activity (Butler et al., 2016). Theta oscillations are dependent on activity of both excitatory and inhibitory neurons (Pelkey et al., 2017). Interneuron subtypes show remarkable similarity in their theta oscillation phase preferences: CA1 PV+ basket, axo-axonic, and CCK+ basket cells are phase-locked close to the peak of theta oscillations, while O-LM cells and bistratified cells fire at the trough (Klausberger et al., 2003; Klausberger et al., 2004; Klausberger et al., 2005).

Slow oscillations in the hippocampus are associated with sharp wave ripples and are present during both memory consolidation and slow-wave sleep. Slow oscillations cycle between “up-states” of synchronous activity and “down-states” of low activity. Slow oscillations can be generated directly in the cortex, but also emerge *in vivo* through thalamocortical interactions (Pelkey et al., 2017). During slow oscillations, PCs are strongly activated, and inhibitory interneurons have different firing rates depending on subtype and brain region. During up-states in the barrel cortex, PV+ interneurons are highly active, SST+ and VIP+ cells are moderately active, while NPY+ interneurons are silent (Neske et al., 2015). In medial entorhinal cortex up-states, PV+ cells have very high firing rates, other interneurons such as SST+ cells are weakly activated, and neurogliaform (NPY+ and NPY-) cells and VIP+ interneurons are silent (Tahvildari et al., 2012; Neske et al., 2015). *In vivo* studies in the prefrontal cortex have further analyzed the activity of subtypes of PV+ interneurons and found that basket cells fire at the onset of up-states and axo-axonic cells wait at least 200 ms after onset to fire (Massi et al., 2012).

1.2 Disorders involving dysfunctional inhibition

Dysfunctional inhibitory neurotransmission is implicated in many disorders of the nervous system including neurodevelopmental, neurodegenerative, and mood disorders, viruses and traumatic injury to the brain (Pelkey et al., 2017). Epileptiform activity is associated with many of these disorders, and “antiepileptic drugs” that influence inhibitory neurotransmission can often alleviate symptoms from seemingly diverse conditions such as chronic migraines, anxiety, dementia, bipolar disorder and schizophrenia (Smith et al., 2016; Zheng et al., 2017; Baldessarini et al., 2018; Benjamin et al., 2019). Mutations identified in human patients with such disorders are used to create animal models to investigate disruptions in great detail.

1.2.1 Neurodegenerative disorders

Neurodegenerative disorders can selectively damage populations of neurons. Alzheimer’s disease is a memory-eroding neurodegenerative disorder characterized by intracellular neurofibrillary tangles of phosphorylated tau protein and extracellular deposits of beta-amyloid plaques (Canter et al., 2016). Overexpression of amyloid precursor protein (APP) in an animal model of Alzheimer’s disease causes an overall increase in network excitability and reduces levels of the voltage-gated sodium channel Nav1.1, which is predominately expressed in PV+ interneurons (Verret et al., 2012; Wang et al., 2011). Human Alzheimer’s disease patients have an increased risk for seizures and mice over-expressing APP have disruptions in gamma oscillations and impaired cognitive functions (Palop & Mucke, 2009; Verret et al., 2012). Reductions of SST+ interneurons are observed in other models of Alzheimer’s disease such as mice overexpressing APP/PS1 (which also impacts NPY+ and CR+ cells), mice overexpressing

mutant tau (which also impacts PV+ cells), and mice expressing the human risk gene *ApoE4* (Pelkey et al., 2017).

Parkinson's Disease is the second most common neurodegenerative disease and the prognosis includes motor impairments, mood disorders, sleep disorders, and cognitive impairments including dementia (McGregor & Nelson, 2019). While degradation of midbrain dopamine neurons is considered the main cause of Parkinson's disease, there are also disruptions to inhibitory circuits, and human patients have an increased risk of epileptic seizures (Gruntz et al., 2018; Mallet et al., 2019). Parkinson's disease patients show reduction of SST in cerebrospinal fluid and a recent study found that induced pluripotent stem cells generated from human patients with *PARK2* mutations show reduction of SST+ cells (Iwasawa et al., 2019). Another recent study discovered that the dual cholinergic/GABAergic interneurons in the striatum are dependent on dopamine to provide inhibition, and this circuit is compromised in models of Parkinson's disease (Lozovaya et al., 2018).

1.2.2 Neurodevelopmental psychiatric disorders

Autism spectrum disorder (ASD) is an umbrella term for a large set of neurodevelopmental disorders with common symptoms including impaired social interaction and repetitive behavior patterns and is highly comorbid with epilepsy (Chattopadhyaya & Di Cristo, 2012). Post-mortem analysis of brain tissue from ASD patients show reduction in the GABA-synthesizing enzymes GAD65 and GAD67, as well as alterations in expression of GABA_A and GABA_B receptors (Chattopadhyaya & Di Cristo, 2012). Mouse models of ASD demonstrate a reduction of PV+ interneuron density in the cortex (Gogolla et al., 2009). In related disorders such as Rett

Syndrome and Fragile X Disease, mutations to different genes converge on a similar phenotype: imbalance between excitation and inhibition (Pelkey et al., 2017).

Schizophrenia is a complex disorder associated with delusion, paranoia, hallucination and psychosis, in addition to numerous cognitive and social deficits. While the heritability of schizophrenia is extremely high (80%) and numerous genes such as *DISC1*, *Neuregulin1*, and *COMT* have been proposed to play key roles, no consensus has been reached on the genetic causes of schizophrenia (Pelkey et al., 2017). Despite the genetic underpinning of schizophrenia remaining elusive, there are clear disruptions to inhibitory circuits. Lower expression of GAD67 has been observed in subtypes of neurons in brains of schizophrenic patients (Volk et al., 2000). Specific disruptions to subtypes of neurons have also observed including reductions in the neuronal marker CB in various brain regions (Beasley et al., 2002; Cotter et al., 2002; Chance et al., 2005). Studies on PV expression show mixed results: some studies identified no changes and others found a decrease in PV+ immunostaining in schizophrenic patients, including one study which found a large reduction of PV density in the hippocampus, the interneuron subtype with the highest expression of GAD67 (Zhang & Reynolds, 2001; Cotter et al., 2002; Beasley et al., 2002). Many studies have found disrupted gamma oscillations in schizophrenic patients, again implicating deficient PV+ interneuron inhibition (Williams & Boksa, 2010).

1.2.3 Cortical malformation disorders

Cortical malformation disorders primarily arise from abnormal cell proliferation and abnormal neuronal migration and are a common cause of epilepsy (Barkovich et al., 2015). Although rodent

brains lack gyri, their brains have in models of human cortical malformation disorders have severe disruptions to structural organization and epileptic seizures, summarized in Table 1.

Mutation	Cortex mislamination	Hippocampus mislamination	Cerebellum mislamination	Seizures
LIS1	+	+	+	+
DCX	-	+	-	+
NDEL1	+	+(postnatal KO)	-	unknown
RELN	+	+	+	+
TISH	+	-	-	+
EML1	+	+	+	+
PTEN	+	+	+	+
TUBB2B	+	-	unknown	unknown
GPR56	+	-	+	unknown
CDK5RAP2	+	unknown	unknown	unknown
ASPM	+	+	+	unknown

Table 1. Summary of murine models of brain malformation disorders.

Mutations that reduce cell proliferation result in brain malformation disorders known as microcephalies. Microcephalies are often correlated with seizures, and deficits in inhibition have been observed in rodent models, such as fewer inhibitory inputs to PCs in *CDK5RAP2* mutants and a reduction of PV+ interneurons in *ASPM* mutant mice (Zaqout et al., 2018; Garrett et al., 2020). Genetic mutations and haploinsufficiencies that reduce cell proliferation can overlap with other neurodevelopmental disorders such as the *ARID1B* heterozygous mouse model of ASD, which has decreased proliferation of ganglionic eminence interneuron progenitors and reduction of interneuron density (Jung et al., 2017). Other models of cortical malformation disorders with aberrant proliferation include the telencephalic internal structural disorder (*TISH*) mutant rat, which results in cortical lamination deficits and epileptic seizures (Lee et al., 1997; Fitzgerald et al., 2011).

Neuronal migration disorders are a large subset of cortical malformation disorders and often arise from mutations to genes involved in cytoskeletal rearrangement such as *LIS1*, *DCX*, and *RELN*. Humans with *LIS1* and *DCX* mutations have lissencephaly-spectrum disorders including

lack of cortical gyrification, severely impaired cognitive and motor functions and drug-resistant epilepsy (Nosten-Bertrand et al., 2008; Guerrini & Parrini, 2010). Mouse models *LIS1* haploinsufficiency recapitulate many of the human symptoms including malformation of cortical structures, ectopic positioning of interneurons and electrographic seizures (Hirotsune et al., 1998; Fleck et al., 2000). Similarly, the reeler mutant mouse (*RELN* mutation) is associated with disrupted lamination of all cortical structures, mispositioning of inhibitory interneurons and epilepsy (Pascual et al., 2003; Patrylo et al., 2006). Unlike *LIS1* and *RELN* mutants, *DCX* mutant mice only have disrupted lamination of the hippocampus, but these mice also exhibit spontaneous seizures (Corbo et al., 2002; Nosten-Bertrand et al., 2008). Cell type-specific mutations and postmigratory neuronal development remain largely unexplored in cortical malformation disorders.

1.3 Project overview

One of the goals of modern neuroscience is to comprehensively characterize the landscape of neuronal types and subtypes, integrating information about molecular identity, cellular morphology, intrinsic physiology, connectivity and synaptic transmission dynamics, and to understand how these cells and circuits changes in disease conditions. The following projects focus on a murine model of Type I lissencephaly, one of the most severe neuronal migration/cortical malformation disorders (Wong & Roper, 2015). Previous work on murine models of Type I lissencephaly found that mutant mice have cortical, hippocampal and cerebellar lamination deficits, motor deficits, enhanced excitability, lower *in vitro* seizure threshold and spontaneous seizures *in vivo* (Hirotsutne et al., 1998; Paylor et al., 1999; Fleck et al., 2000;

Greenwood et al., 2009). Despite the wealth of information gathered on Type I lissencephaly, the cellular and circuit mechanisms driving the epileptiform activity remain unknown. This thesis aims to investigate the impact of *LIS1* haploinsufficiency and resulting neuronal migration deficits on the morphophysiological development and microcircuit formation of hippocampal CA1 neurons and the origin of epileptiform activity, with an emphasis on PV-containing inhibitory interneurons, through using a combination of genetics, immunohistochemistry, morphology, whole-cell electrophysiology, pharmacology, and transcriptomics.

Chapter 2 was done in collaboration with James D'Amour, a postdoctoral fellow in the McBain laboratory, and investigates the impact of lamination on microcircuit formation in subtypes of hippocampal PCs. We find a microcircuit deficit involving CCK+ interneurons and ectopic CB+PCs and find that *in vitro* gamma oscillations are less responsive to pharmacological inhibition of CCK+ interneurons in the *LIS1* mutant.

Chapter 3 is the majority of my thesis work and focuses specifically on PV+ interneuron morphophysiological development and microcircuit integration using global and cell type-specific *LIS1* mutations. I find that disruptions to *LIS1*-dependent intrinsic developmental programs within interneurons, rather than ectopic positioning or pyramidal cell disorganization, results in the emergence of non-canonical PV+ interneurons. Compared to standard fast-spiking cells, these non-canonical PV+ interneurons have physiological properties that render them less able to balance excitation in hippocampal networks, likely contributing to epileptic seizures.

1.4 References

- Ali, A. B.** (2007). Presynaptic inhibition of GABAA receptor-mediated unitary IPSPs by cannabinoid receptors at synapses between CCK-positive interneurons in rat hippocampus. *Journal of Neurophysiology*, *98*(2), 861–869. <https://doi.org/10.1152/jn.00156.2007>
- Anderson, S. A., Eisenstat, D. D., Shi, L., & Rubenstein, J. L. R.** (1997). Interneuron migration from basal forebrain to neocortex: Dependence on *Dlx* genes. *Science*, *278*(5337), 474–476. <https://doi.org/10.1126/science.278.5337.474>
- Armstrong, C., Krook-Magnuson, E., & Soltesz, I.** (2012). Neurogliaform and Ivy cells: A major family of nNOS expressing GABAergic neurons. *Frontiers in Neural Circuits*, *6*(MAY2012), 1–10. <https://doi.org/10.3389/fncir.2012.00023>
- Armstrong, C., & Soltesz, I.** (2012). Basket cell dichotomy in microcircuit function. *The Journal of Physiology*, *590*(4), 683–694. <https://doi.org/10.1113/jphysiol.2011.223669>
- Baldessarini, R. J., Tondo, L., & Vázquez, G. H.** (2019). Pharmacological treatment of adult bipolar disorder. *Molecular Psychiatry*, *24*(2), 198–217. <https://doi.org/10.1038/s41380-018-0044-2>
- Bartley, A. F., Huang, Z. J., Huber, K. M., & Gibson, J. R.** (2008). Differential activity-dependent, homeostatic plasticity of two neocortical inhibitory circuits. *Journal of Neurophysiology*, *100*(4), 1983–1994. <https://doi.org/10.1152/jn.90635.2008>
- Beasley, C. L., Zhang, Z. J., Patten, I., & Reynolds, G. P.** (2002). Selective deficits in prefrontal cortical GABAergic neurons in schizophrenia defined by the presence of calcium-binding proteins. *Biological Psychiatry*, *52*(7), 708–715. [https://doi.org/10.1016/S0006-3223\(02\)01360-4](https://doi.org/10.1016/S0006-3223(02)01360-4)
- Benjamin, S., Williams, J. W., Cotton, C., Tung, J., An, H., Sanger, S., & Ho, J. M. W.** (2019). Anticonvulsants for behavioral and psychological symptoms in dementia: Protocol for a systematic review. *Systematic Reviews*, *8*(1), 1–7. <https://doi.org/10.1186/s13643-019-1025-5>
- Brenner, E., Tiwari, G. R., Kapoor, M., Liu, Y., Brock, A., & Mayfield, R. D.** (2020). Single cell transcriptome profiling of the human alcohol-dependent brain. *Human Molecular Genetics*, *29*(7), 1144–1153. <https://doi.org/10.1093/hmg/ddaa038>
- Butler, J. L., Mendonça, P. R. F., Robinson, H. P. C., & Paulsen, O.** (2016). Intrinsic cornu ammonis area 1 theta-nested gamma oscillations induced by optogenetic theta frequency

stimulation. *Journal of Neuroscience*, 36(15), 4155–4169.
<https://doi.org/10.1523/JNEUROSCI.3150-15.2016>

Canter, R. G., Penney, J., & Tsai, L. H. (2016). The road to restoring neural circuits for the treatment of Alzheimer's disease. *Nature*, 539(7628), 187–196.
<https://doi.org/10.1038/nature20412>

Cardin, J. A., Carlén, M., Meletis, K., Knoblich, U., Zhang, F., Deisseroth, K., ... Moore, C. I. (2009). Driving fast-spiking cells induces gamma rhythm and controls sensory responses. *Nature*, 459(7247), 663–667. <https://doi.org/10.1038/nature08002>

Chattopadhyaya, B., & Di Cristo, G. (2012). GABAergic circuit dysfunctions in neurodevelopmental disorders. *Frontiers in Psychiatry*, 3(MAY), 1–9.
<https://doi.org/10.3389/fpsy.2012.00051>

Corbo, J. C., Deuel, T. A., Long, J. M., LaPorte, P., Tsai, E., Wynshaw-Boris, A., & Walsh, C. A. (2002). Doublecortin is required in mice for lamination of the hippocampus but not the neocortex. *The Journal of Neuroscience : The Official Journal of the Society for Neuroscience*, 22(17), 7548–7557. <https://doi.org/22/17/7548> [pii]

Cotter, D., Landau, S., Beasley, C., Stevenson, R., Chana, G., MacMillan, L., & Everall, I. (2002). The density and spatial distribution of GABAergic neurons, labelled using calcium binding proteins, in the anterior cingulate cortex in major depressive disorder, bipolar disorder, and schizophrenia. *Biological Psychiatry*, 51(5), 377–386. [https://doi.org/10.1016/S0006-3223\(01\)01243-4](https://doi.org/10.1016/S0006-3223(01)01243-4)

Craig, M. T., & McBain, C. J. (2015). Fast Gamma Oscillations Are Generated Intrinsically in CA1 without the Involvement of Fast-Spiking Basket Cells. *Journal of Neuroscience*, 35(8), 3616–3624. <https://doi.org/10.1523/JNEUROSCI.4166-14.2015>

Fitzgerald, M. P., Covio, M., & Lee, K. S. (2011). Disturbances in the positioning, proliferation and apoptosis of neural progenitors contribute to subcortical band heterotopia formation. *Neuroscience*, 176, 455–471. <https://doi.org/10.1016/j.neuroscience.2010.12.003>

Fleck, M. W., Hirotsune, S., Gambello, M. J., Phillips-Tansey, E., Soares, G., Mervis, R. F., ... McBain, C. J. (2000). Hippocampal abnormalities and enhanced excitability in a murine model of human lissencephaly. *Journal of Neuroscience*, 20(7), 2439–2450.
<https://doi.org/10729324>

Fuentealba, P., Begum, R., Capogna, M., Jinno, S., Márton, L. F., Csicsvari, J., ... Klausberger, T. (2008). Ivy Cells: A Population of Nitric-Oxide-Producing, Slow-Spiking GABAergic Neurons and Their Involvement in Hippocampal Network Activity. *Neuron*, 57(6), 917–929.
<https://doi.org/10.1016/j.neuron.2008.01.034>

- Ganter, P., Szücs, P., Paulsen, O., & Somogyi, P. (2004).** Properties of horizontal axo-axonic cells in stratum oriens of the hippocampal CA1 area of rats in vitro. *Hippocampus*, *14*(2), 232–243. <https://doi.org/10.1002/hipo.10170>
- Garrett, L., Chang, Y. J., Niedermeier, K. M., Heermann, T., Enard, W., Fuchs, H., ... Hölter, S. M. (2020).** A truncating Aspm allele leads to a complex cognitive phenotype and region-specific reductions in parvalbuminergic neurons. *Translational Psychiatry*, *10*(1). <https://doi.org/10.1038/s41398-020-0686-0>
- Gogolla, N., LeBlanc, J. J., Quast, K. B., Südhof, T. C., Fagiolini, M., & Hensch, T. K. (2009).** Common circuit defect of excitatory-inhibitory balance in mouse models of autism. *Journal of Neurodevelopmental Disorders*, *1*(2), 172–181. <https://doi.org/10.1007/s11689-009-9023-x>
- Gouwens, N. W., Sorensen, S. A., Baftizadeh, F., Budzillo, A., Lee, B. R., Jarsky, T., ... Zeng, H. (2020).** Toward an Integrated Classification of Cell Types: Morphoelectric and Transcriptomic Characterization of Individual GABAergic Cortical Neurons. *BioRxiv*. <https://doi.org/10.2139/ssrn.3544405>
- Greenwood, J. S. F., Wang, Y., Estrada, R. C., Ackerman, L., Ohara, P. T., & Baraban, S. C. (2009).** Seizures, enhanced excitation, and increased vesicle number in Lis1 mutant mice. *Annals of Neurology*, *66*(5), 644–653. <https://doi.org/10.1002/ana.21775>
- Gruntz, K., Bloechliger, M., Becker, C., Jick, S. S., Fuhr, P., Meier, C. R., & Rüegg, S. (2018).** Parkinson disease and the risk of epileptic seizures. *Annals of Neurology*, *83*(2), 363–374. <https://doi.org/10.1002/ana.25157>
- Guerrini, R., & Parrini, E. (2010).** Neuronal migration disorders. *Neurobiology of Disease*, *38*(2), 154–166. <https://doi.org/10.1016/j.nbd.2009.02.008>
- Gulyás, A. I., Hájos, N., & Freund, T. F. (1996).** Interneurons containing calretinin are specialized to control other interneurons in the rat hippocampus. *Journal of Neuroscience*, *16*(10), 3397–3411. <https://doi.org/10.1523/jneurosci.16-10-03397.1996>
- Harris, K. D., Hochgerner, H., Skene, N. G., Magno, L., Katona, L., Bengtsson Gonzales, C., ... Hjerling-Leffler, J. (2018).** Classes and continua of hippocampal CA1 inhibitory neurons revealed by single-cell transcriptomics. In *PLoS Biology* (Vol. 16). <https://doi.org/10.1371/journal.pbio.2006387>
- Hefft, S., & Jonas, P. (2005).** Asynchronous GABA release generates long-lasting inhibition at a hippocampal interneuron–principal neuron synapse. *Nature Neuroscience*, *8*(10), 1319–1328. <https://doi.org/10.1038/nn1542>

- Hirotsune, S., Fleck, M. W., Gambello, M. J., Bix, G. J., Chen, a, Clark, G. D., ... Wynshaw-Boris, a.** (1998). Graded reduction of Pafah1b1 (Lis1) activity results in neuronal migration defects and early embryonic lethality. *Nature Genetics*, *19*(4), 333–339. <https://doi.org/10.1038/1221>
- Hook, P. W., McClymont, S. A., Cannon, G. H., Law, W. D., Morton, A. J., Goff, L. A., & McCallion, A. S.** (2018). Single-Cell RNA-Seq of Mouse Dopaminergic Neurons Informs Candidate Gene Selection for Sporadic Parkinson Disease. *American Journal of Human Genetics*, *102*(3), 427–446. <https://doi.org/10.1016/j.ajhg.2018.02.001>
- Iwasawa, C., Kuzumaki, N., Suda, Y., Kagawa, R., Oka, Y., Hattori, N., ... Narita, M.** (2019). Reduced expression of somatostatin in GABAergic interneurons derived from induced pluripotent stem cells of patients with parkin mutations. *Molecular Brain*, *12*(1), 1–8. <https://doi.org/10.1186/s13041-019-0426-7>
- Jung, E. M., Moffat, J. J., Liu, J., Dravid, S. M., Gurumurthy, C. B., & Kim, W. Y.** (2017). Arid1b haploinsufficiency disrupts cortical interneuron development and mouse behavior. *Nature Neuroscience*, *20*(12), 1694–1707. <https://doi.org/10.1038/s41593-017-0013-0>
- Karayannis, T., Elfant, D., Huerta-Ocampo, I., Teki, S., Scott, R. S., Rusakov, D. A., ... Capogna, M.** (2010). Slow GABA transient and receptor desensitization shape synaptic responses evoked by hippocampal neurogliaform cells. *Journal of Neuroscience*, *30*(29), 9898–9909. <https://doi.org/10.1523/JNEUROSCI.5883-09.2010>
- Kato, M., & Dobyns, W. B.** (2003). Lissencephaly and the molecular basis of neuronal migration. *Human Molecular Genetics*, *12*(REV. 1), 89–96. <https://doi.org/10.1093/hmg/ddg086>
- Klausberger, T., Magill PJ, Marton LF, Roberts JDB, Cobden PM, Buzsáki G, & P., S.** (2003). Brain-state- and cell-type-specific firing of hippocampal interneurons in vivo. *Nature*, *421*(6925), 844–848.
- Klausberger, T., Márton, L. F., Baude, A., Roberts, J. D. B., Magill, P. J., & Somogyi, P.** (2004). Spike timing of dendrite-targeting bistratified cells during hippocampal network oscillations in vivo. *Nature Neuroscience*, *7*(1), 41–47. <https://doi.org/10.1038/nn1159>
- Klausberger, T., Marton, L. F., O’Neill, J., Huck, J. H. J., Dalezios, Y., Fuentealba, P., ... Somogyi, P.** (2005). Complementary roles of cholecystikinin- and parvalbumin-expressing GABAergic neurons in hippocampal network oscillations. *Journal of Neuroscience*, *25*(42), 9782–9793. <https://doi.org/10.1523/JNEUROSCI.3269-05.2005>
- Kohus, Z., Káli, S., Rovira-Esteban, L., Schlingloff, D., Papp, O., Freund, T. F., ... Gulyás, A. I.** (2016). Properties and dynamics of inhibitory synaptic communication within the CA3 microcircuits of pyramidal cells and interneurons expressing parvalbumin or

cholecystokinin. *Journal of Physiology*, 594(13), 3745–3774.
<https://doi.org/10.1113/JP272231>

- Lee**, K. S., Schottler, F., Collins, J. L., Lanzino, G., Couture, D., Rao, A., ... Eisenman, L. (1997). A genetic animal model of human neocortical heterotopia associated with seizures. *Journal of Neuroscience*, 17(16), 6236–6242. <https://doi.org/10.1523/jneurosci.17-16-06236.1997>
- Lee**, S. H., Marchionni, I., Bezaire, M., Varga, C., Danielson, N., Lovett-Barron, M., ... Soltesz, I. (2014). Parvalbumin-positive basket cells differentiate among hippocampal pyramidal cells. *Neuron*, 82(5), 1129–1144. <https://doi.org/10.1016/j.neuron.2014.03.034>
- Lim**, L., Mi, D., Llorca, A., & Marín, O. (2018). Development and Functional Diversification of Cortical Interneurons. *Neuron*. <https://doi.org/10.1016/j.neuron.2018.10.009>
- Lozovaya**, N., Eftekhari, S., Cloarec, R., Gouty-Colomer, L. A., Dufour, A., Riffault, B., ... Hammond, C. (2018). GABAergic inhibition in dual-transmission cholinergic and GABAergic striatal interneurons is abolished in Parkinson disease. *Nature Communications*, 9(1). <https://doi.org/10.1038/s41467-018-03802-y>
- Maccaferri**, G., David, J., Roberts, B., Szucs, P., Cottingham, C. A., & Somogyi, P. (2000). Cell surface domain specific postsynaptic currents evoked by identified GABAergic neurones in rat hippocampus in vitro. *Journal of Physiology*, 524(1), 91–116. <https://doi.org/10.1111/j.1469-7793.2000.t01-3-00091.x>
- Mallet**, N., Delgado, L., Chazalon, M., Miguelez, C., & Baufreton, J. (2019). Cellular and Synaptic Dysfunctions in Parkinson's Disease: Stepping out of the Striatum. *Cells*, 8(9), 1–29. <https://doi.org/10.3390/cells8091005>
- Martínez-Cerdeño**, V., Noctor, S. C., Espinosa, A., Ariza, J., Parker, P., Orasji, S., ... Kriegstein, A. R. (2010). Embryonic MGE Precursor Cells Grafted into Adult Rat Striatum Integrate and Ameliorate Motor Symptoms in 6-OHDA-Lesioned Rats. *Cell Stem Cell*, 6(3), 238–250. <https://doi.org/10.1016/j.stem.2010.01.004>
- Massi**, L., Lagler, M., Hartwich, K., Borhegyi, Z., Somogyi, P., & Klausberger, T. (2012). Temporal dynamics of parvalbumin-expressing axo-axonic and basket cells in the rat medial prefrontal cortex in vivo. *Journal of Neuroscience*, 32(46), 16496–16502. <https://doi.org/10.1523/JNEUROSCI.3475-12.2012>
- McBain**, C. J., DiChiara, T. J., & Kauer, J. A. (1994). Activation of metabotropic glutamate receptors differentially affects two classes of hippocampal interneurons and potentiates excitatory synaptic transmission. *Journal of Neuroscience*, 14(7), 4433–4445. <https://doi.org/10.1523/jneurosci.14-07-04433.1994>

- McGregor, M. M., & Nelson, A. B. (2019).** Circuit Mechanisms of Parkinson's Disease. *Neuron*, 101(6), 1042–1056. <https://doi.org/10.1016/j.neuron.2019.03.004>
- Muller, C., & Remy, S. (2014).** Dendritic inhibition mediated by O-LM and bistratified interneurons in the hippocampus. *Frontiers in Synaptic Neuroscience*, 6(SEP), 1–15. <https://doi.org/10.3389/fnsyn.2014.00023>
- Muñoz-Manchado, A. B., Bengtsson Gonzales, C., Zeisel, A., Munguba, H., Bekkouche, B., Skene, N. G., ... Hjerling-Leffler, J. (2018).** Diversity of Interneurons in the Dorsal Striatum Revealed by Single-Cell RNA Sequencing and PatchSeq. *Cell Reports*, 24(8), 2179–2190.e7. <https://doi.org/10.1016/j.celrep.2018.07.053>
- Neske, G. T., Patrick, S. L., & Connors, B. W. (2015).** Contributions of diverse excitatory and inhibitory neurons to recurrent network activity in cerebral cortex. *Journal of Neuroscience*, 35(3), 1089–1105. <https://doi.org/10.1523/JNEUROSCI.2279-14.2015>
- Nosten-Bertrand, M., Kappeler, C., Dinocourt, C., Denis, C., Germain, J., Tuy, F. P. D., ... Francis, F. (2008).** Epilepsy in Dcx knockout mice associated with discrete lamination defects and enhanced excitability in the hippocampus. *PLoS ONE*, 3(6). <https://doi.org/10.1371/journal.pone.0002473>
- Palop, J. J., & Mucke, L. (2009).** Epilepsy and cognitive impairments in alzheimer disease. *Archives of Neurology*, 66(4), 435–440. <https://doi.org/10.1001/archneurol.2009.15>
- Pascual, M., Pérez-Sust, P., & Soriano, E. (2004).** The GABAergic septohippocampal pathway in control and reeler mice: Target specificity and termination onto reelin-expressing interneurons. *Molecular and Cellular Neuroscience*, 25(4), 679–691. <https://doi.org/10.1016/j.mcn.2003.12.009>
- Patrylo, P. R., Browning, R. A., & Cranick, S. (2006).** Reeler homozygous mice exhibit enhanced susceptibility to epileptiform activity. *Epilepsia*, 47(2), 257–266. <https://doi.org/EPI417> [pii]\r10.1111/j.1528-1167.2006.00417.x
- Pawelzik, H., Hughes, D. I., & Thomson, A. M. (2002).** Physiological and morphological diversity of immunocytochemically defined parvalbumin- and cholecystokinin-positive interneurons in CA1 of the adult rat hippocampus. *Journal of Comparative Neurology*, 443(4), 346–367. <https://doi.org/10.1002/cne.10118>
- Paylor, R., Hirotsune, S., Gambello, M. J., Yuva-Paylor, L., Crawley, J. N., & Wynshaw-Boris, A. (1999).** Impaired Learning and Motor Behavior in Heterozygous Pafah1b1 (Lis1) Mutant Mice. *Learning & Memory*, 6(5), 521–537. <https://doi.org/10.1101/lm.6.5.521>

- Pelkey, K. A., Chittajallu, R., Craig, M. T., Tricoire, L., Wester, J. C., & McBain, C. J. (2017).** Hippocampal GABAergic Inhibitory Interneurons. *Physiological Reviews*, *97*(4), 1619–1747. <https://doi.org/10.1152/physrev.00007.2017>
- Price, C. J., Cauli, B., Kovacs, E. R., Kulik, A., Lambolez, B., Shigemoto, R., & Capogna, M. (2005).** Neurogliaform neurons form a novel inhibitory network in the hippocampal CA1 area. *Journal of Neuroscience*, *25*(29), 6775–6786. <https://doi.org/10.1523/JNEUROSCI.1135-05.2005>
- Rudy, B., & McBain, C. J. (2001).** Kv3 channels: Voltage-gated K⁺ channels designed for high-frequency repetitive firing. *Trends in Neurosciences*, *24*(9), 517–526. [https://doi.org/10.1016/S0166-2236\(00\)01892-0](https://doi.org/10.1016/S0166-2236(00)01892-0)
- Savanthrapadian, S., Meyer, T., Elgueta, C., Booker, S. A., Vida, I., & Bartos, M. (2014).** Synaptic Properties of SOM- and CCK-Expressing Cells in Dentate Gyrus Interneuron Networks. *Journal of Neuroscience*, *34*(24), 8197–8209. <https://doi.org/10.1523/JNEUROSCI.5433-13.2014>
- Silberberg, G., & Markram, H. (2007).** Disynaptic Inhibition between Neocortical Pyramidal Cells Mediated by Martinotti Cells. *Neuron*, *53*(5), 735–746. <https://doi.org/10.1016/j.neuron.2007.02.012>
- Sohal, V. S., Zhang, F., Yizhar, O., & Deisseroth, K. (2009).** Parvalbumin neurons and gamma rhythms enhance cortical circuit performance. *Nature*, *459*(7247), 698–702. <https://doi.org/10.1038/nature07991>
- Szabadics, J., Tamás, G., & Soltesz, I. (2007).** Different transmitter transients underlie presynaptic cell type specificity of GABAA,slow and GABAA,fast. *Proceedings of the National Academy of Sciences of the United States of America*, *104*(37), 14831–14836. <https://doi.org/10.1073/pnas.0707204104>
- Tahvildari, B., Wölfel, M., Duque, A., & McCormick, D. A. (2012).** Selective functional interactions between excitatory and inhibitory cortical neurons and differential contribution to persistent activity of the slow oscillation. *Journal of Neuroscience*, *32*(35), 12165–12179. <https://doi.org/10.1523/JNEUROSCI.1181-12.2012>
- Tasic, B., Yao, Z., Graybiel, L. T., Smith, K. A., Nguyen, T. N., Bertagnolli, D., ... Zeng, H. (2018).** Shared and distinct transcriptomic cell types across neocortical areas. *Nature*, *563*(7729), 72–78. <https://doi.org/10.1038/s41586-018-0654-5>
- Tricoire, L., Pelkey, K. A., Erkkila, B. E., Jeffries, B. W., Yuan, X., & McBain, C. J. (2011).** A Blueprint for the Spatiotemporal Origins of Mouse Hippocampal Interneuron Diversity. *Journal of Neuroscience*, *31*(30), 10948–10970. <https://doi.org/10.1523/JNEUROSCI.0323-11.2011>

- Tricoire, L., Pelkey, K. A., Daw, M. I., Sousa, V. H., Miyoshi, G., Jeffries, B., ... McBain, C. J. (2010).** Common origins of hippocampal ivy and nitric oxide synthase expressing neurogliaform cells. *Journal of Neuroscience*, *30*(6), 2165–2176. <https://doi.org/10.1523/JNEUROSCI.5123-09.2010>
- Tsai, L. H., & Gleeson, J. G. (2005).** Nucleokinesis in neuronal migration. *Neuron*, *46*(3), 383–388. <https://doi.org/10.1016/j.neuron.2005.04.013>
- Verret, L., Mann, E. O., Hang, G. B., Barth, A. M. I., Cobos, I., Ho, K., ... Palop, J. J. (2012).** Inhibitory interneuron deficit links altered network activity and cognitive dysfunction in alzheimer model. *Cell*, *149*(3), 708–721. <https://doi.org/10.1016/j.cell.2012.02.046>
- Volk, D. W., Austin, M. C., Pierri, J. N., Sampson, A. R., & Lewis, D. a. (2000).** Decreased Glutamic Acid Decarboxylase 67 Messenger RNA Expression in a Subset of Prefrontal Cortical gamma-Aminobutyric Acid Neurons in Subjects With Schizophren. *Archives Gen Psychiatry*, *57*, 237–245. <https://doi.org/10.1001/archpsyc.57.3.237>
- Wang, W., Takashima, S., Segawa, Y., Itoh, M., Shi, X., Hwang, S. K., ... Hirose, S. (2011).** The developmental changes of Nav1.1 and Nav1.2 expression in the human hippocampus and temporal lobe. *Brain Research*, *1389*, 61–70. <https://doi.org/10.1016/j.brainres.2011.02.083>
- Williams, S., & Boksa, P. (2010).** Gamma oscillations and schizophrenia. *Journal of Psychiatry and Neuroscience*, *35*(2), 75–77. <https://doi.org/10.1503/jpn.100021>
- Wong, M., & Roper, S. N. (2016).** Genetic animal models of malformations of cortical development and epilepsy. *Journal of Neuroscience Methods*, *260*, 73–82. <https://doi.org/10.1016/j.jneumeth.2015.04.007>
- Yoshimura, Y., & Callaway, E. M. (2005).** Fine-scale specificity of cortical networks depends on inhibitory cell type and connectivity. *Nature Neuroscience*, *8*(11), 1552–1559. <https://doi.org/10.1038/nn1565>
- Zaqout, S., Blaesius, K., Wu, Y. J., Ott, S., Kraemer, N., Becker, L. L., ... Kaindl, A. M. (2019).** Altered inhibition and excitation in neocortical circuits in congenital microcephaly. *Neurobiology of Disease*, *129*(April), 130–143. <https://doi.org/10.1016/j.nbd.2019.05.008>
- Zhang, J., Velmeshev, D., Hashimoto, K., Huang, Y.-H., Hofmann, J. W., Shi, X., ... Huang, E. J. (2020).** Neurotoxic microglia promote TDP-43 proteinopathy in progranulin deficiency. *Nature*. <https://doi.org/10.1038/s41586-020-2709-7>
- Zhang, Z. J., & Reynolds, G. P. (2002).** A selective decrease in the relative density of parvalbumin-immunoreactive neurons in the hippocampus in schizophrenia. *Schizophrenia Research*, *55*(1–2), 1–10. [https://doi.org/10.1016/S0920-9964\(01\)00188-8](https://doi.org/10.1016/S0920-9964(01)00188-8)

Zheng, W., Xiang, Y. T., Yang, X. H., Xiang, Y. Q., & De Leon, J. (2017). Clozapine augmentation with antiepileptic drugs for treatment-resistant schizophrenia: A meta-analysis of randomized controlled trials. *Journal of Clinical Psychiatry, 78*(5), e498–e505.
<https://doi.org/10.4088/JCP.16r10782>

Chapter 2.

Aberrant sorting of hippocampal complex pyramidal cells in type I lissencephaly alters topological innervation

***Note:** This chapter was published as the following citation:

James A D'Amour, **Tyler Ekins**, Stuti Ganatra, Xiaoqing Yuan, and Chris J McBain (2020).

Aberrant sorting of hippocampal complex pyramidal cells in type I lissencephaly alters topological innervation. eLife 2020;9:e55173

Details of T. Ekins contributions:

I conducted immunohistochemistry experiments, recorded intrinsic electrophysiological properties of pyramidal neurons, imaged and reconstructed pyramidal neurons, performed pharmacology experiments with agatoxin and conotoxin, analyzed data, created figures and edited the manuscript.

ABSTRACT

Layering has been a long-appreciated feature of higher order mammalian brain structures but the extent to which it plays an instructive role in synaptic specification remains unknown. Here we examine the formation of synaptic circuitry under cellular heterotopia in hippocampal CA1, using a mouse model of the human neurodevelopmental disorder Type I Lissencephaly. We identify calbindin-expressing principal cells which are mispositioned under cellular heterotopia. Ectopic calbindin-expressing principal cells develop relatively normal morphological features and stunted intrinsic physiological features. Regarding network development, a connectivity

preference for cholecystinin-expressing interneurons to target calbindin-expressing principal cells is diminished. Moreover, in vitro gamma oscillatory activity is less synchronous across heterotopic bands and mutants are less responsive to pharmacological inhibition of cholecystinin-containing interneurons. This study will aid not only in our understanding of how cellular networks form but highlight vulnerable cellular circuit motifs that might be generalized across disease states.

INTRODUCTION

Cellular layers and refined somatic positioning are the hallmark of more evolutionarily developed brain structures. However, little is known regarding the contributions of layers to cellular maturation and local microcircuit formation. Disorders affecting cellular lamination offer a unique window of study into cellular and circuit development in the absence or disruption of traditional positional cues present in layers. Cellular heterotopias within brain structures result from a variety of developmental insults to an organism but share the common feature of lacking normal cellular layering typical in the cortex and hippocampus of mammalian brains; and like many things, how it falls apart speaks to its construction (Anusha, 2014; Di Donato et al., 2017).

While heterotopias may arise from diverse causes, they share some common phenotypes (Kato, 2003). Particularly devastating heterotopias involve mutations to genes that encode proteins essential to cellular migration and proliferation (Hirotsune et al., 1998). Brains from these patients often appear smooth, lacking the infoldings and gyri of healthy human subjects. Broadly, this condition is referred to as lissencephaly, meaning 'smooth brain'. One of the most common and first identified genetic causes of Type I lissencephaly is due to mutations in the Lis1

gene (Pafah1b1), which encodes an enzyme essential for nuclear kinesis and microtubule stabilization (Hirotsune et al., 1998; Dobyns and Das, 2009; McManus et al., 2004; Wynshaw-Boris, 2007). Unsurprisingly, mutations to other parts of this migratory pathway also result in lissencephalies and more recently infections during embryonic development have received renewed attention for their role in microcephalies, such as the mosquito transmitted Zika virus (for example DCX, YWHAE, RELN, ARX) (Kato, 2003; Rice et al., 2018). As alluded to above, these disorders also produce intra-structure cellular heterotopias which are characterized by mispositioned cell somas and disorganized cellular layering.

Rodent brains lack gyri but mice heterozygous for the human mutant Pafah1b1 allele (Lis1-MUT, Lis mutants) display severe cellular heterotopias in both cortex and hippocampus, developmental defects, hydrocephaly, and enlarged ventricles. These mice also have increased network excitability, lowered seizure threshold, and increased spontaneous mortality rate – features shared with the human condition (Fleck et al., 2000; Hunt et al., 2012). Interestingly, these heterotopias in area CA1 of the hippocampus have a tendency to fragment the single excitatory principal cell layer (PCL) into multiple pyramidal cell bands, stacked vertically on one another – transitioning the region into what looks like a primitive cortical structure with multiple excitatory layers. Concurrently, hippocampal researchers have proposed a system of parallel information processing being carried out among the intertwined circuitry of CA1, where-in preferential interneuron targeting acts to segregate information streams to different sets of principal neurons (Soltesz and Losonczy, 2018). It seems possible, if not likely, that these crude laminar structures resulting from faulty cellular migration in the Lis1 mutant mouse, might reflect natural underlying patterns in local circuit connectivity upon which normal hippocampal function

is critically dependent. Clearly, mislamination is a shared feature of several human neurodevelopmental disorders that merits deeper investigation and may inform our understanding of normal hippocampal development and function.

In light of studies suggesting specified microcircuitry among deep versus superficial principal cells and local basket cells in wild type (Wt) CA1, we wondered if the heterotopic cell layers observed in *Lis1* mutants reflected a functional distinction between discrete microcircuitry of the PCL (Soltesz and Losonczy, 2018; Lee et al., 2014; Nielsen et al., 2010; Slomianka et al., 2011; Valero et al., 2015). Recent evidence suggesting a preferential connectivity between principal cells and either parvalbumin (PV) or cholecystokinin (CCK) expressing interneurons, depending on the extrahippocampal projection target, somatic position of the principal cell, or marker expression of the principal cell, suggests an underlying blueprint in the establishment of hippocampal circuitry and connectivity that has been previously underappreciated in what otherwise appears as a monolithic excitatory lamina, the PCL (Soltesz and Losonczy, 2018; Lee et al., 2014; Nielsen et al., 2010; Slomianka et al., 2011; Valero et al., 2015; DeFelipe, 1997; Deguchi et al., 2011; Valero and de la Prida, 2018; Varga et al., 2010). This model will allow us to identify the same cell subtypes in non-mutant and mutant littermates and examine to what extent their relative relationships are preserved under mis-lamination. Put more succinctly, to what extent are innate wiring motifs disrupted under heterotopia?

Remarkably, in subjects suffering from cellular heterotopias that survive into adulthood cellular networks function surprisingly well and animals are often behaviorally indistinguishable from normal type littermates (Salinger et al., 2003; Wagener et al., 2010; Wagener et al., 2016). In the more thoroughly studied *Reeler* mouse model, that displays severe cortical and

hippocampal mis-lamination, cells in cortex appear to be relatively healthy and are integrated into the local network (Wagener et al., 2016; Boyle et al., 2011; Caviness and Sidman, 1973; Guy and Staiger, 2017; Polleux et al., 1998). Collectively, the evidence suggests that the formation of functional synaptic connectivity has some innate resilience to mis-lamination and layers may play little to no role in the guidance and establishment of synaptic connectivity (Wagener et al., 2016; Guy and Staiger, 2017; Caviness and Rakic, 1978; Guy et al., 2015). Furthermore, if there was logic behind the dividing of these heterotopic cell populations the Lis1-MUT would represent an ideal model to assay the resilience of genetic network formation blueprints to the developmental/local-environment cues of intra-structure position and layering (Soltesz and Losonczy, 2018; Harris and Shepherd, 2015; Margeta and Shen, 2010; Sur and Rubenstein, 2005). This might permit us to determine over what relative distances genetic wiring programs are able to locate and synapse on the appropriate postsynaptic targets, shed light on what appears to be intertwined parallel circuitry for information processing in CA1, and identify synaptic connectivity motifs that are more susceptible to heterotopia than others (Soltesz and Losonczy, 2018; Valero and de la Prida, 2018; Varga et al., 2010). Ultimately, these studies provide key insight into what is the role of layers in higher mammalian brain structures and highlight the proper areas of study for future treatment of cellular heterotopias.

RESULTS

Heterotopic banding of the principal cell layer in Lis1 mutant mice

Non-conditional Pafah1b1 +/- mice were generated by breeding a Pafah1b1 +/- Fl line to Sox2-cre animals, heterozygous mice are referred to henceforth as Lis1-MUT. Lis1-MUT mice were often

noticeably smaller than litter mates. Some animals displayed severe macroscopic brain abnormalities, including enlarged ventricles, hydrocephaly, intracranial bleeding, and spontaneous death. Lis1-MUT mice that survived to 3–5 weeks of age were used for experiments and subsequent breeding; non-mutant littermates were used as controls. In coronal sections from dorsal hippocampus Lis1-MUT animals displayed heterotopic banding of the principal cell layer (Figure 1A). Banding varied in severity, cell soma density, and septal-temporal extent. Most animals displayed the strongest banding in area CA1, with fewer mice showing multiple PCLs past region CA2. Region CA3 rarely appeared banded, but instead scattered and uncompact. Mice occasionally had three distinct layers or clustered islands of cells, but most typically two prominent PCLs could be seen (Figure 1A, right vs left). Deeper bands were typically situated in what would be stratum oriens-alveus in a non-mutant animal. In measuring from the border of the alveus and the cortex radially (toward radiatum, known as the radial axis of CA1), the entirety of normal wild type (Wt) PCLs were located between ~175–300 μm . In Lis1-MUT mice, superficial bands were positioned between ~250–320 μm and deeper heterotopic bands (positioned closer to the alveus) were between ~100 and 190 μm . Of the two bands, the superficial tended to be more densely populated and closer to the normal positioning of the PCL in normal type mice (Figure 1A and B). We next considered whether these heterotopic bands were splitting randomly, or if the banding represented distinct cell populations.

Calbindin expressing principal cells preferentially position in the deeper heterotopic band of CA1 in Lis1 mutant

In order to better understand the banding process in mutant mice, immunohistochemistry experiments were carried out for principal cell markers and quantified by normalized expression levels in each heterotopic band (n antibody stained cells/ n dapi cells in same region of interest). In addition to marking a subpopulation of GABAergic cells, calbindin is expressed in superficial principal cells in several species (Slomianka et al., 2011). Consistent with these reports, our Lis1 wild-type litter mates show calbindin-expression among superficial principal cells of CA1 (Figure 1B, *left*). These cells are tightly packed, forming one-three rows of somas on the stratum radiatum adjacent (superficial) side of the PCL. Conversely, calbindin staining in Lis1-MUT mice showed a strong bias for calbindin-expressing principal cells to occupy the deeper heterotopic principal cell layer (Figure 1B, *right*). Figure 1D shows a normalized histogram of identified calbindin-positive cell soma positions in Lis1 mutants and wild-type litter mate controls. Note for quantification purposes, the deep and superficial bands are analyzed as separate regions of interest, numbers represent the fraction of cells in that particular band expressing calbindin. Analogously, the single wild-type PCL is divided in half radially (top versus bottom) and analyzed as separate deep and superficial bands (Figure 1E; Distal CA1 Wt: deep $8.9 \pm 2.8\%$; superficial $25.1 \pm 1.3\%$; Lis1-MUT: deep $18.0 \pm 2.8\%$; superficial $4.4 \pm 1.0\%$, $n = 12$ Wt and 12 Lis1-MUT slices from six animals, respectively). This finding was not a general feature of having the Lis1 mutant allele, as in animals with less severe banding (or in the same slices nearer CA2) but still carrying the mutant *Pafah1b1* allele, the PCL displayed relatively normal, superficial calbindin soma positioning (Figure 1F; Proximal CA1 Wt: deep $16.3 \pm 2.3\%$; superficial $30.0 \pm 2.0\%$; Lis1-MUT: deep $12.1 \pm 2.3\%$; superficial $19.0 \pm 2.4\%$, $n = 12$ and 11, respectively). A large proportion of the principal cells expressing calbindin are being preferentially shifted into the deeper heterotopic

band, but it should be noted that calbindin cells overall still represent a minority of the population in either location. Given that principal cells are generated near what becomes the alveus and migrate radially during embryonic development in a deep to superficial manner (Caviness and Sidman, 1973; Angevine, 1965; Stanfield and Cowan, 1979), the calbindin staining pattern suggested a late born population undergoing migratory failure in the *Lis1*-MUT mouse.

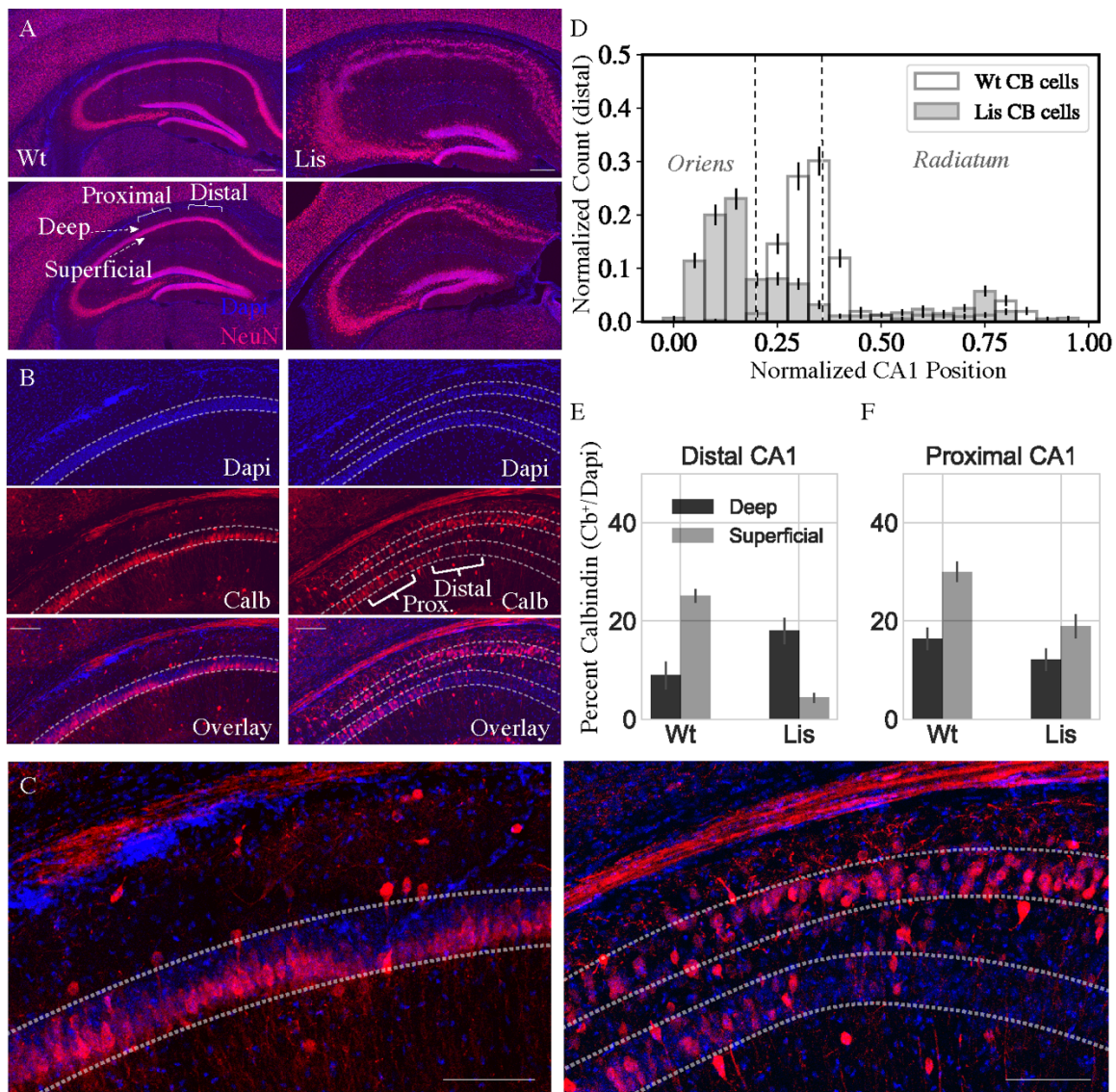


Figure 1. *Lis* mutants display heterotopic banding and ectopic positioning of calbindin-expressing principal cells.

(A) *Left*, two coronal NeuN stained images from differing levels of dorsal CA1 hippocampus in a wild-type littermate. *Right*, approximately matched coronal sections from a Lis mutant displaying heterotopic banding of the PCL. Scale bars are 300 μm . (B) *Left*, wild-type and Lis1-MUT, *right*, staining of CA1 highlighting the position of the PCL, calbindin-positive neurons, and overlay. Note the deep layer preference of calbindin-expressing neurons, particularly in distal CA1 in mutant. Scale bars are 200 μm . (C) Higher magnification view of the overlay images in (B), for wild-type (*left*) and Lis1-MUT (*right*). Scale bars are 150 μm . (D) Normalized histogram showing the positioning of calbindin-expressing cells in mutants with PCL banding compared to wild-type mice. (E) Percentage of cells in deep and superficial layers expressing calbindin in distal CA1 (for controls mice, the single PCL is divided in half radially). Counts represent number of identified calbindin soma divided by number of DAPI identified cells, Wt: deep $8.9 \pm 2.8\%$, superficial $25.1 \pm 1.3\%$; Lis1-MUT: deep $18.0 \pm 2.8\%$, superficial $4.4 \pm 1.0\%$. (F) Same as (E) for proximal CA1, Wt: deep $16.3 \pm 2.3\%$, superficial $30.0 \pm 2.0\%$; Lis1-MUT: deep $12.1 \pm 2.3\%$, superficial $19.0 \pm 2.4\%$; $n = 12$ Wt and 12 Lis1-MUT slices for distal and 12 and 11 for proximal, from six animals.

Embryonic development of the calbindin expressing principal cells

Superficial principal cells in normal mice arise near the end of gestation (Emb days 16–17) (Slomianka et al., 2011; Caviness and Sidman, 1973; Angevine, 1965). Our initial data suggests that the heterotopic banding in Lis1-MUT mice may arise from a migratory stalling event, where later born superficial-preferring cells were unable to overcome a migratory burden and instead form a new deep heterotopic layer. In order to test this hypothesis and ensure that a novel population of deeply positioned principal cells was not adopting calbindin expression in Lis1-MUT animals, cellular birth-dating experiments were performed.

In timed pregnancy experiments using Lis1 mutants crossed to *Neurog2-cre* were crossed with a cre-dependent EGFP reporter mouse (Rosa26 <RCE >), tamoxifen administration induces cre-recombination and subsequent eGFP expression in newly born neurons of developing mouse pups. Pregnant mothers were gavaged at various embryonic time points spanning days E12-17. After pups were born, they were perfused and fixed at ~P30 for calbindin staining, and subsequent quantification of the percentage of eGFP expressing neurons from any time point

that were co-stained for calbindin (Figure 2A–C). Approximately 10% of cells born on E12-E13 expressed calbindin at P30 (Figure 2D; Wt: $9 \pm 3\%$; Lis1-MUT: $12 \pm 3\%$, n = 95 cells and 168 labeled cells analyzed from five animals, respectively) in both Lis1 wild-type littermates and mutants. Cells born E14-E15 co-stained for calbindin $42 \pm 9\%$ of the time for wild type and $52 \pm 8\%$ (n = 221 and n = 128, from 10 animals) for Lis1 mutants and cells born E16-E17 co-stained for calbindin $54 \pm 7\%$ of the time for wild type and $71 \pm 9\%$ for Lis1 mutants (n = 48 and 20 labelled cells from 11 animals). While the timing of calbindin cell birthdates remained similar to littermate controls in Lis1-MUT animals in that calbindin cells arise late in embryonic development (Figure 2D), positioning of these cells differed substantially. Later born cells positioned more superficially in wild-type littermates (smaller PCL depth measurements), while they positioned more deeply in mutant mice (Figure 2E and F, E represents counts from single experiments data are averages and summarized in F). These results suggest that deeply positioned calbindin-expressing cells in the Lis1-MUT mice are the same late-born cell population that are now ectopically positioned in the deeper heterotopic band.

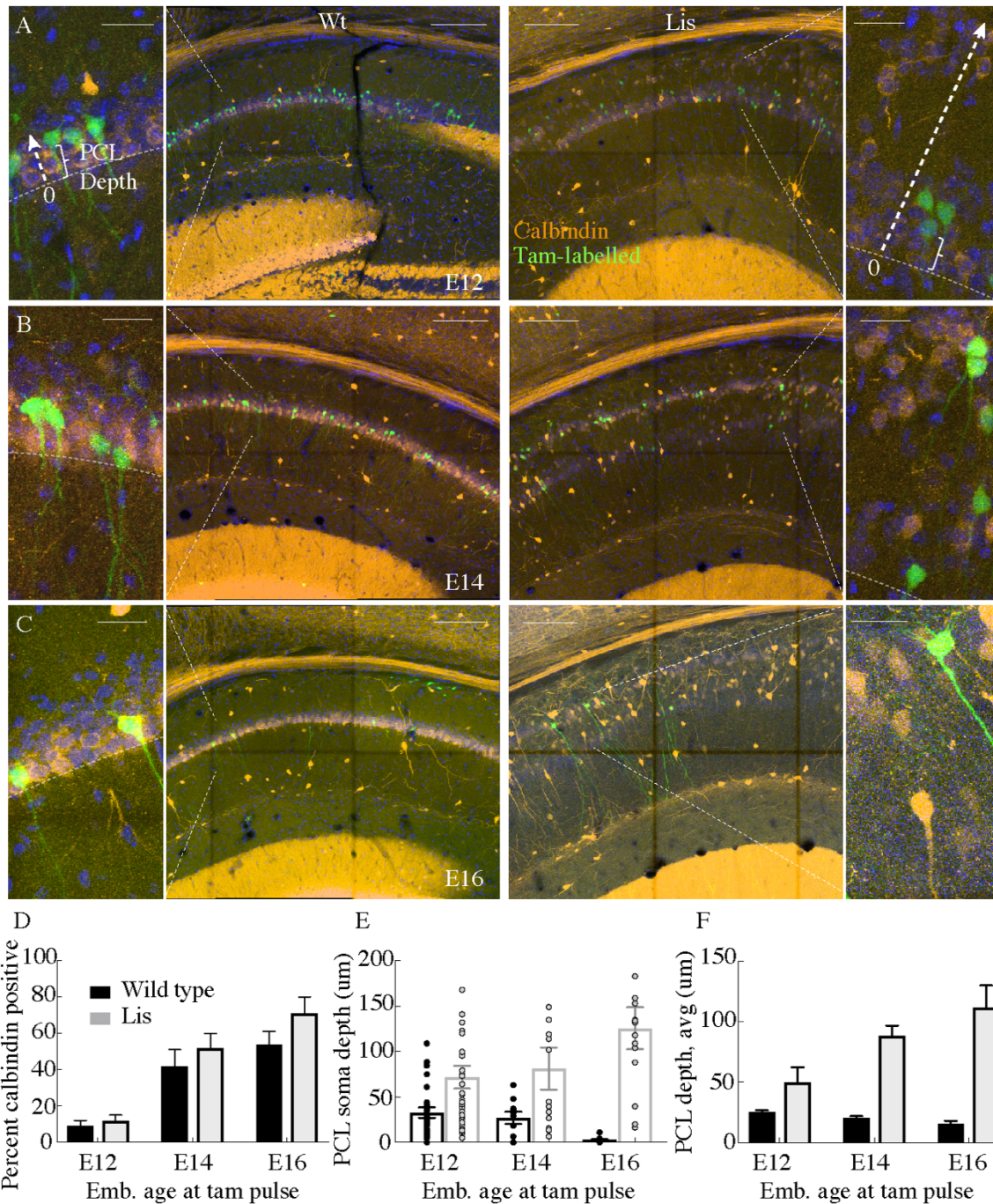


Figure 2. Cellular birth-dating indicates ectopic calbindin cells in Lis mutants are the same late-derived embryologic population.

(A) Wild-type (*left*) and Lis mutant (*right*) example birth-dating images for a litter tamoxifen dosed between E12-E13. Note the cutout, displaying how cellular somatic positioning was measured from the front of the PCL (as opposed to normalized structural position). Green corresponds to cells born during tamoxifen administration; orange is calbindin immunohistochemistry staining carried out when litters are P30. (B) Same as in (A) but for litters dosed at E14-E15. (C) Same as (A) but for litters dosed at E16-E17. (D) Quantification of the

fraction tamoxifen-marked neurons co-staining for calbindin antibody from each timepoint. E12: Wt: $9 \pm 3\%$; Lis1-MUT: $12 \pm 3\%$, E14: Wt: $42 \pm 9\%$; Lis1-MUT: $52 \pm 8\%$, E16: Wt: $54 \pm 7\%$; Lis1-MUT: $71 \pm 9\%$. (E) Example counts from single images at each timepoint for PCL depth measurements. Later born cells position more superficially (front of the PCL) in non-mutants, but deeper in Lis1-MUT littermates. (F) Group averages for the measurements shown in (E). E12- Wt: $25.4 \pm 1.4 \mu\text{m}$; Lis1-MUT: $50 \pm 12.3 \mu\text{m}$, E14- Wt: $20.5 \pm 1.3 \mu\text{m}$; Lis1-MUT: $88 \pm 8.7 \mu\text{m}$, E16- Wt: $15.6 \pm 2.6 \mu\text{m}$; Lis1-MUT: $111.6 \pm 18.3 \mu\text{m}$. Scale bars are $150 \mu\text{m}$ and $25 \mu\text{m}$ for the main image and zoom, respectively.

Calbindin-expressing principal cells retain a complex apical morphology

Previous studies have documented variation in CA1 principal cell morphology, particularly in comparing basal and apical dendritic trees (Lee et al., 2014; Bannister and Larkman, 1995; Li et al., 2017). These morphological features can be reliably used to differentiate excitatory neuron subtypes. In particular, calbindin-expressing principal cells have more complex apical dendritic trees (more branching), than calbindin-negative counterparts (Li et al., 2017). This has enabled offline characterization of excitatory cell group through K-means clustering of morphological features after cellular reconstructions. A prior study using this approach suggested that clustering was greater than 90% accurate as verified by mRNA and in situ hybridization approaches but comes with the drawback that every recording must be histologically processed, virtually reconstructed, and analyzed (Li et al., 2017). Additionally, there is a minimal threshold for the amount of dendritic tree that must be recovered and drawn for clustering to be accurate.

In our 63 best recovered principal cell morphologies from physiological recording experiments ($n = 32$ wild type, $n = 31$ Lis1-MUT), we implemented a k-means clustering algorithm based on dendritic branch connectivity and lengths that generates length-ratio index (LRI) values and node-ratio index values (ORI), as done previously, with a minor modification to cell values if selected nodes were distant from the soma (Li et al., 2017). See Materials and methods for more

details. The clustering results from mutant and wild-type litter mate cellular morphologies are shown in Figure 3B. The same process was applied to mutant and wild-type cells, but these groups were processed independently by a supervised k-means algorithm that expected two groups, corresponding to complex and simple morphologies. While morphologically speaking, additional subtypes of principal neurons likely exist in CA1 (if analyzing basal dendrites or soma size etc.), the present study makes use of prior work for the purposes of separating principal cells along the lines of calbindin positive and calbindin negative populations. However, preliminary clustering analysis using within cluster sum of squares (elbow plots) suggested $n_{cluster} = 2$ is not an unreasonable choice for apical dendritic morphology in agreement with the original study (data not shown). Note, not all cells come from the same experimental group as in this figure we are looking for the best morphological recoveries, therefore not every morphological data point will have corresponding physiological data points causing N's to vary between some subpanels – the same should be noted for the analysis in Figure 4.

The data show that relatively simple and complex cell morphologies persist in the Lis1 mutant, in approximately the same proportions to wild type mice, with nearly overlapping cluster centers (complex cells, Wt: [-0.1, 0.8], Lis1-MUT: [-0.4, 0.9]; simple cells, Wt: [-1.8,-1.3], Lis1-MUT: [-1.7,-1.2]). The nearness of the cluster centers for non-mutant and mutant data further suggest that fundamentally new clusters of morphological subtypes have not cropped up, but instead a relative relationship between complex and simple subtypes persists – even if Lis1 complex cells are less 'branchy' as described below in sholl analysis. A visual comparison of some of the more obviously simple and complex cellular recoveries suggests the sorting has been successful (Figure 3A & C, note deeply positioned complex cells in Lis1-MUT experiments).

Grouping cells by the assigned shape cluster and plotting the associated PCL depth measurements (from the border between the first PCL and the radiatum) gives further support to the sorting results, as complex cells were located superficial to simple cells in normal type controls and scattered but generally deeper than simple cells in Lis1-MUT mice, in agreement with our calbindin staining experiment (Figure 3D PCL depth, Wt complex: $35 \pm 8.0 \mu\text{m}$, simple: $50.2 \pm 6.3 \mu\text{m}$, $n = 13$ and 11 ; Lis1-MUT, complex: $127 \pm 23.4 \mu\text{m}$, simple: $94.6 \pm 12.3 \mu\text{m}$, $n = 8$ and 13).

Additionally, we observed that complex cells in both mutant and non-mutant animals tended to have their first prominent apical branch bifurcation points sooner than simple cells (Figure 3E). This suggests that the complex apical branch morphology can still be used to identify putative calbindin-expressing principal cells in Lis1-MUT mice. It should be noted that the clustering algorithm has no direct knowledge of somatic positioning, or what is determined to be the first primary apical bifurcation – yet these differences appear using the labels assigned in the clustering. More traditional morphological analyses such as sholl intersections fail to show clear differences between complex and simple cell types when they are pre-sorted by K-means label, highlighting the usefulness of analyzing branching patterns with this approach (Figure 3F–H, note that sholl intersections represent apical dendritic trees only and do not include basal dendrites). For additional confirmation that calbindin remains predictive of complex morphologies in Lis1-MUT animals, we crossed mice to a *Calb1-cre:Ai14* reporter line and made recordings in these mutants and processed their morphological reconstructions through the algorithm (Figure 3B; open and filled stars). Out of eight successful recoveries, four principal cells with confirmed calbindin expression had LRI and ORI values in the upper right (complex) quadrant (Figure 3I–K).

The remaining were calbindin negative and had relatively simple morphological values (Figure 3B, lower left). An additional three calbindin positive recordings are not included in the analysis, as their recoveries were split across multiple sections or incomplete, but these showed the hallmark of an early bifurcation point and dense early branching. These data support the notion that relatively complex and simple morphologies persist in the Lis1 mutant, and calbindin-expression remains predictive of the complex morphological group.

Readers should note, direct comparisons of sholl analysis from mutants and wild-type litter mates revealed a reduction in branch intersections in Lis1-MUT complex cells (Figure 3H). While wild-type complex cells typically have peak sholl intersections of 8–11 around 200 μm from the soma, Lis1-MUT complex cells have fewer peak intersections (~ 7), closer to the soma ($\sim 125 \mu\text{m}$) (Wt n = 10 complex and 14 simple; Lis1-MUT n = 10 complex and 12 simple). While relatively speaking, the complex and simple subtypes persist in the Lis1-MUT mice, there has been an effect of the mutation, either direct or indirect, in stunting general morphological development. Clustering was performed separately for mutant and non-mutant data to reveal relative relationships between sub-types of cells in one genetic condition rather than an absolute comparison of all cell morphologies, allowing us to compare how related cell subtypes and their associated microcircuits develop under heterotopia.

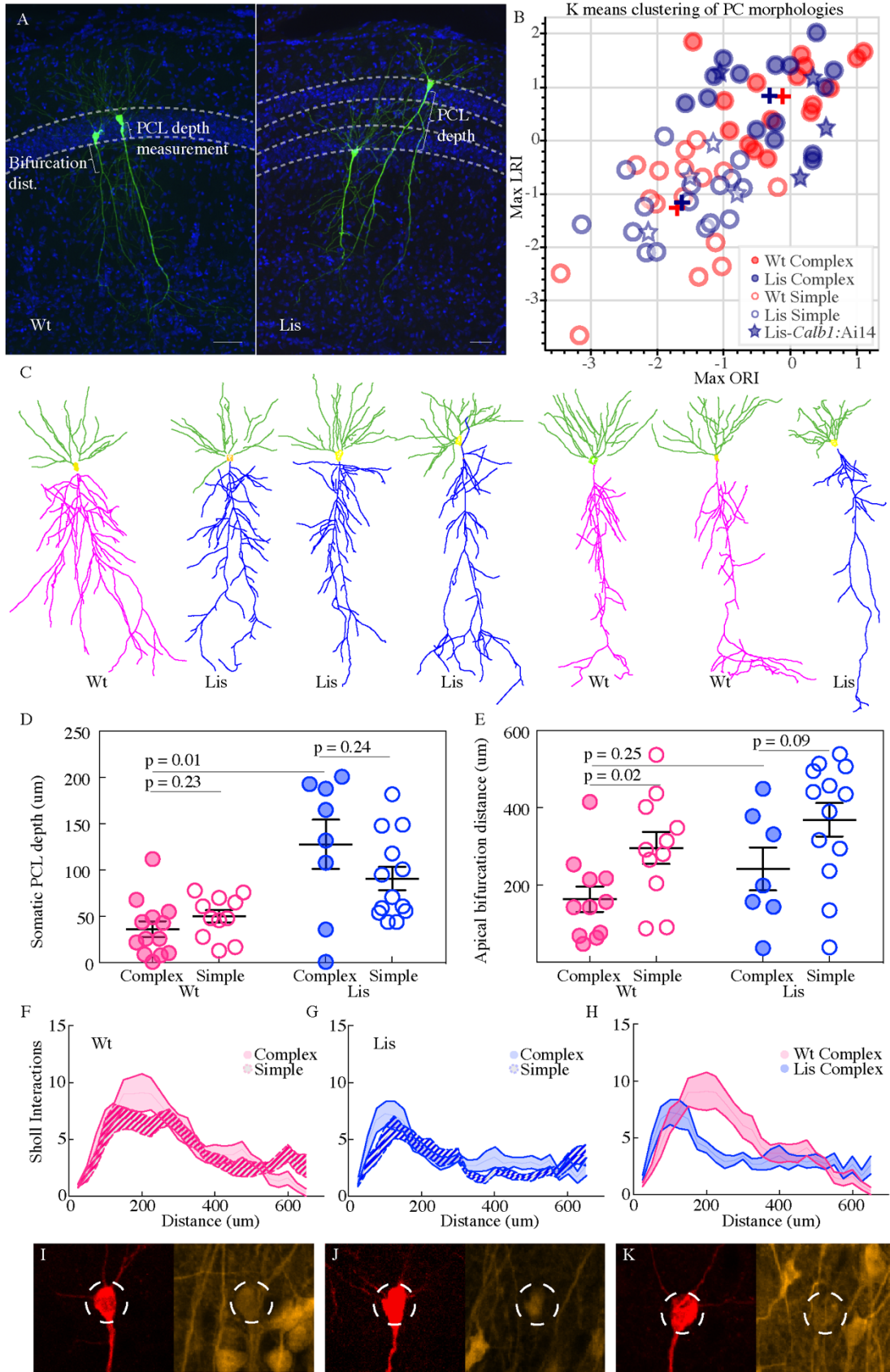


Figure 3. Lis1-MUT calbindin-expressing PCs retain relatively complex morphologies.

(A) Recovered cells from non-mutant and mutant experiments, highlighting different apical dendritic morphologies, complex and simple. Complex morphologies have been previously shown to be highly predictive of calbindin expression (Li et al., 2017). Scale bars are 50 μm . (B) Supervised K-means plots (63 best recovered cells, $k = 2$) carried out separately for mutant and wild-type data (blue and red respectively). Filled circles correspond to complex morphologies and open circles are simple. Stars are morphological recoveries from Lis1 mutants crossed to a *Calb1-cre;Ai14* mouse line ($n = 8$ total) – filled stars have confirmed calbindin expression and open stars are calbindin negative recordings. These cells are then run through the same clustering algorithm, and the associated LRI/ORI positions are plotted over the original clustering. Note filled and open stars fall in the upper right (complex) quadrant and the lower left (simple) quadrant, respectively. (C) Example morphological reconstructions, ranging from most complex (left) to simple (right). (D) Positional properties for predicted calbindin (complex, filled circles) and non-calbindin expressing (simple, open circles) principal cells. Note predicted calbindin expressing cells were superficial to non-calbindin predicted, and this trend was inverted for Lis1-MUT animals. Wt: complex $36.42 \pm 8.5 \mu\text{m}$, simple $50 \pm 6.9 \mu\text{m}$; Lis1-MUT: complex $128 \pm 26.6 \mu\text{m}$, simple $90.9 \pm 12.7 \mu\text{m}$, $n = 13, 11, 8, 13$, respectively. Depth is measured as it was for Figure 2 from the front/superficial side of the PCL. (E) Group sorted measurements for distance along primary apical dendrite until first prominent bifurcation occurs. Wt: complex $163 \pm 32.8 \mu\text{m}$, simple $295.9 \pm 41.4 \mu\text{m}$; Lis1-MUT: complex $241.6 \pm 55.8 \mu\text{m}$, simple $368.9 \pm 43.4 \mu\text{m}$. Note complex cells tend to bifurcate sooner in both mutant and non-mutants. (F) Sholl interactions from Wt apical dendrites alone, of complex and simple sorted cells. (G) Likewise, for Lis1-MUT animals. (H) Overlay of the complex morphology sholl data from non-mutant and mutant experiments. Despite retaining a relatively complex population, complex Lis1-MUT principal cells have decreased apical dendritic branching that peaks closer to the soma. (I–K) Somatic images confirming calbindin expression from three recordings performed in Lis1 mutants bred to a *Calb1-cre;Ai14* line. Morphologically these cells clustered with the complex group in (B) – filled stars, while calbindin negative recoveries (not shown here) are plotted as open stars in (B). Dashed circle diameter is 15 μm .

Lis1 mutant principal cells display disrupted physiological properties

From the whole-cell recordings that were used for morphological reconstructions in Figure 3 a battery of intrinsic physiological properties were analyzed in two ways. Several of these properties are shown in Figure 4. Each property was plotted against the PCL depth of the soma (somatic depth from the radial side of the PCL) from which the recording was made (Figure 4A). The same data were also sorted into putative calbindin-positive and calbindin-negative cell types as predicted by either complex or simple morphologies (Figures 3B and 4B). Resting membrane

potential displayed a pearson r value of 0.44 for correlation with position in wild-type litter mates, and a r-value of 0.07 in Lis1 mutant mice (Wt: n = 23, Lis1-MUT: n = 23). Sag index correlated with position at an r-value of 0.5 in wild-type mice and an r-value of 0.05 in Lis mutants (Wt: n = 24, Lis1-MUT: n = 26). Input resistance and depth in wild-type mice had a correlation value of $r = 0.2$, while in Lis mice $r = -0.1$ (Wt: n = 23, Lis1-MUT: n = 26).

In sorting recorded data by putative cell type, we noted that many of the positional differences observed in Figure 4A persisted or at least trended toward significant in wild-type littermates (complex cells are filled circles, open are simple; Resting membrane potential: Wt mean complex -63.3 ± 1.2 mV, simple -60.3 ± 1.2 mV, $p=0.09$ n=11 and 12; Sag index: mean complex 0.75 ± 0.02 , simple 0.79 ± 0.02 , $p=0.25$ n=12 and 12; Input resistance: complex 120.4 ± 6.8 M Ω , simple 149.3 ± 14.11 M Ω , $p=0.08$ n=11 and 12). Some of these differences in sub-types were still detectable in Lis1 mutants, but differences between principal cell sub-types for most properties seemed substantially diminished from those in normal mice (RMP: mean complex -61.2 ± 2.1 mV, simple -61.1 ± 1.5 mV, $p=0.96$ n=10 and 13; Sag index: mean complex 0.78 ± 0.02 , simple 0.81 ± 0.01 , $p=0.09$ n=13 and 13; R input: mean complex 171.9 ± 13.2 M Ω , simple 123.3 ± 13.02 M Ω , $p=0.29$ n=13 and 13). Note that not all physiological recordings had associated morphological recoveries. Additionally, in some recordings not all properties were measured, meaning some morphological groups vary in their summary N's.

We wondered if there were physiological subtypes of principal cells and how those subtypes might correspond to our previously identified morphological subtypes of complex and simple. Principal component analysis and subsequent K-means clustering was carried out on the physiological data (Figure 4C and D, resting membrane potential, sag index, input resistance,

spike amplitude, adaptation ratio, firing frequency at 2x threshold, spike threshold, and after hyperpolarization amplitude were used for physiological clustering). Note that the clustering in this figure has no knowledge of morphological features nor LRI or ORI values from Figure 3B – we merely carry over the morphological labels afterward. Pre-clustering analysis with nbclust and elbow plots was performed, both approaches suggested n cluster = 2 was the optimal solution (data not shown). We then scored where morphologically identified cells fell in the physiological clusters. Out of eight morphologically complex cells, six were found in physiological cluster 0 and the remaining two in physiological cluster 1. Of eleven morphologically simple cells, eight were located in physiological cluster 1 and the remaining three in cluster 0, suggesting that these physiological clusters roughly correspond to the two morphological subtypes identified in Figure 3 for wild-type littermates (Figure 4C). The same analysis in Lis1 mutants yielded uneven cluster counts, and no clear relationship between physiological cluster and morphological cluster (Figure 4D). The data indicate a loose relationship between morphological subtype and physiological subtype in wild-type animals that has been significantly perturbed under the Lis1 mutation - suggesting that physiological aspects of cellular identity may become smeared or lost under cellular heterotopia before or to a greater extent than morphological aspects. Put another way, cellular morphology is less predictive of intrinsic physiological properties under the Lis1 mutation.

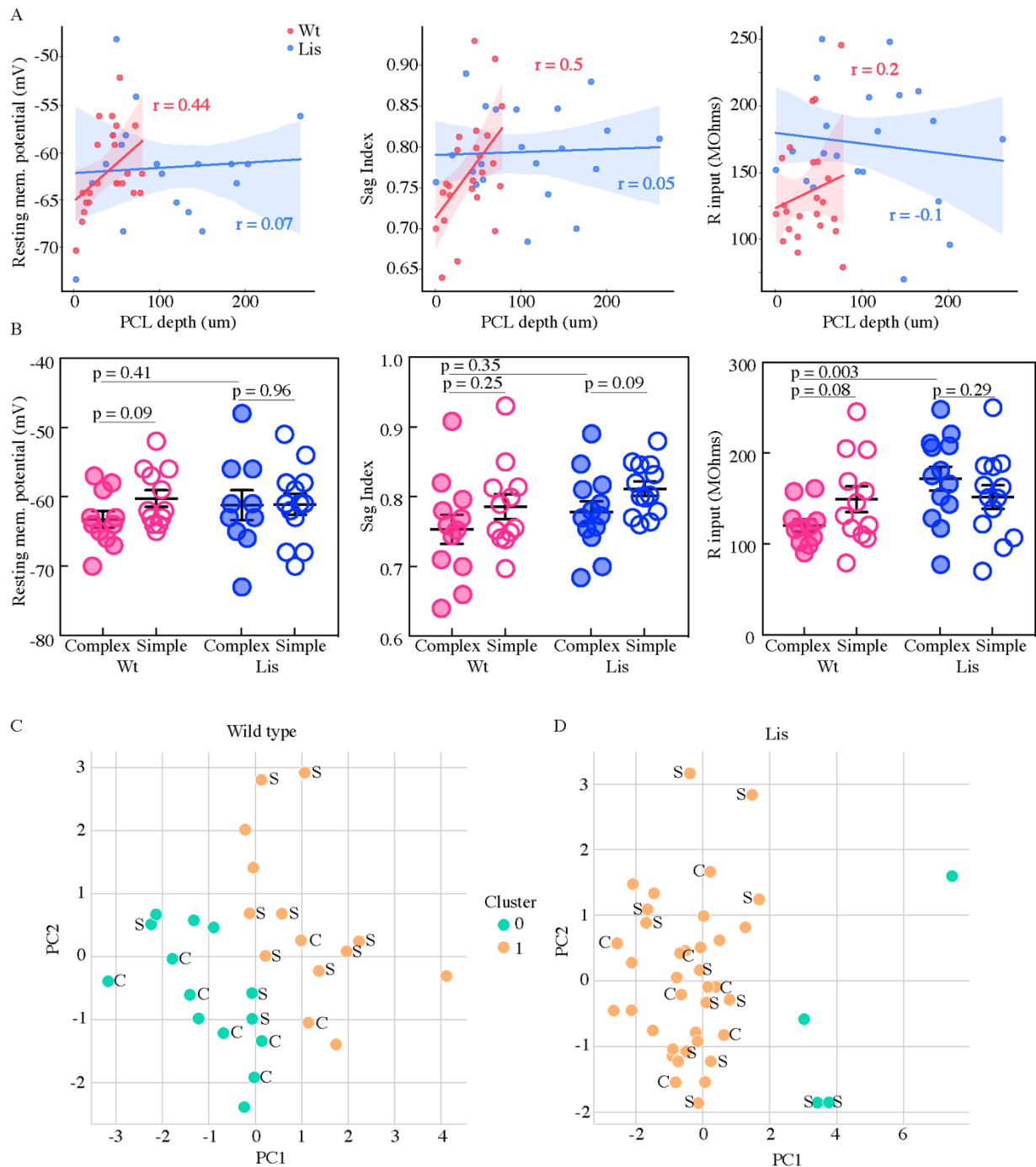


Figure 4. Physiological properties of calbindin positive and negative morphological clusters.

(A) *Left*, somatic PCL depth correlations with cellular resting membrane potential for wild-type (red) and Lis1-MUT (blue) recordings. *Middle*, likewise, for sag index, where values closer to 1 correspond to less sag exhibited. *Right*, same for input resistance. (B) Same data as in (A), grouped by predicted calbindin expression. (C) Supervised K-means ($n = 2$) sorting wild types. A handful of electrophysiological properties alone are capable of reasonably accurate morphological subtype prediction (and therefore calbindin expression). C's and S's correspond to

the data points associated morphological group, note that even mis-categorized points are near the midline. Of 8 morphologically complex cells, 6 are found in in physiological cluster 0, of 11 simple cells, 8 are found in physiological cluster 1. (D) Same as in (C) for recordings in Lis mutants. Physiological properties are less capable of predicting morphological cluster in Lis mutant mice.

Basket cell-principal cell innervation biases are differentially affected in the Lis1 mutant hippocampus

Having gained insight into how the heterozygous *Pafah1b1* mutation impacts the development of principal cell properties of positioning, embryonic birthdate, morphology and intrinsic physiology, we next wondered how ectopic calbindin cells were integrated into the local synaptic network of CA1. Prior studies have suggested a preferential and complementary innervation bias among two types of local basket cells found in the CA1 subfield – parvalbumin-containing (PV) and a subset of cholecystokinin-containing (CCK) inhibitory interneurons. PV-expressing basket cells preferentially innervate deeply situated calbindin-negative principal cells, while CCK-expressing interneurons have a similar bias, but for superficial calbindin positive principal cells (Lee et al., 2014; Valero et al., 2015; Valero and de la Prida, 2018). We wondered if these innervation patterns were present in the Lis1 mutant despite ectopic cellular layering, which might shed light on how positioning and layering effect synaptic network development of brain structures.

To begin to assay this network feature in our Lis1 mutants, we first asked where these two types of basket interneuron somas were positioning in mutant mice. Immunohistochemical staining experiments were performed using antibodies against PV and CCK (Figure 5A and B). The somas of stained interneuron classes are plotted in binned and normalized histograms in Figure 5B, left and right for PV and CCK, respectively (filled bars for Wt dashed bars for Lis1-MUT).

Vertical dotted lines show the approximate location of the wild type principal cell layer. Note that for this figure, somatic position is measured from the alveus/cortical border toward the s. radiatum across the entire radial depth of CA1, as opposed to how it is measured when examining principal cell layer depth, meaning 0 corresponds to the deepest position in this plot. This measure is more appropriate when looking at non-principal cells and overall hippocampal distributions (compare with Figures 3F and 4A), as these interneurons often position on the edges of, or outside of the PCL. Our data indicate that both PV- and CCK-containing cell types have undergone superficial radial shifts, that is, the cell bodies have moved toward the s. radiatum. Notably, this is opposite the direction in which calbindin positive principal cells are shifted in *Lis1* mutants (Figures 1 and 2). Overall, PV-containing somatic shifts appear less severe than CCK-containing shifts, but in both cases a few drastically shifted somas were observed (right tail of dashed histograms). To begin to probe synaptic network development under heterotopia, we performed high-magnification immunohistological staining experiments with four simultaneously visualized channels (Figure 5C-F).

This permitted the identification of inhibitory synapses on the somas of calbindin-positive and calbindin-negative principal cells (Figure 5C, *left* and *right* panels, respectively) in normal and *Lis1* mutant littermates (5C vs E and 5D vs F, for PV and CB1R respectively). First, putative inhibitory boutons are automatically identified in the corresponding stain (Pv or CB1-R, top panels, blue staining). These putative pre-synaptically localized boutons are then filtered by proximity to a postsynaptic inhibitory synapse marker, gephyrin – yielding ‘true’ inhibitory puncta (synthetic spheres in bottom panels, gephyrin staining not shown). These puncta are then counted if they are within 0.2 μm or less of a principal cell soma – which are demarcated by the

WFS1 antibody (green). Six calbindin positive and six calbindin negative principal cells in CA1 of mutants and non-mutant littermates are used for each image, yielding a single data point – that is to say, filtered inhibitory puncta are counted on somas of six calbindin positive and six calbindin negative principal cells. Six cells are used because sections and images taken are extremely thin to minimize Z-axis problems. We want to analyze ectopically positioned calbindin-expressing principal cells, and there are a limited number of these in any given image. The counts on calbindin-positive somas are divided by counts on calbindin-negative somas yielding a bias ratio (no. of Calb-positive PCs/no. of Calb-negative PCs). Numbers greater than one indicate a preference for calbindin-expressing principal cells. See Materials and methods for additional information.

PV-expressing basket cells preferentially innervated calbindin-negative principal cells in both mutant and wild-type mice (Figure 5G; PV-calbindin preferences: 0.74 ± 0.05 , 0.63 ± 0.11 for Wt and mutant, respectively, $p=0.55$, each point represents 12 cells from a slice, $n = 3$ pair of littermates from three litters). In experiments where the PV channel stain was replaced with a Cb1-R antibody, known to selectively stain presynaptic terminals of CCK-expressing basket cells, we noted a preferential innervation of calbindin-expressing post-synaptic targets in normal type that was absent from the *Lis1* mutant mouse (Figure 5H; CB1-R-calbindin preferences: 1.32 ± 0.04 , 1.02 ± 0.09 for Wt and *Lis1*-MUT, respectively, $p=0.02$). Which suggested that at least from an immunohistological level, CCK-expressing basket targeting onto ectopic calbindin-positive principal cells was disrupted.

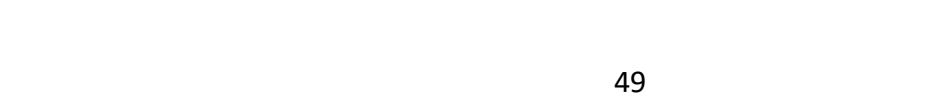
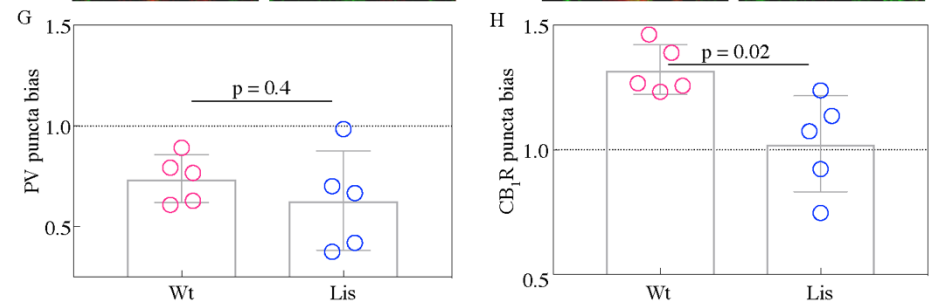
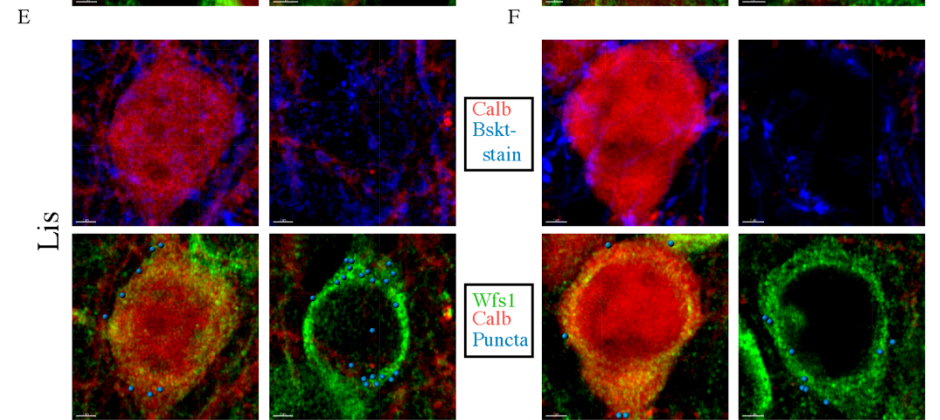
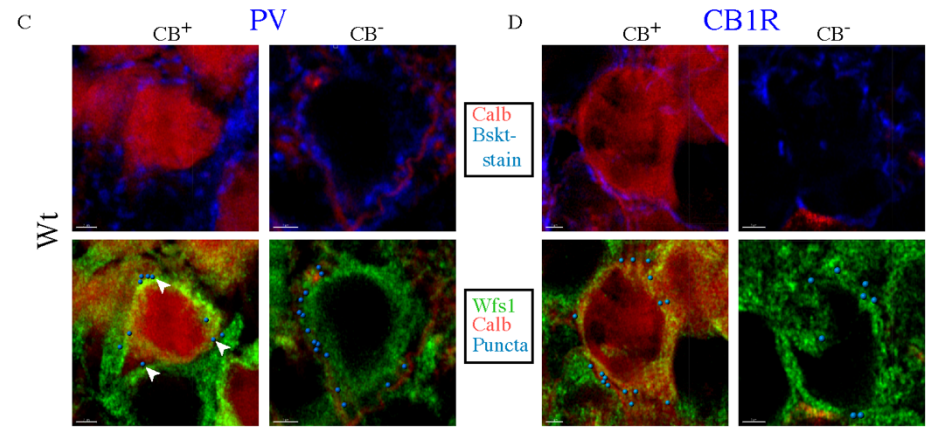
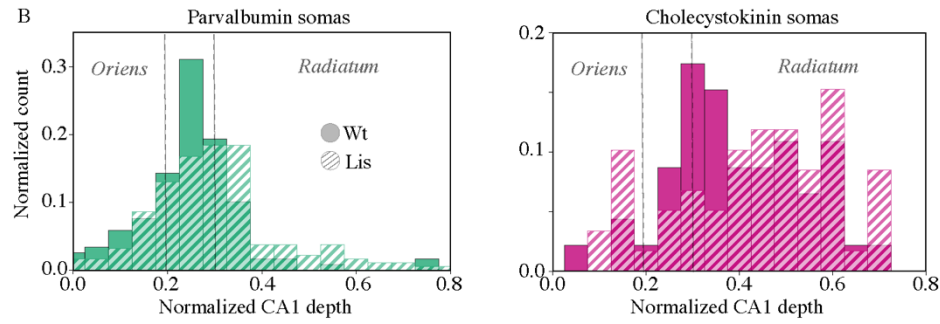
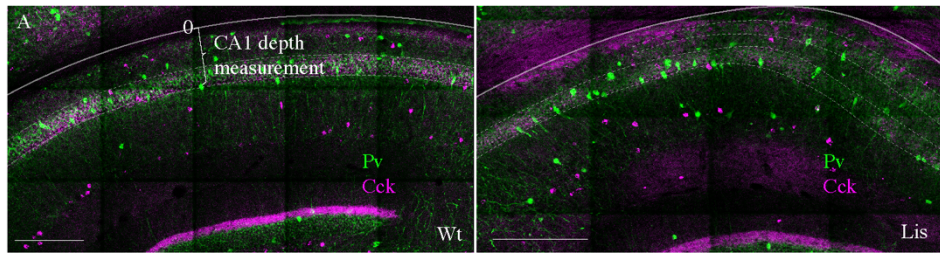


Figure 5. CCK-expressing basket cells have decreased innervation preference with ectopic calbindin-positive principal cells.

(A) Low-magnification images showing the locations of parvalbumin and cholecystokinin-expressing interneurons in the CA1 hippocampus. Note the CA1 depth measurement from the back of the oriens – this measure is more appropriate for assessing somatic position within the larger CA1 structure, as opposed to PCL depth used elsewhere in this study. Scale bars are 350 μm . (B) Normalized histograms of basket cell soma depth measurements along the radial axis of CA1, both PV- (*left*) and CCK-containing (*right*) inhibitory interneuron somas show modest superficial shifts in Lis1-MUT mice. (C) High-magnification images of a staining experiment for the quantification of PV-containing inhibitory puncta from control littermate samples. *Left*, an example CB-expressing principal cell. *Right*, an example non-CB-expressing principal cell. The top row shows calbindin and parvalbumin staining, the bottom row shows the same cells with calbindin, Wfs1 staining which was used to draw the cell border, and the puncta derived from the parvalbumin staining shown above (arrows point to a few in the first panel) – these puncta are filtered for proximity to a postsynaptic gephyrin puncta (channel not shown). (D) Same as in (C), except the interneuron staining is for the cannabinoid receptor 1, highly expressed in the terminals of CCK-expressing interneurons. (E and F) Same as the corresponding above panels, but for samples from Lis1-MUT littermates. Scale bars are 2 μm . (G) PV puncta bias summary. PV puncta had a modest preference for non-calbindin expressing principal cells in both non-mutant and mutant slices. PV-calbindin preference: 0.74 ± 0.05 and 0.63 ± 0.11 innervation biases for wild-type and mutants, respectively, $p=0.55$, each point represents 12 cells from a slice, $n = 3$ pairs of littermates from three litters. (H) Same as in (E), but for experiments where the PV antibody was replaced by the CB1-R antibody. Non-mutant CCK baskets displayed a preference for calbindin-expressing principal cells that was lost in Lis1-MUT mice. CB1-R-calbindin preference: 1.32 ± 0.04 , 1.02 ± 0.09 for wild-type and mutant respectively, $p=0.02$. Scale bars for C-F are 2 μm .

Monosynaptic CCK-mediated inhibition onto calbindin-positive principal cells is disrupted in

CA1 of the Lis1 mutant

In order to better understand the role of CCK-expressing inhibitory cell networks in the face of pyramidal cell heterotopia and to further the observations shown in Figure 5 at a functional level, whole-cell recordings were made from principal cells in CA1 in the presence of excitatory synaptic transmission blockers (APV 50 μM and DNQX 10 μM). Monosynaptic inhibitory events were evoked using a stimulation electrode placed locally in the PCL of CA1, and omega-conotoxin (1 μM) was applied to selectively inhibit vesicle release from CCK-expressing interneurons (Figure

6; Heft and Jonas, 2005). Example traces from four groups are shown in Figure 6C, from left to right, Wt complex, Wt simple, Lis1-MUT complex, Lis1-MUT simple. Baseline events are in black, and post wash-in data are in gray. In littermate controls, conotoxin reduced monosynaptically evoked IPSCs to $52.5 \pm 3.9\%$ of baseline amplitudes in complex cells, while events in simple cells were reduced to $75.6 \pm 8.3\%$ of baseline amplitudes, consistent with our observation that complex cells are preferentially targeted by CCK-containing interneurons (Figure 6D (*left*), $p=0.03$, $n = 8$ Wt and 8 Lis1-MUT cells). In Lis1 mutant mice this differential CCK-containing inhibitory input was not detected, as conotoxin reduced eIPSCs to $48.2 \pm 16.4\%$ of baseline and $60.2 \pm 7.8\%$, for complex and simple cell subtypes respectively (Figure 6D (*right*), $p=0.53$ $n=5$ and 13).

We next repeated this experiment using an antagonist known to inhibit release from parvalbumin-expressing interneurons, omega-agatoxin IVA (250 nM). Example traces for the four subtypes before and after agatoxin application are shown in Figure 6E (wash-in data in gray). In control mice, agatoxin reduced monosynaptically evoked eIPSCs to $42.01 \pm 6.2\%$ of baseline in complex cells, events in simple cells were reduced to $9.5 \pm 0.7\%$ of baseline amplitudes, signifying that events in simple cells were more dependent on PV-expressing basket cell input (Figure 6F (*left*), $p=0.003$, $n = 6$ complex and 4 simple cells). In Lis1 mutant mice agatoxin reduced eIPSCs to $49.6 \pm 5.8\%$ of baseline and $14.2 \pm 3\%$, for complex and simple cell subtypes, respectively (Figure 6F (*right*), $n = 6$ and 7, $p=0.0002$). In comparing both interneuron networks between genotypes, data suggest that CCK innervations are more perturbed than PV in Lis1 mutants. In both monosynaptic wash-in experiments representative traces come from single examples, but readers should attend to the spread of the points particularly in the mutant data sets. We believe

this variance to largely stem from differences in severity of heterotopic banding between animals or slices. For example, not all *Lis1* mutant slices display severe heterotopic banding, but instead a scattering of cells at various points of CA1. Additionally, it is difficult to assess the degree of banding prior to making whole-cell recordings. Hence, some calbindin-positive complex cells in mutants may in fact come from the superficial heterotopic band, while others (the ones we select for when doing immunohistochemical analysis particularly in Figure 5) are located ectopically in the deeply positioned heterotopic band. In most cases, we see the greatest deficits in the wash-in experiments, in these heterotopic principal cells, and less severe deficits in the more normally positioned complex cells in the *Lis1* mutants. While this complicates analysis by increasing the putative groups or obscuring relationships when grouping all cells by shape rather than position and shape, the data seem to hint there is indeed something about the disrupted layering itself, or the heterotopic positioning that is contributing to the failures in microcircuit formation observed here.

Having probed monosynaptic inhibitory circuitry onto putative calbindin-positive and -negative cells, we next examined feedforward disynaptic inhibition onto CA1 principal cells in normal and *Lis1* mutant mice. Superficial cells have been previously shown to exhibit a comparatively higher level of excitatory drive during feedforward circuit activation (large EPSCs per unit of IPSC, Valero et al., 2015). Cells were voltage clamped at -70 mV and $+10$ mV to measure the Schaffer collateral-mediated monosynaptic excitatory and disynaptic inhibitory drive (Figure 6G). Excitatory transmission was subsequently blocked (APV 50 μ M and DNQX 20 μ M), to allow the subsequent isolation of the disynaptic feedforward inhibitory drive from the total inhibitory component. Inhibition:excitation (IE) ratios were positively correlated with

somatic depth in the PCL for wild-type littermates, but not Lis1 mutants (Figure 6H; Wt $r = 0.4$, Lis1-MUT $r = 0.05$). When recorded cells were sorted by complex and simple morphologies complex cells had lower IE ratios in both wild-type and Lis 1 mutant mice (Figure 6I, Wt complex 3.15 ± 0.39 , simple 5.7 ± 0.95 , $p=0.02$ $n=23$ complex and 23 simple; Lis1-MUT complex 3.02 ± 0.49 , simple 5.03 ± 0.76 , $p=0.03$ $n=21$ complex and 17 simple cells). While their resulting ratios were predictive of sub-type, neither EPSC or IPSCs alone were significantly associated with depth or cell subtype (data not shown). EPSCs displayed depth correlations of $r = 0.16$ and $r = 0.07$ for wild-type and Lis1-MUT experiments, respectively. Neither excitatory nor inhibitory events differed significantly between principal cell shapes. IPSCs had a somatic depth correlation value of 0.2 wild-type littermates and 0.01 for mutants.

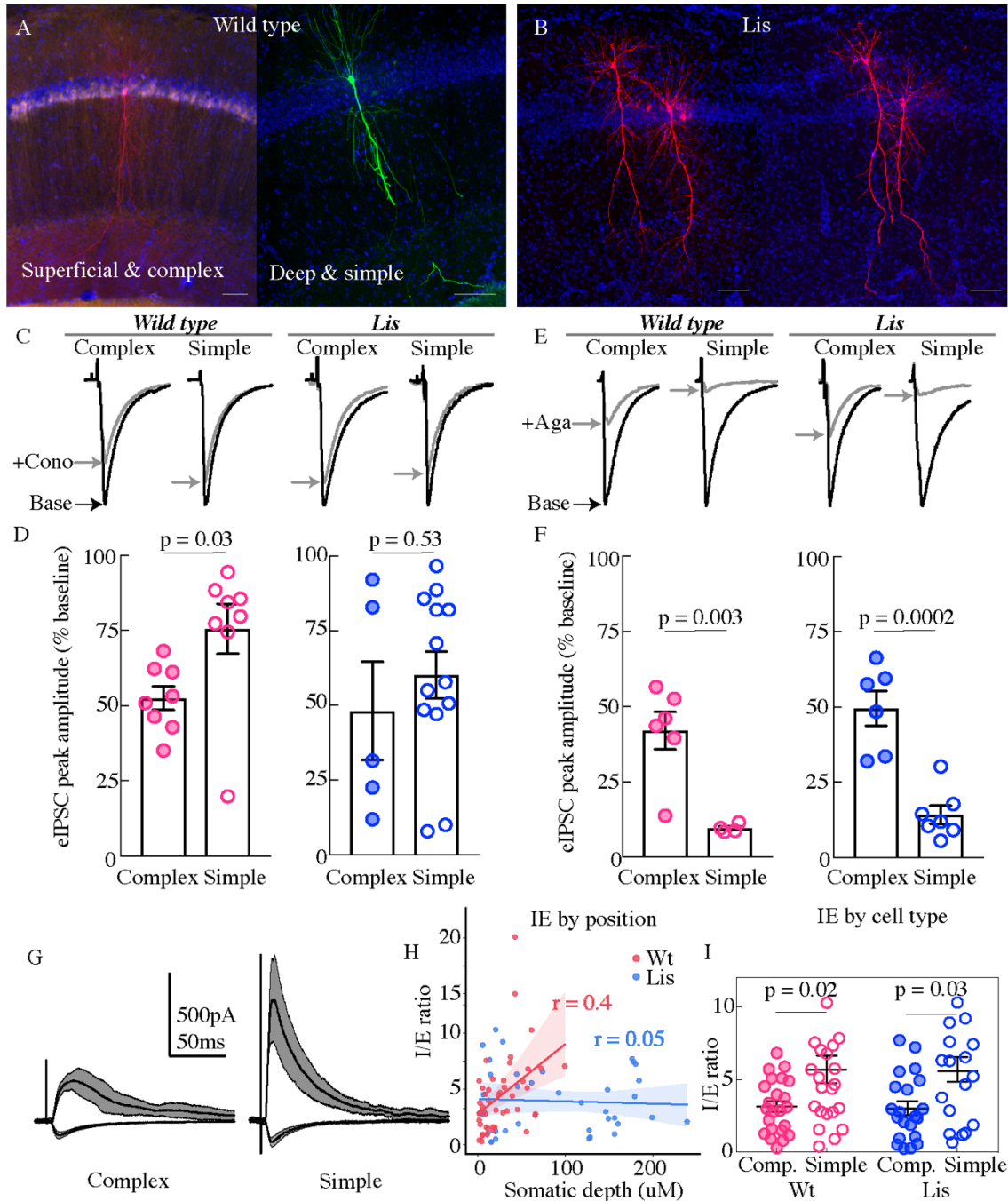


Figure 6. Physiological assays of network function within CA1.

(A and B) Cell recoveries from normal type and Lis1 mutant experiments. Scale bars are 85 μm . (C) Normalized example traces from pre- and post-wash in (dashed) of omega-conotoxin (1 μM), from left to right, a normal-type complex and simple recordings, followed by Lis mutant complex and simple examples. Stimulation for monosynaptic experiments was delivered locally in the CA1 PCL. (D) Quantification of the percent reduction in the evoked IPSC 10–12 mins after drug application. Wt: complex $52.5 \pm 3.9\%$, simple $75.6 \pm 8.3\%$; Lis1-MUT: complex $48.2 \pm 16.4\%$; simple $60.2 \pm 7.8\%$, $n = 8, 8, 13, 5$, respectively. (E) Example traces as in (C) but for omega-

agatoxin experiments (250 nM). (F) As in (D) but for agatoxin. Wt: complex $42.0 \pm 6.2\%$, simple $9.5 \pm 0.7\%$; Lis1-MUT: complex $49.6 \pm 5.8\%$; simple $14.2 \pm 3.0\%$, n = 6, 4, 6, 7, respectively. (G) Example traces for monosynaptic EPSCs (excitatory, inward current), and disynaptic feedforward IPSCs (inhibitory, outward current) evoked by stimulation of Schaffer collaterals, from a simple and complex recovered cell morphology in normal type. (H) IPSC amplitude/EPSC amplitude plotted by somatic PCL depth. (I) Same data as in (H) sorted by cell sub-type. Wt: complex 3.15 ± 0.39 , simple 5.70 ± 0.95 ; Lis1-MUT: complex 3.02 ± 0.49 ; simple 5.03 ± 0.76 , n = 23, 23, 21, 17, respectively.

Lis1-MUT mice display robust extracellular oscillations but are less synchronous across heterotopic bands

Using extracellular oscillations measured in vitro we next sought to assay alterations in network level function resulting from the cellular heterotopia present in our Lis1 mutants. Both wild-type and Lis1 mutant slices were capable of producing robust gamma oscillatory activity (ranging from 18 to 50 Hz), in response to application of 20 μ M carbachol (Figure 7; Buhl et al., 1998; Fellous and Sejnowski, 2000; Fisahn et al., 1998). Slices from Lis1 mutants produced slightly higher frequency gamma oscillations than non-mutants (Wt 24.9 ± 1.7 Hz, Lis1-MUT 31 ± 1.1 Hz, $p=0.005$ n=20 and 14, respectively) (Figure 7B–D). Subsequent addition of the synthetic CB1R agonist, WIN-55,212–2 (WIN) (2 μ M), did not alter the peak frequency of the oscillations in normal type nor mutant recordings (Figure 7D) but caused a significant decrease in peak power in normal type recordings (Figure 7E), but not in Lis1-MUT mice suggesting that CCK-networks in mutants are less involved in gamma oscillation generation than in wild-type littermates (Wt +WIN 0.93 ± 0.03 vs CCh alone $p=0.03$, Lis1-MUT +WIN 1.02 ± 0.04 vs CCh alone $p=0.69$; n = 20 and 14 non-mutant and mutant, respectively).

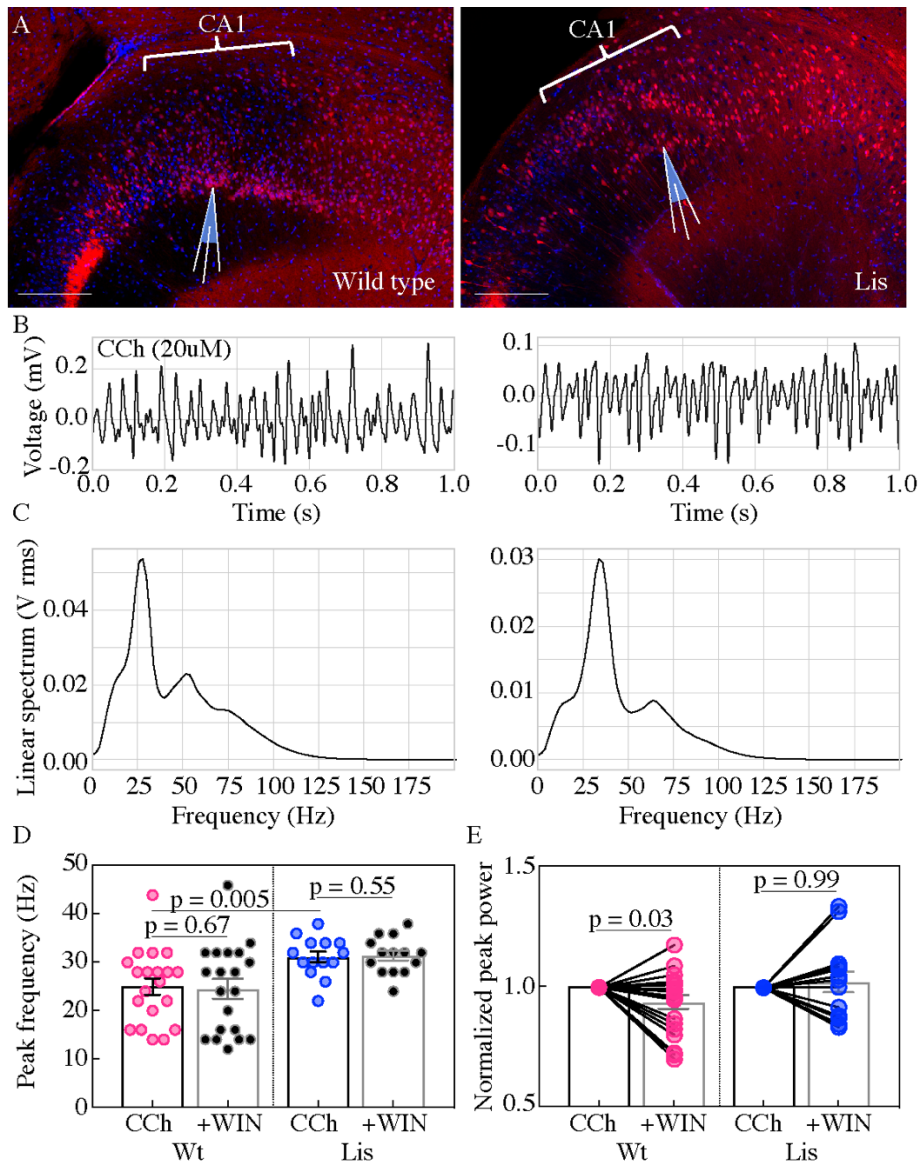


Figure 7. Lis mutants display robust carbachol-induced oscillations.

(A) Normal type (*left*) and mutant (*right*) images from ventral hippocampus in *Calb1-cre:Ai14* mice. Note the second layer of deeply positioned calbindin expressing principal cells in the Lis mutant. Scale bars are 200 μ m. (B) One second of data during carbachol induced activity from radiatum side electrodes in normal type and mutant recordings, respectively. (C) Power spectra computed for each of the above example recordings. (D) Summary peak frequency data for wild-type and Lis mutant experiments, in carbachol alone, and with addition of WIN-55 (Cb1-R agonist, 2 μ m). Wt CCh 24.88 ± 1.7 Hz, +WIN 24.4 ± 2 Hz, Lis1-MUT CCh 31 ± 1.1 Hz, +WIN 31.3 ± 1 Hz. (E) Summary data as in (D) but for normalized V_{rms} power at the peak frequency. Wt +WIN 0.93 ± 0.03 vs CCh alone $p=0.03$, Lis1-MUT +WIN 1.02 ± 0.04 vs CCh alone $p=0.69$; $n=20$ and 14 wild-type and mutant respectively. Pre-vs-post wash p values represent paired t tests.

In an additional series of experiments, a second electrode was placed in the same radial axis as the first approximately 150 μm deeper, so that in normal type slices one electrode targeted the radiatum side of the PCL while the other targeted the oriens side (Figure 8A). In the Lis1-MUT slices, electrodes were placed in different heterotopic bands but still in the same radial axis. This allowed for analysis of the correlation and synchronicity of oscillations across the normal and heterotopic layers of CA1 (Figure 8). Electrode location was preserved in analysis such that comparisons are always made in a deep vs superficial manner. Examples of simultaneous one second recordings are shown for the oriens (*top*) and radiatum (*bottom*) side electrodes in Figure 8B (Wt on *left*, Lis1-MUT on *right*). Dashed vertical lines show peak alignment for each example. Associated cross-correlation plots between these electrodes are displayed in Figure 8C (Wt *left*, Lis1-MUT *right*); note the +0.7 ms peak in offset in the wild-type experiment, and -2.7 ms peak offset in the Lis1 example. Wild-type and Lis1 mutant slices were capable of producing correlated oscillatory activity (Figure 8D; Wt 394.6 ± 80.0 , Lis1-MUT 394.2 ± 60.8 , $p=0.99$ $n=20$ and 14). However, examining the time-shifts obtained from cross correlation analysis (how far one signal is peak shifted from another in time) we noted that Lis1-MUT mice displayed significantly less temporally correlated oscillations between the two electrodes (Figure 8E; Wt: $+1.01 \pm 0.8$ ms, Lis1-MUT: -1.8 ± 0.79 , $p=0.02$ $n=20$ and 14) suggesting that while both heterotopic bands participate in the ongoing oscillation, their separation in anatomical space or deficits in basket cell network connectivity erodes the correlated activity between the bands. Application of the CB1R agonist WIN-55 produced modest decreases in wild-type cross-correlation values but not in the Lis1 mutants (Wt: + WIN 333.9 ± 71.9 , vs baseline $p=0.04$ $n=20$; Lis1-MUT: + WIN 427.2 ± 84.13 , vs baseline $p=0.43$ $n=14$) suggesting a diminished

role for CCK-containing interneuron networks in the mutant mouse. WIN-55 application did not have a significant impact on the time-shift between deep and superficial channels in either genetic background (Wt: + WIN 0.68 ± 0.52 ms, vs baseline $p=0.62$, Lis1-MUT: + WIN -0.41 ± 1.23 ms, vs baseline $p=0.21$).

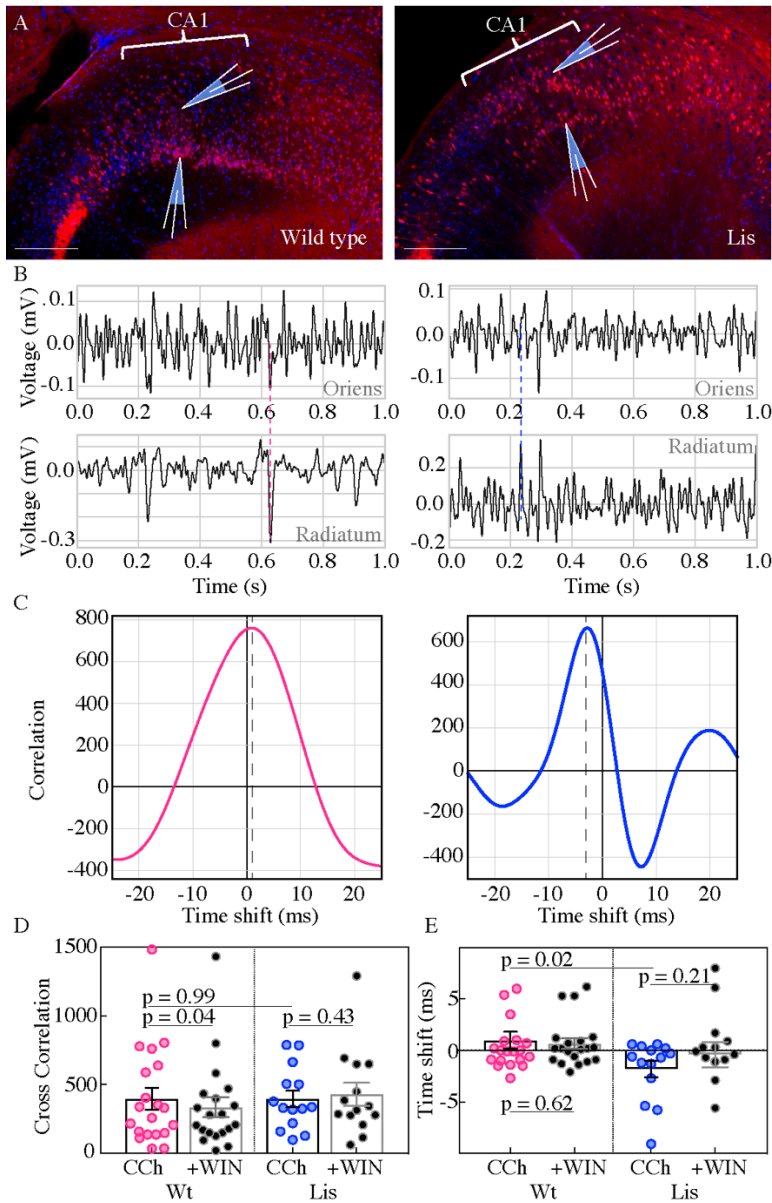


Figure 8. Carbachol oscillations in Lis1 mutants are less synchronous across CA1 heterotopias. (A) Normal type (*left*) and mutant (*right*) images from ventral hippocampus showing the positioning of dual electrode recordings, one from the s. radiatum and a second s. oriens side electrode in the same radial plane. Scale bars are 200 μ m. (B) One second of simultaneous

recordings from the deep (top) and superficial (bottom) electrodes, for wild-type (*left*) and Lis mutant (*right*) example experiments. Dashed lines highlight peak alignment between electrodes – note the blue line intersecting near a trough in the top trace, and a peak in the bottom. (C) Cross correlation plots for the example experiments shown in (B). Correlation values are arbitrary units. (D) Summary data for non-mutant and Lis1-MUT experiments in carbachol and after WIN-55 wash-in. Wt CCh 394.6 ± 80 , +WIN 333.9 ± 72 , Lis1-MUT CCh 394.2 ± 60.8 , +WIN 427.2 ± 84.1 . (E) Summary for the millisecond timing of peak correlation shifts shown in (D). Wt CCh 1 ± 0.8 ms, +WIN 0.68 ± 0.5 ms, Lis1-MUT CCh -1.8 ± 0.8 ms, +WIN -0.4 ± 1.23 ms; n = 20 and 14 wild-type and mutant respectively. Pre-vs-post wash p values represent paired t tests.

DISCUSSION

Cellular heterotopias arising from various genetic and environmental factors carry with them a poor prognosis for the affected individual, including severe mental disability, increased seizure risk, and shortened life span (De Wit et al., 2011). The degree to which these effects are a direct result of the heterotopia itself (a lack of layers) or related to the role of the mutated genes in other processes remains unclear. That is to say, it is unknown to what extent any of the disease phenotypes associated with Lissencephaly are the result of disrupted layering and cellular misposition during embryonic development. However, by making relative comparisons between cell subtypes and their integration into the local circuitry separately in wild-type and mutant animals, we are able to garner some insight into cellular maturation, subtype identity development, and susceptibility of key circuit motifs to a loss in layering.

In the present work, we first investigate the heterotopic banding observed in area CA1 of the Lis1 mutant mouse in order to determine if there is a pattern to the splitting of these excitatory cell populations – that might reflect naturally ‘embedded’ layers in the wild type CA1. To this end, we demonstrate that calbindin-expressing principal cells are preferentially affected by cellular heterotopia in CA1, where they are proportionately relegated to the deeper cellular layer – opposite of their normal superficial positioning in the PCL (Figure 1; Slomianka et al.,

2011). After confirming that these cells are the same embryonically derived population (Figure 2), namely late-born calbindin expressing, we asked to what degree their intrinsic development reflected the differences between calbindin-positive and calbindin-negative PC subtypes in wild-type animals, and if relative differences between the two population were preserved (Figures 3 and 4). While there was an effect of stunted arborization in comparison to normal type calbindin cells, Lis1 calbindin cells retained their complex morphology relative to within animal non-calbindin expressing principal cells. Intrinsic physiological properties appear more disrupted in Lis1 calbindin-expressing principal cells; however, several properties showed greater differences or trended toward significant differences when separated by putative calbindin expression, as opposed to somatic positioning – suggesting again that subtype was a stronger influence than layering in the determination of these properties. It is unclear if the intrinsic physiological differences between calbindin positive PCs in normal and Lis1 mutants reflected other roles of the *Pafah1b1* protein directly, compensatory changes of ectopic cells, or are the result of cellular development in an ectopic position – the first two seem more likely given findings from other mis-lamination models (Salinger et al., 2003; Wagener et al., 2016; Caviness and Rakic, 1978), although insufficient circuit integration and activity is known to alter cellular development in cortex (De Marco García et al., 2011).

We next turned our attention to the integration of these ectopic calbindin-expressing principal cells into the CA1 basket cell network. Staining experiments suggest that CCK expressing basket cell synapses were specifically altered to a greater extent than PV networks onto ectopic calbindin principal cell targets (Figure 5). This finding was confirmed by monosynaptic inhibition experiments, which showed reduced sensitivity of ectopic calbindin-expressing principal cells to

omega-conotoxin, which selectively impedes CCK cells –suggesting these connections are sparse or otherwise underdeveloped (Figure 6, left). Conversely, PV cell networks seemed substantially more resilient, which is not so surprising given that these cells occupy deeper positions within CA1, and their preferred synaptic targets are not substantially mispositioned under the cellular heterotopia present in Lis1 (Figure 5A and B; Lee et al., 2014). Interestingly, we observed greater spread in the mutant monosynaptic inhibition data than the wild-type counterpart. As briefly mentioned in the associated text, we suspect the spread stems from differences in the degree of heterotopic banding in any particular animal or slice. Data points showing greater inhibition deficits were often the cells whose soma were most ectopically located (calbindin cells far in the deeper heterotopic band). Notably, in Figure 5 we select for these cells in our immunohistochemical bouton analysis, but this is much harder to do for whole-cell recordings – hence grouping the data by shape alone means some cells will be complex and calbindin expressing, but somewhat normally located. Others will be ectopically located complex cells – the population more likely to suffer from the developmental deficit. While this makes the data harder to gather, group, and analyze, this would suggest that some of the network deficits described here are not a de facto consequence of the Lis1 mutation – instead being tied to local CA1 architecture or loss of layering under heterotopia.

Disynaptic inhibition experiments also support the notion of PV networks being more robust under cellular heterotopia (Figure 6, *bottom*). Feed-forward inhibition is much stronger onto PV baskets than their CCK expressing counterparts, making this largely a test of PV network connectivity (Glickfeld and Scanziani, 2006). Additionally, depolarization to +10 mV (as done in these experiment) drives depolarization-induced suppression of inhibition in CCK-basket cells,

largely removing them from this assay (Freund and Katona, 2007; Lee et al., 2010; Neu et al., 2007). In sorting these experiments by principal cell sub-type, we observed that ectopic calbindin-expressing principal cells retained their relatively high excitability (low I/E ratios), suggesting that parvalbumin cells did not start to inappropriately target deeply positioned, ectopic calbindin PCs.

Groups working in a related model of cellular heterotopia, the Reeler mouse which has severely disorganized cortical and hippocampal principal cell layering, previously reported that excitatory and inhibitory cells are produced in approximately the correct proportions, that ectopic cells retain expression of their correct markers, morphology of cell types is generally conserved, and their intrinsic physiological properties are largely unperturbed on a network level (Wagener et al., 2016; Boyle et al., 2011; Caviness and Sidman, 1973; Guy and Staiger, 2017; Guy et al., 2017). Despite differing genetic causes, the present study supports these findings that brain development is surprisingly robust despite mis-lamination. An interesting caveat, however, is that in the present work and other studies of cellular heterotopias, morphological development and orientation of principal cell dendrites appear stunted and meandering (Figure 3; Guy et al., 2015; Stanfield and Cowan, 1979). In the Reeler mouse synaptic network development was also remarkably intact, as thalamocortical and intracortical connectivity, cellular tuning properties to stimuli, and even animal behavior seem only minorly altered if at all (Salinger et al., 2003; Wagener et al., 2010; Wagener et al., 2016; Guy et al., 2015). From a broad perspective, this is in agreement with the present work in the *Lis1* hippocampus, as feed-forward properties onto PC subtypes retain their relative excitabilities, and *Lis1* slices retain their ability to generate gamma oscillations (Figure 7).

Interestingly, we observed higher peak oscillation frequency in Lis1 mutant experiments than normal type (Figure 7D). One possible interpretation of this result is that CCK-expressing interneuron networks tend to generate lower frequency gamma, and when disrupted in Lis1 mutants, networks become more dependent on alternative faster oscillation mechanisms such as greater reliance on parvalbumin cell networks. These results may reflect biological differences in hyperexcitability that predispose these mice and human patients to seizures – further study is required to determine if more heavily banded hippocampal PCL regions in mutant animals have a greater propensity to act as seizure foci. In the power domain, measurements are sensitive to differences in electrode placement between experiments, as this cannot be ruled out particularly as the cell layer positioning is unruly in Lis1-MUT mice; power data from these recordings was normalized and only compared within experiment to wash-in values (Figure 7E). Non-mutant slices showed power decreases in the presence of the cannabinoid receptor agonist WIN-55, while Lis1 mutant slices were non-responsive to this compound. These data add to our immunohistochemistry and monosynaptic physiology experiments in suggesting deficits in the CCK-basket cell networks of CA1 under heterotopia as Lis1 slices are largely not affected by WIN-55 application.

Comparing recordings from two electrodes in Figure 8 revealed that cross correlation values were relatively similar between wild type and mutant mice, but time-shifts or synchronicity between channels were significantly different (Figure 8E). It seems likely that timing differences in gamma-oscillations arise from the physical separation of current sinks and sources under Lis1-MUT heterotopia, and not as a result of the CCK-innervation deficit described above, as these measures were largely unchanged by WIN-55 application in normal-type mice, however,

that possibility cannot be ruled out (Hájos et al., 2000; Soltesz and Deschênes, 1993). It is worth noting that the time-shifts under baseline conditions in the mutants are opposite in direction than that of non-mutants. In that respect, they roughly mirror the physical inversion of PCL lamina under Lis1-MUT cellular heterotopia.

Collectively, these findings bolster the notion that layers are in large part an epiphenomenon of neurogenesis, as has been hypothesized previously. Importantly, layer terminology has a correlated genetic component in wild-type mice as it is likely to capture a related embryonic pool of neurons. Therefore, when traditional studies refer to cellular layer, they are using it as a proxy for cellular genetic subtype, which is no longer the case in heterotopias (Guy and Staiger, 2017; Caviness and Rakic, 1978; Guy et al., 2015). In agreement with this line of reasoning, decades of work on synapse development are increasingly bolstering the ‘handshake hypothesis’ – where in molecular cues present on the surface of both putative synaptic partners confirm or reject synapse formation to aid in the establishment of appropriate and canonical circuitry over several scales of axon pathfinding (Harris and Shepherd, 2015; Margeta and Shen, 2010; Blakemore and Molnár, 1990; Molnár et al., 2012). The degree to which these genetic network wiring mechanisms are modified in an activity-dependent fashion afterward remains an area of active study (Sur and Rubenstein, 2005; De Marco García et al., 2011; Che et al., 2018). Importantly, the present study does identify a crucial network motif, CCK-interneuron targeting of calbindin positive principal cells, that is specifically disrupted in ectopic calbindin PCs in the Lis1-MUT mouse. Further work will be needed to determine if this is a genetically specified connection preference for calbindin-expressing principal cells, and why it might exhibit positional dependence.

It might not be so surprising to find specific defects in CCK-expressing synaptic connections as opposed to PV circuitry. CCK and PV expressing interneurons arise from different progenitor pools, in the caudal ganglionic eminence (CGE) and medial ganglionic eminence (MGE), respectively (Butt et al., 2005; Fishell, 2007). Additionally, CGE interneurons are developmentally lagged relative to MGE pools, as MGE cells are born first (Tricoire et al., 2011). Notably, later born basket cell populations (CCK basket cells), appear to be biased towards innervation of late born principal cell populations (superficial, calbindin expressing) in non-mutant animals. In fact, prior work has demonstrated that basket CGE derived populations wait until the first post-natal week to form synapses on principal cell somas in the PCL (Morozov and Freund, 2003). This network motif may represent a lopsided obstacle in the establishment of CA1 circuitry, as few if any of their putative synaptic targets remain on the radiatum adjacent side of the PCL under this form of cellular heterotopia (Armstrong and Soltesz, 2012). As CCK cell somas reside largely on the border between the PCL and the radiatum, in the *Lis1* hippocampus these basket cells are tasked with sending axons through the denser superficial PCL and passing through the inter-PCL space before finding their appropriate synaptic targets in the deeper heterotopic band. It remains to be seen whether this CCK specific defect is generalized to area CA1 in other cellular heterotopias, or *Lis1* specific, but it may suggest natural limits to the handshake hypothesis – after all if you are never introduced, you cannot shake hands.

MATERIALS AND METHODS

Animal care and breeding

All experiments were conducted in accordance with animal protocols approved by the National Institutes of Health. Pafah1b1^{+/-}/Fl male mice (provided by the laboratory of Anthony Wynshaw-Boris, Case Western Reserve University) were crossed with Sox2-cre females (provided by National Human Genome Research Institute transgenic core, Tg(Sox2-Cre)^{1Amc/J}). Sox2-cre females display cre-recombinase activity in gamete tissues, allowing us to genotype and select non-conditional Lis1-MUT mice without the cre gene in one generation. To identify mutant offspring, we designed a new forward primer (Recombined forward: AGTGCTGGGACAGAACTC, Reverse: CCTCTACCACTAAAGCTTGTTTC) from the previously published genomic sequences. These mice were bred to wild-type C57BL/6J mice (Jackson Labs stock no. 000664) and used for experiments. Both male and female Pafah1b1^{+/-} mice were used for recording and immunohistochemical experiments. Female Neurog2-Cre (provided by the laboratory of Rosa Cossart, INSERM Marseille, France) mice were used for cell birth-dating experiments after being crossed to a cre-dependent reporter line (R26R, Jackson Labs stock no. 32037) – which contain an EGFP reporter with a loxP flanked stop cassette. Calb1-cre mice were obtained from Jackson laboratories (stock no. 028532) and bred to Ai14 animals from also from Jackson (stock no. 007914).

Cellular birth-dating

Timed pregnancies were established between Pafah1b1^{+/-} males and tamoxifen inducible Neurog2-CreER:Rosa26 females. Tamoxifen administration in these pregnant mice induces cre-

recombination and subsequent eGFP expression in newly born neurons of developing mouse pups. Pregnant mothers were gavaged with tamoxifen (Sigma no. T5648) in corn oil (200–250 mL, 20 mg/mL) at various embryonic time points spanning days E12-17. Pups were genotyped and grown to P27-32 before perfusion and brain fixation in 4% paraformaldehyde in 0.1 M phosphate buffer for 2–4 hr at room temperature or 12 hr at 4°C. Brains were washed, transferred to 30% sucrose in 1x phosphate buffered saline and stored at 4°C. Sections (50–100 μ m) were cut on a frozen microtome and stained for calbindin protein (described below). Coronal hippocampal sections were confocally imaged under 20x magnification on a Zeiss confocal microscope, tiled, stitched in the Zen Black software package and post-hoc analyzed for colocalization of calbindin staining and eGFP expression using the Imaris analysis package (Imaris 9.3.1, Bitplane).

Immunohistochemistry

Standard staining procedures were used for most of the experiments and have been described previously (Chittajallu et al., 2013) but briefly, deeply anesthetized mice were transcardially perfused with 50 mL of 4% paraformaldehyde (PFA) in 0.1 M phosphate buffer (pH 7.6). Brains were post-fixed overnight at 4°C, then cryopreserved in 30% sucrose solution. Coronal sections were cut (50 μ m) on a frozen microtome. Prior to staining sections are washed in phosphate buffered saline (PBS), blocked and permeabilized with 0.5% triton X-100, 10% goat serum in PBS for 2 hr at room temperature while shaking. Primary antibodies are applied overnight at 4°C shaking at the appropriate dilution with PBS containing 1% goat serum and 0.5% triton X-100. The following day sections are washed, and a secondary antibody is applied for 1 hr at room

temperature while shaking at a dilution of 1:1000. For most experiments, a final DAPI staining was also used to show lamina of the hippocampus. Sections are then mounted and cover slipped with Mowiol. Primary antibodies: Calbindin (Millipore polyclonal rabbit, stock no. AB1778, 1:1000; or Swant monoclonal mouse 1:1000, stock no. 300); CCK (Frontier Institutes rabbit, stock no. CCK-pro-Rb-Af350, 1:1000).

For quantification of inhibitory puncta the procedure was similar with a few adjustments. Coronal sections (50 μm) of dorsal hippocampus were cut, blocked with 10% donkey serum in 0.5% Triton X at room temperature for 2–4 hr. Primary antibodies were applied in phosphate buffered saline with 1% donkey serum and 0.05% triton X-100 at 4°C for 48 hr. Secondary antibodies were left at room temperature for 1–2 hr, before washing and mounting. Primary antibodies: Gephyrin-mouse (Synaptic Systems, CAT no. 147021, 1:1000), Wolfram syndrome 1 (Wfs1)-rabbit (Protein Tech, CAT no. 1558–1-AP, 1:5000), cannabinoid1-receptor (CB1-R)-guinea pig (Frontier Institutes, CAT no. CB1-GF-Af530, 1:5000), parvalbumin (PV)-goat (Swant, CAT no. PVG 214, 1:5000). Calbindin was visualized by using pups from crosses between Lis mutants and *Calb1-cre:Ai14* mice. Anti-donkey secondaries: Jackson Immuno Research laboratories Inc, AF 405 mouse (715-476-150), AF 488 rabbit (711-545-152), and AF 633 (706-605-148) guinea pig or goat (705-605-147) for visualization of CB1-R- and PV-positive baskets respectively (all 1:500). Images were captured on a Zeiss 880 confocal under 63x magnification using Zen Airyscan image processing. Between 25 and 30 Z-axis images were collected at Z-steps of 0.159 μm . Analysis was performed on a Max-IP from the first seven of these steps, accounting for 1.1 μm of tissue thereby minimizing Z-axis problems.

Images were quantified in Imaris 9.3.1 software. Twelve principal cells were selected using the Wfs1 staining – half of which were calbindin positive, and cell somas were traced. Gephyrin puncta (with an approximated size of $\sim 0.25 \mu\text{m}$) were automatically detected in the image and excluded if not within $1 \mu\text{m}$ of a cell soma. In parallel, inhibitory boutons were automatically detected from a pre-synaptic basket cell marker (parvalbumin in one set of experiments, CB1-R in the other). Inhibitory puncta were filtered for proximity to the post-synaptic gephyrin puncta ($1 \mu\text{m}$ or less), and further filtered by proximity to a principal cell soma ($0.2 \mu\text{m}$ or less). Remaining inhibitory puncta were counted on the somas of six calbindin positive, and six calbindin-negative principal cells. Dividing puncta counts on calbindin cells by those on calbindin-negative cells yielded synaptic innervation bias measurements such that counts from 12 cells are used to generate a single data point. A value less than one signifies an avoidance of calbindin-positive targets and numbers greater than one signifies a preference for calbindin-positive targets. The five points in each group originate from five different slices. Each slice is a ratio of inhibitory puncta on six negative cells, to six positive cells (12 cells total per point). Slices came from six different animals, three Lis mutant and three wild-type age-matched littermates, spanning three litters.

Principal cell reconstructions

Slices with biocytin filled cells were fixed (4% PFA and stored at 4°C) and processed for visualization using avidin conjugated dye. Slices were resectioned ($50\text{--}100 \mu\text{m}$) and DAPI stained so cells could be visualized, and their somatic depth could be assessed within the larger hippocampal structure. After staining, slices were imaged, and files were imported to

NeuroLucida (MBF Bioscience) cell tracing software. Once traced, data sheets were exported for apical dendrite shapes and connectivity profiles for each cell and processed in a custom python script to generate the LRI and ORI measurements later used for morphological clustering. This python script has been provided for use and exploration as a supplemental document to accompany this manuscript.

Slice preparation

Young adult mice (P20-40) were anesthetized with isoflurane before decapitation. Brains were immediately dissected in dishes of ice-cold dissection ACSF (in mM): 1 CaCl₂, 5 MgCl₂, 10 glucose, 1.25 NaH₂PO₄ * H₂O, 24 NaHCO₃, 3.5 KCl, 130 NaCl. ACSF was oxygenated thoroughly for 20mins by bubbling vigorously with 95% O₂ and 5% CO₂ beforehand. For measurement of cell intrinsic properties whole-cell recordings, mono-synaptic inhibition, and disynaptic inhibition experiments coronal slices were cut (350 μm) using a VT 1200S vibratome from Leica Microsystems. Slices were allowed to recover in an incubation chamber at 35°C in the same solution for 30 min. For oscillation experiments, the same extracellular slicing and recording solutions were used, and pipettes contained extracellular solution. Slices were cut horizontally (450 μm) from more ventral hippocampus, as oscillations were often extremely weak or all together lacking from coronal sections. We verified that similar migratory problems with the late-born calbindin population occurred in ventral hippocampus (Figure 7B). Oscillation experiment slices recovered for 15 min at 35°C before being transferred to a custom interface incubation chamber.

Whole-cell physiology

For electrophysiological recordings slices were transferred to an upright Olympus microscope (BX51WI) with a heated chamber (32°C, Warner Inst.) and custom pressurized perfusion system (~2.5 mL/min). Recording ACSF contained the following (in mM): 2.5 CaCl₂, 1.5 MgCl₂, 10 glucose, 1.25 NaH₂PO₄ * H₂O, 24 NaHCO₃, 3.5 KCl, 130 NaCl. Electrodes of 4–6 MOhm resistance (borosilicate glass, World Precision Instruments, no. TW150F-3) were prepared on Narishige (PP-830) vertical pipette pullers. Recording were collected using a Multiclamp 700B amplifier (Molecular Devices) with a Bessel filter at 3 kHz and Digitized at 20 kHz using a Digidata 1440A (Molecular Devices). Protocols were designed, executed and analyzed using the pClamp 10.4 software package (Molecular Devices). Liquid junction potentials were not corrected for and series resistance compensation was not applied. Series resistance was monitored throughout experiments using a –5 mV pulse at the start of each sweep and ranged from 12 to 32 MOhms, cells that varied by greater than 30% over the recording were not considered for analysis. Cells were biased to –70 mV in current clamp mode, and held at –70, –30, and +10 mV in voltage clamp mode depending on the requirements of the experiment. For basic properties and morphological recoveries, electrodes were filled with the following, in (mM): 130 K-glu, 0.6 EGTA, 10 HEPES, 2 MgATP, 0.3 NaGTP, 10 KCl. For monosynaptic inhibition experiments, eIPSCs were recorded at –70 mV using electrodes were filled with (in mM): 100 K-glu, 45 KCl, 3 MgCl, 2 Na₂ATP, 0.3 NaGTP, 10 HEPES, 0.6 EGTA; yielding an E_{cl} of –27 mV. eIPSCs were evoked by local stimulation for 5–10 min until a stable baseline was established, then omega-conotoxin GVIA (1 μM) was applied while eIPSCs were monitored for changes in amplitude. Similar experiments were performed washing in omega-agatoxin IVA (250 nM), with QX-314 (2 mM) added to the internal solution. Series

resistances for conotoxin: Wt: complex base 20.1 ± 2 wash 23.2 ± 2.9 , simple base 18.5 ± 3.8 wash 21.8 ± 4.5 MOhms. Lis1: complex base 18.4 ± 3 wash 21.2 ± 4.5 , simple base 17.4 ± 2.3 wash 19.9 ± 2.6 MOhms. Series resistances for agatoxin: Wt: complex base 20.8 ± 1.8 wash 24.7 ± 2.4 , simple base 18 ± 1.3 wash 20.5 ± 1.9 MOhms. Lis1: complex base 22.7 ± 1.8 wash 27.8 ± 1.9 , simple base 21.6 ± 1.4 wash 25.6 ± 2.4 MOhms. For feedforward I/E experiments electrodes contained (in mM): 135 Cs-MethaneSO₄, 5 NaCl, 4 MgATP, 0.3 NaATP, 10 HEPES, 0.6 EGTA, 5 QX-314 chloride salt, giving an E_{cl} of -69.7 mV. Internal solutions were adjusted for a pH of 7.4 using KOH and an osmolarity of 290 mOsm. Biocytin (2 mg/1 mL) was added to thawed aliquots before use. For feedforward inhibition experiments, pilot experiments where stimulation was delivered in CA3 did not include a wash-in of excitatory blockers as activation of direct monosynaptic inhibition was less likely. For most of the experiments, however, stimulation was delivered in the s. radiatum of CA1 and APV (50 μ M)/DNQX (20 μ M) was added to block glutamatergic transmission, permitting us to determine and subsequently subtract the monosynaptic component of the inhibitory response. These data were pooled. Experiments where IPSCs were not reduced by at least 30% by wash-in were excluded.

Extracellular field potentials

For LFP recordings, slices were transferred onto an interface chamber with two manipulator-controlled electrodes positioned under 25x visual guidance. Carbachol (20 μ M) was applied to induce slice oscillations. Recordings were made at 10 kHz, low and high pass filtered (8 and 100 Hz, respectively) and mean subtracted. Cross correlation was the max real value resulting from the inverse fast-fourier transformation of F_1 and F_2 ; where $F_1 = \text{fft}(\text{signal sample from channel 1})$,

and F_2 is likewise for channel 2, after a flip operation. Cross correlation summary values are the max cross-correlation value in the resulting vector C. The temporal shift between the two signals is the X-coordinate (in milliseconds), corresponding to this cross-correlation peak. Experiments were processed such that channel-1 and channel-2 always corresponded to the same side of the principal cell layer (deep vs superficial).

Data analysis

Initial data exploration and analysis was performed in custom Python scripts. For further plotting and statistical analysis, Graphpad Prism was used for physiological data. For soma positioning measurements and gephyrin puncta quantification, Microsoft excel sheets were used. Pre-clustering analysis was carried out in python or R using nbclust. K-means clustering was performed in Python using the Scikit learn clustering and decomposition packages. Both clustering routines were supervised (Figures 3 and 4), in that they expected K-means $n = 2$. For morphological clustering this was to replicate prior work and aid in identification of calbindin positive and negative principal cells. For physiological properties, we wished to ask if the two morphological populations might be reflected in our physiology data.

Statistics

P values represent Welch's t-tests for comparisons of two independent samples, unless otherwise noted. Student's paired t-tests were used for intra-sample (like inhibitory puncta) and pre-post wash comparisons. R values represent Pearson's cross-correlation unless otherwise noted. Quantification and error bars are standard error of the mean.

AUTHOR CONTRIBUTIONS

James A D'Amour, Conceptualization, Formal analysis, Funding acquisition, Investigation, Methodology, Writing - original draft, Writing - review and editing; Tyler Ekins, Data curation, Formal analysis, Investigation, Methodology; Stuti Ganatra, Xiaoqing Yuan, Data curation, Investigation, Methodology; Chris J McBain, Conceptualization, Resources, Data curation, Formal analysis, Supervision, Validation, Investigation, Writing - original draft, Writing - review and editing

ACKNOWLEDGEMENTS

The authors acknowledge with gratitude S Hunt and D Abebe for their assistance in tissue processing and animal management, G Akgul for designing new primers to genotype the recombined Pafafh1b1 allele, M Craig for help with analysis of oscillation experiments, D Calvigioni for assistance with Neurog2-cre experiments, C Bengtsson-Gonzales for analysis help and suggestions, and K Pelkey, R Chittajallu, T Petros, S Lee, W Lu. for feedback, comments, suggestions, and discussions during lab meetings. Finally, we are thankful to Dr. Wynshaw-Boris and his lab for providing the heterozygous floxed Pafafh1b1 mouse used to rederive the full het animal used here.

REFERENCES

- Angeivine** JB. 1965. Time of neuron origin in the hippocampal region an autoradiographic study in the mouse. *Experimental Neurology* 2:1–70.
- Anusha** DR. 2014. Lissencephaly: a review with a rare case report. *International Journal of Science and Research* 3:2319–7064.
- Armstrong** C, Soltesz I. 2012. Basket cell dichotomy in microcircuit function. *The Journal of*

- Physiology 590:683–694. DOI: <https://doi.org/10.1113/jphysiol.2011.223669>, PMID: 22199164
- Bannister** NJ, Larkman AU. 1995. Dendritic morphology of CA1 pyramidal neurones from the rat Hippocampus: I. branching patterns. *The Journal of Comparative Neurology* 360:150–160. DOI: <https://doi.org/10.1002/cne.903600111>, PMID: 7499560
- Blakemore** C, Molnar Z. 1990. Factors involved in the establishment of specific interconnections between thalamus and cerebral cortex. *Cold Spring Harbor Symposia on Quantitative Biology* 491–504.
- Boyle** MP, Bernard A, Thompson CL, Ng L, Boe A, Mortrud M, Hawrylycz MJ, Jones AR, Hevner RF, Lein ES. 2011. Cell-type-specific consequences of reelin deficiency in the mouse neocortex, Hippocampus, and amygdala. *The Journal of Comparative Neurology* 519:2061–2089. DOI: <https://doi.org/10.1002/cne.22655>, PMID: 21491433
- Buhl** EH, Tamas G, Fisahn A. 1998. Cholinergic activation and tonic excitation induce persistent gamma oscillations in mouse somatosensory cortex in vitro. *The Journal of Physiology* 513:117–126. DOI: <https://doi.org/10.1111/j.1469-7793.1998.117by.x>, PMID: 9782163
- Butt** SJ, Fuccillo M, Nery S, Noctor S, Kriegstein A, Corbin JG, Fishell G. 2005. The temporal and spatial origins of cortical interneurons predict their physiological subtype. *Neuron* 48:591–604. DOI: <https://doi.org/10.1016/j.neuron.2005.09.034>, PMID: 16301176
- Caviness** VS, Rakic P. 1978. Mechanisms of cortical development: a view from mutations in mice. *Annual Review of Neuroscience* 1:297–326. DOI: <https://doi.org/10.1146/annurev.ne.01.030178.001501>, PMID: 386903
- Caviness** VS, Sidman RL. 1973. Retrohippocampal, hippocampal and related structures of the forebrain in the Reeler mutant mouse. *The Journal of Comparative Neurology* 147:235–253. DOI: <https://doi.org/10.1002/cne.901470206>, PMID: 4682775
- Che** A, Babij R, Iannone AF, Fetcho RN, Ferrer M, Liston C, Fishell G, De Marco García NV. 2018. Layer I interneurons sharpen sensory maps during neonatal development. *Neuron* 99:98–116. DOI: <https://doi.org/10.1016/j.neuron.2018.06.002>, PMID: 29937280
- Chittajallu** R, Craig MT, McFarland A, Yuan X, Gerfen S, Tricoire L, Erkkila B, Barron SC, Lopez CM, Liang BJ, Jeffries BW, Pelkey KA, McBain CJ. 2013. Dual origins of functionally distinct O-LM interneurons revealed by differential 5-HT(3A)R expression. *Nature Neuroscience* 16:1598–1607. DOI: <https://doi.org/10.1038/nn.3538>, PMID: 24097043
- De Marco Garcia** NV, Karayannis T, Fishell G. 2011. Neuronal activity is required for the development of specific cortical interneuron subtypes. *Nature* 472:351–355. DOI: <https://doi.org/10.1038/nature09865>
- De Wit Marie-Claire** Y, de Rijk-van Andel J, Halley DJ, Poddighe PJ, Arts WFM, De Coo Ireaeus FM, Mancini GMS. 2011. Long-term follow-up of type 1 lissencephaly: survival is related to neuroimaging abnormalities. *Developmental Medicine & Child Neurology* 53:417–421. DOI: <https://doi.org/10.1111/j.1469-8749.2011.03937.x>
- DeFelipe** J. 1997. Types of neurons, synaptic connections and chemical characteristics of cells immunoreactive for calbindin-D28K, parvalbumin and calretinin in the neocortex. *Journal of Chemical Neuroanatomy* 14:1–19. DOI: [https://doi.org/10.1016/S0891-0618\(97\)10013-8](https://doi.org/10.1016/S0891-0618(97)10013-8), PMID: 9498163
- Deguchi Y, Donato F, Galimberti I, Cabuy E, Caroni P. 2011. Temporally matched subpopulations of selectively interconnected principal

- neurons in the Hippocampus. *Nature Neuroscience* 14:495–504. DOI: <https://doi.org/10.1038/nn.2768>, PMID: 21358645
- Di Donato N**, Chiari S, Mirzaa GM, Aldinger K, Parrini E, Olds C, Barkovich AJ, Guerrini R, Dobyns WB. 2017. Lissencephaly: expanded imaging and clinical classification. *American Journal of Medical Genetics Part A* 173:1473–1488. DOI: <https://doi.org/10.1002/ajmg.a.38245>, PMID: 28440899
- Dobyns WB, Das S. 2009. PFAH1B1-associated lissencephaly/subcortical band heterotopia. *Gene Reviews* 3:1993–2020.
- Fellous JM, Sejnowski TJ. 2000. Cholinergic induction of oscillations in the hippocampal slice in the slow (0.5-2hz), theta (5-12 hz), and gamma (35-70 hz) bands. *Hippocampus* 10:187–197. DOI: [https://doi.org/10.1002/\(SICI\)1098-1063\(2000\)10:2<187::AID-HIPO8>3.0.CO;2-M](https://doi.org/10.1002/(SICI)1098-1063(2000)10:2<187::AID-HIPO8>3.0.CO;2-M), PMID: 10791841
- Fisahn A**, Pike FG, Buhl EH, Paulsen O. 1998. Cholinergic induction of network oscillations at 40 hz in the Hippocampus in vitro. *Nature* 394:186–189. DOI: <https://doi.org/10.1038/28179>, PMID: 9671302
- Fishell G**. 2007. Perspectives on the developmental origins of cortical interneuron diversity. *Novartis Foundation Symposium* 21–35.
- Fleck MW**, Hirotsune S, Gambello MJ, Phillips-Tansey E, Soares G, Mervis RF, Wynshaw-Boris A, McBain CJ. 2000. Hippocampal abnormalities and enhanced excitability in a murine model of human lissencephaly. *The Journal of Neuroscience* 20:2439–2450. DOI: <https://doi.org/10.1523/JNEUROSCI.20-07-02439.2000>, PMID: 10729324
- Freund TF**, Katona I. 2007. Perisomatic inhibition. *Neuron* 56:33–42. DOI: <https://doi.org/10.1016/j.neuron.2007.09.012>, PMID: 17920013
- Glickfeld LL**, Scanziani M. 2006. Distinct timing in the activity of cannabinoid-sensitive and cannabinoid-insensitive basket cells. *Nature Neuroscience* 9:807–815. DOI: <https://doi.org/10.1038/nn1688>, PMID: 16648849
- Guy J**, Wagener RJ, Moock M, Staiger JF. 2015. Persistence of functional sensory maps in the absence of cortical layers in the somatosensory cortex of Reeler Mice. *Cerebral Cortex* 25:2517–2528. DOI: <https://doi.org/10.1093/cercor/bhu052>, PMID: 24759695
- Guy J**, Sachkova A, Moock M, Witte M, Wagener RJ, Staiger JF. 2017. Intracortical network effects preserve thalamocortical input efficacy in a cortex without layers. *Cerebral Cortex* 27:4851–4866. DOI: <https://doi.org/10.1093/cercor/bhw281>, PMID: 27620977
- Guy J**, Staiger JF. 2017. The functioning of a cortex without layers. *Frontiers in Neuroanatomy* 11:54. DOI: <https://doi.org/10.3389/fnana.2017.00054>, PMID: 28747874
- Hajos N**, Katona I, Naiem SS, MacKie K, Ledent C, Mody I, Freund TF. 2000. Cannabinoids inhibit hippocampal GABAergic transmission and network oscillations. *European Journal of Neuroscience* 12:3239–3249. DOI: <https://doi.org/10.1046/j.1460-9568.2000.00217.x>, PMID: 10998107
- Harris KD**, Shepherd GM. 2015. The neocortical circuit: themes and variations. *Nature Neuroscience* 18:170–181. DOI: <https://doi.org/10.1038/nn.3917>, PMID: 25622573
- Heft S**, Jonas P. 2005. Asynchronous GABA release generates long-lasting inhibition at a Hippocampal interneuron-principal neuron synapse. *Nature* 437:1319–1328. DOI: <https://doi.org/10.1038/nn1542>
- Hirotsune S**, Fleck MW, Gambello MJ, Bix GJ, Chen A, Clark GD, Ledbetter DH, McBain CJ, Wynshaw-Boris A. 1998. Graded reduction of Pafah1b1 (Lis1) activity results in neuronal

- migration defects and early embryonic lethality. *Nature Genetics* 19:333–339. DOI: <https://doi.org/10.1038/1221>, PMID: 9697693
- Hunt** RF, Dinday MT, Hindle-Katel W, Baraban SC. 2012. LIS1 deficiency promotes dysfunctional synaptic integration of granule cells generated in the developing and adult dentate gyrus. *Journal of Neuroscience* 32: 12862–12875. DOI: <https://doi.org/10.1523/JNEUROSCI.1286-12.2012>, PMID: 22973010
- Kato** M. 2003. Lissencephaly and the molecular basis of neuronal migration. *Human Molecular Genetics* 12:89R–96. DOI: <https://doi.org/10.1093/hmg/ddg086>
- Lee** SH, Foldy C, Soltesz I. 2010. Distinct endocannabinoid control of GABA release at Perisomatic and dendritic synapses in the Hippocampus. *Journal of Neuroscience* 30:7993–8000. DOI: <https://doi.org/10.1523/JNEUROSCI.6238-09.2010>, PMID: 20534847
- Lee** SH, Marchionni I, Bezair M, Varga C, Danielson N, Lovett-Barron M, Losonczy A, Soltesz I. 2014. Parvalbumin-positive basket cells differentiate among hippocampal pyramidal cells. *Neuron* 82:1129–1144. DOI: <https://doi.org/10.1016/j.neuron.2014.03.034>, PMID: 24836505
- Li** Y, Xu J, Liu Y, Zhu J, Liu N, Zeng W, Huang N, Rasch MJ, Jiang H, Gu X, Li X, Luo M, Li C, Teng J, Chen J, Zeng S, Lin L, Zhang X. 2017. A distinct entorhinal cortex to hippocampal CA1 direct circuit for olfactory associative learning. *Nature Neuroscience* 20:559–570. DOI: <https://doi.org/10.1038/nn.4517>, PMID: 28263300
- Margeta** MA, Shen K. 2010. Molecular mechanisms of synaptic specificity. *Molecular and Cellular Neuroscience* 43:261–267. DOI: <https://doi.org/10.1016/j.mcn.2009.11.009>, PMID: 19969086
- McManus** MF, Nasrallah IM, Pancoast MM, Wynshaw-Boris A, Golden JA. 2004. Lis1 is necessary for normal non-radial migration of inhibitory interneurons. *The American Journal of Pathology* 165:775–784. DOI: [https://doi.org/10.1016/S0002-9440\(10\)63340-8](https://doi.org/10.1016/S0002-9440(10)63340-8), PMID: 15331402
- Molnar** Z, Garel S, Lo´pez-Bendito G, Maness P, Price DJ. 2012. Mechanisms controlling the guidance of thalamocortical axons through the embryonic forebrain. *European Journal of Neuroscience* 35:1573–1585. DOI: <https://doi.org/10.1111/j.1460-9568.2012.08119.x>, PMID: 22607003
- Morozov** YM, Freund TF. 2003. Post-natal development of type 1 cannabinoid receptor immunoreactivity in the rat Hippocampus. *European Journal of Neuroscience* 18:1213–1222. DOI: <https://doi.org/10.1046/j.1460-9568.2003.02852.x>, PMID: 12956720
- Neu** A, Foldy C, Soltesz I. 2007. Postsynaptic origin of CB1-dependent tonic inhibition of GABA release at cholecystokinin-positive basket cell to pyramidal cell synapses in the CA1 region of the rat Hippocampus. *The Journal of Physiology* 578:233–247. DOI: <https://doi.org/10.1113/jphysiol.2006.115691>, PMID: 17053036
- Nielsen** JV, Blom JB, Noraberg J, Jensen NA. 2010. Zbtb20-induced CA1 pyramidal neuron development and area enlargement in the cerebral midline cortex of mice. *Cerebral Cortex* 20:1904–1914. DOI: <https://doi.org/10.1093/cercor/bhp261>, PMID: 19955470
- Polleux** F, Dehay C, Kennedy H. 1998. Neurogenesis and commitment of corticospinal neurons in reeler. *The Journal of Neuroscience* 18:9910–9923. PMID: 9822747
- Rice** ME, Galang RR, Roth NM, Ellington SR, Moore CA, Valencia-Prado M, Ellis EM, Tufa AJ,

- Taulung LA, Alfred JM, Pe´ rez-Padilla J, Delgado-Lo´ pez CA, Zaki SR, Reagan-Steiner S, Bhatnagar J, Nahabedian JF, Reynolds MR, Yeargin-Allsopp M, Viens LJ, Olson SM, et al. 2018. Vital signs: zika-associated birth defects and neurodevelopmental abnormalities possibly associated with congenital zika virus infection - U.S. territories and freely associated states, 2018. *MMWR. Morbidity and Mortality Weekly Report* 67:858–867. DOI: <https://doi.org/10.15585/mmwr.mm6731e1>, PMID: 30091967
- Salinger** WL, Ladrow P, Wheeler C. 2003. Behavioral phenotype of the Reeler mutant mouse: effects of RELN gene dosage and social isolation. *Behavioral Neuroscience* 117:1257–1275. DOI: <https://doi.org/10.1037/0735-7044.117.6.1257>, PMID: 14674845
- Slomianka** L, Amrein I, Knuesel I, Sørensen JC, Wolfer DP. 2011. Hippocampal pyramidal cells: the reemergence of cortical lamination. *Brain Structure and Function* 216:301–317. DOI: <https://doi.org/10.1007/s00429-011-0322-0>, PMID: 21597968
- Soltesz** I, Descheˆ nes M. 1993. Low- and high-frequency membrane potential oscillations during theta activity in CA1 and CA3 pyramidal neurons of the rat Hippocampus under ketamine-xylazine anesthesia. *Journal of Neurophysiology* 70:97–116. DOI: <https://doi.org/10.1152/jn.1993.70.1.97>, PMID: 8395591
- Soltesz** I, Losonczy A. 2018. CA1 pyramidal cell diversity enabling parallel information processing in the Hippocampus. *Nature Neuroscience* 21:484–493. DOI: <https://doi.org/10.1038/s41593-018-0118-0>, PMID: 295 93317
- Stanfield** BB, Cowan WM. 1979. The morphology of the Hippocampus and dentate gyrus in normal and reeler mice. *The Journal of Comparative Neurology* 185:393–422. DOI: <https://doi.org/10.1002/cne.901850302>, PMID: 438366
- Sur** M, Rubenstein JL. 2005. Patterning and plasticity of the cerebral cortex. *Science* 310:805–810. DOI: <https://doi.org/10.1126/science.1112070>, PMID: 16272112
- Tricoire** L, Pelkey KA, Erkkila BE, Jeffries BW, Yuan X, McBain CJ. 2011. A blueprint for the spatiotemporal origins of mouse hippocampal interneuron diversity. *Journal of Neuroscience* 31:10948–10970. DOI: <https://doi.org/10.1523/JNEUROSCI.0323-11.2011>, PMID: 21795545
- Valero** M, Cid E, Averkin RG, Aguilar J, Sanchez-Aguilera A, Viney TJ, Gomez-Dominguez D, Bellistri E, de la Prida LM. 2015. Determinants of different deep and superficial CA1 pyramidal cell dynamics during sharp-wave ripples. *Nature Neuroscience* 18:1281–1290. DOI: <https://doi.org/10.1038/nn.4074>, PMID: 26214372
- Valero** M, de la Prida LM. 2018. The Hippocampus in depth: a sublayer-specific perspective of entorhinal-hippocampal function. *Current Opinion in Neurobiology* 52:107–114. DOI: <https://doi.org/10.1016/j.conb.2018.04.013>, PMID: 29729527
- Varga** C, Lee SY, Soltesz I. 2010. Target-selective GABAergic control of entorhinal cortex output. *Nature Neuroscience* 13:822–824. DOI: <https://doi.org/10.1038/nn.2570>, PMID: 20512133
- Wagener** RJ, David C, Zhao S, Haas CA, Staiger JF. 2010. The somatosensory cortex of Reeler mutant mice shows absent layering but intact formation and behavioral activation of columnar somatotopic maps. *Journal of Neuroscience* 30:15700–15709. DOI: <https://doi.org/10.1523/JNEUROSCI.3707-10.2010>, PMID: 21084626
- Wagener** RJ, Witte M, Guy J, Mingo-Moreno N, Ku¨ gler S, Staiger JF. 2016. Thalamocortical

connections drive intracortical activation of functional columns in the mislaminated reeler somatosensory cortex. *Cerebral Cortex* 26:820–837.

DOI:<https://doi.org/10.1093/cercor/bhv257>, PMID: 26564256

Wynshaw-Boris A. 2007. Lissencephaly and LIS1: insights into the molecular mechanisms of neuronal migration and development. *Clinical Genetics* 72:296–304.

DOI:<https://doi.org/10.1111/j.1399-0004.2007.00888.x>, PMID: 17850624

Chapter 3.

Emergence of Non-Canonical Parvalbumin-Containing Interneurons in Hippocampus of a Murine Model of Type I Lissencephaly

***Note:** This chapter is from a manuscript under review at eLife:

Tyler G. Ekins, Vivek Mahadevan, Yajun Zhang, James A. D'Amour, Timothy Petros, and Chris J. McBain (2020). Emergence of Non-Canonical Parvalbumin-Containing Interneurons in Hippocampus of a Murine Model of Type I Lissencephaly.

Details of T. Ekins contributions:

With the exception of the snRNA-seq (I thank Dr. Vivek Mahadevan and the Petros Lab), I performed all experiments, analyzed data, created figures and wrote the manuscript (edited by Chris McBain).

ABSTRACT

Type I lissencephaly is a neuronal migration disorder caused by haploinsufficiency of the *LIS1* gene and is characterized in humans by agyria, mislamination of brain structures, developmental delays, and epilepsy. Here, we investigate the impact of *LIS1* mutation on the cellular migration, morphophysiology, microcircuitry and transcriptomics of mouse hippocampal CA1 parvalbumin-containing inhibitory interneurons (PV+INTs). We find that WT PV+INTs consist of two physiological subtypes (80% fast-spiking (FS), 20% non-fast-spiking (NFS)) and four morphological subtypes (basket, axo-axonic, bistratified, radiatum-targeting). We also discover that cell-

autonomous mutations within interneurons disrupts morphological development of PV+INTs and results in the emergence of a non-canonical “intermediate spiking (IS)” subset of PV+INTs. In the GlobalLis mutant, IS/NFS cells become the dominant PV+INT subtypes (56%) and the percentage of FS cells shrinks to 44%. We also find that IS/NFS cells are prone to entering depolarizing block, causing them to temporarily lose the ability to initiate action potentials and control network excitation, potentially promoting seizures. Finally, single-cell nuclear RNAsequencing of PV+INTs revealed several misregulated genes related to morphogenesis, cellular excitability, and synapse formation.

INTRODUCTION

Excitation in neocortical and hippocampal circuits is balanced by a relatively small (10-15%) yet highly heterogenous population of GABAergic inhibitory interneurons (Pelkey et al., 2017). During embryogenesis inhibitory interneurons are generated in the ganglionic eminences, then tangentially migrate to reach their cortical or hippocampal destination (Bartolini et al., 2013). Upon reaching the cortex or hippocampus, interneurons migrate along radial glial cells to their final laminar position and integrate into developing circuits (Lim et al., 2018). The process of neuronal migration requires molecular interactions of motor proteins with networks of microtubules; therefore, genetic mutations disrupting such proteins compromise neuronal migration and promote abnormal brain development (Wynshaw-Boris and Gambello, 2001; Corbo et al., 2002; Tissir and Goffinet, 2003).

LIS1 (PAFAH1B1) encodes a protein (Lis1) that regulates dynein microtubule binding and is essential for neuronal migration (Wynshaw-Boris and Gambello, 2001). Consequently, *LIS1*

haploinsufficiency results in classical, or Type I, lissencephaly (“smooth brain”), a rare neurodevelopmental disorder characterized in humans by brain malformation, intellectual disability, motor impairment, and drug-resistant epilepsy (Kato and Dobyns, 2003; Di Donato et al., 2017). Full loss of *LIS1* is embryonically lethal (Hirotsume et al., 1998).

Classical lissencephaly can be modeled in mouse lines generated through heterozygous removal of *LIS1*, which results in enlarged ventricles and disorganization of brain structures (Hirotsume et al., 1998). Structural abnormalities are particularly notable in the hippocampus, where the normally tightly compacted layer of pyramidal cells fractures into multiple bands of loosely organized cells (Fleck et al., 2000, D’Amour et al 2020). Mice heterozygous for *LIS1* share symptoms with human lissencephaly patients, including learning deficits, motor impairments, increased excitability and decreased seizure threshold (Paylor et al., 1999; Fleck et al., 2000; Greenwood et al., 2009; Menascu et al., 2013; Herbst et al., 2016). Due to the high density of recurrent excitatory connections and the reliance on inhibitory interneurons to control network excitability, the hippocampus and neocortex are prone to generating epileptic seizures (McCormick and Contreras, 2001). Thus, the increased propensity for seizures in *LIS1* mutants may be indicative of dysfunctional inhibition. Indeed, specific deficits in inhibitory interneuron wiring with pyramidal cell targets have been identified in *LIS1* mutant mice, but the origin of seizures remains unclear (Jones & Baraban, 2009; D’amour et al., 2020).

Inhibitory interneurons are classified based on a combination of their morphological, biochemical, intrinsic electrical, and connectivity properties (Lim et al., 2018). Advances in single-cell RNA sequencing have revealed enormous diversity in interneuron genomics, and current efforts attempt to correlate transcriptomic data sets with previously identified interneuron

subtypes (Tasic et al., 2018; Muñoz-Manchado et al., 2018; Gouwens et al., 2019; Que et al., 2020). In CA1 hippocampus alone, inhibitory synaptic transmission is mediated by at least 15 different subtypes of GABAergic inhibitory interneurons (Pelkey et al., 2017). Three canonical interneuron subtypes express the calcium-binding protein parvalbumin (PV): basket-cells, axo-axonic cells and bistratified cells. PV-containing inhibitory interneurons (PV+INTs) are often classified as “fast-spiking” cells due to their ability to sustain high-frequency discharges of action potentials with minimal spike-frequency adaptation/accommodation (Pelkey et al., 2017). Fast-spiking interneurons are essential for proper network oscillations and disrupting the function of PV+INTs can generate spontaneous recurrent seizures (Drexel et al., 2017; Panthi and Leitch, 2019). Recent transcriptomics suggests that there are several genomically distinct subpopulations of PV+INTs (Hodge et al., 2019; Gouwens et al., 2020), some of which may correspond to unique PV+INT subtypes that have remained largely understudied relative to the canonical FS subtypes listed above.

A current model for the formation of neural circuits posits that pyramidal cells (PCs) instruct radial migration and synaptic connectivity of INTs (Pelkey et al., 2017; Wester et al., 2019). In the cortex, INTs are initially dispersed throughout cortical layers, only sorting into their final positions between the 3rd and 7th postnatal day (Miyoshi & Fishell, 2010). Interneurons have programs that enable both cell type-specific and cellular compartment-specific targeting. For example, PV+INTs make connections with PCs and other PV+INTs, but rarely contact other subtypes of INTs (Kohus et al., 2016). Furthermore, different subtypes of PV+INTs target specific regions of PCs such as dendrites (bistratified cells), the axon initial segment (axo-axonic cells), or the perisomatic region (basket cells; Pelkey et al., 2017). Mutations to chemokine receptors can

alter this connectivity, and complete loss or reprogramming of cellular identity is possible when proteins are missing in development (Ye et al., 2015; Pelkey et al., 2017; Mahadevan et al., 2020).

Previous lissencephaly studies have demonstrated that migration of inhibitory interneurons is disrupted in *LIS1* heterozygous mutants (Fleck et al., 2000; McManus et al., 2004). In particular, PV+INTs adopt atypical positions in the hippocampus, including between heterotopic bands of pyramidal cells and within stratum radiatum, a layer where PV+INTs are rarely found in wildtype (WT) CA1 (Fleck et al., 2000; Jones and Baraban, 2009; D'Amour et al., 2020). Despite ectopic positioning of inhibitory interneurons and layer-specific reorganization of inhibitory inputs, the nature and consequences of PV+INT morphophysiological development and microcircuit organization following *LIS1* mutations have remained elusive.

Here we report the impact of *LIS1* mutations and resulting neuronal migration deficits on the lamination, morphology, intrinsic physiology, connectivity, synaptic transmission dynamics and genomics of hippocampal parvalbumin-containing inhibitory interneurons. Cell-autonomous loss of *LIS1* within interneurons results in the emergence of a novel physiological population of PV+INT, comprising ~50% of the total PV+INT cohort. Compared to canonical FS PV+INTs, these altered cells have lower firing rates, provide less reliable inhibition to pyramidal cells and have a higher propensity to enter depolarization block. Single-cell nuclear RNA sequencing (snRNA-seq) revealed multiple disruptions to the expression of ion channels regulating PV+INT excitability. We propose that disrupted physiological development and deficient inhibitory output of PV+INTs likely contributes to the spontaneous seizures observed in classical lissencephaly.

RESULTS AND DISCUSSION

Generation and characterization of *LIS1* mutant lines

To investigate the cell-autonomous and non-autonomous effects of *LIS1* heterozygous mutations on PV+INT migration and development, we crossed *LIS1*^{floxed1/+} breeders to three separate Cre lines: Sox2-Cre to generate heterozygous *LIS1* mutations in all cells (“GlobalLis”); Nkx2.1-Cre to generate heterozygous *LIS1* mutations specifically in medial ganglionic eminence-derived interneurons (“NkxLis”); and Emx1-Cre to generate heterozygous mutations specifically in pyramidal cells (“EmxLis”). These lines were further crossed to PV-TdTomato (TdT) reporter lines to enable selective targeting of PV+INTs during physiological recordings.

As previously reported (Hirotsune et al., 1998; Fleck et al., 2000; D’Amour et al., 2020) hippocampal lamination is disrupted in GlobalLis mice. The normally compact layer of pyramidal cells (PCs) (stratum pyramidale; s.p.) fractures into heterotopic bands, typically with a normotopic layer resembling the WT band, and an ectopic layer often fragmented into stratum oriens (s.o.; Figure 1A). This general pattern of disrupted hippocampal lamination is also observed in the EmxLis mouse line, but not in the NkxLis mouse, indicating that *LIS1* expression in pyramidal cells, but not MGE-derived interneurons, is essential for proper hippocampal pyramidal cell layer formation (Figure 1A).

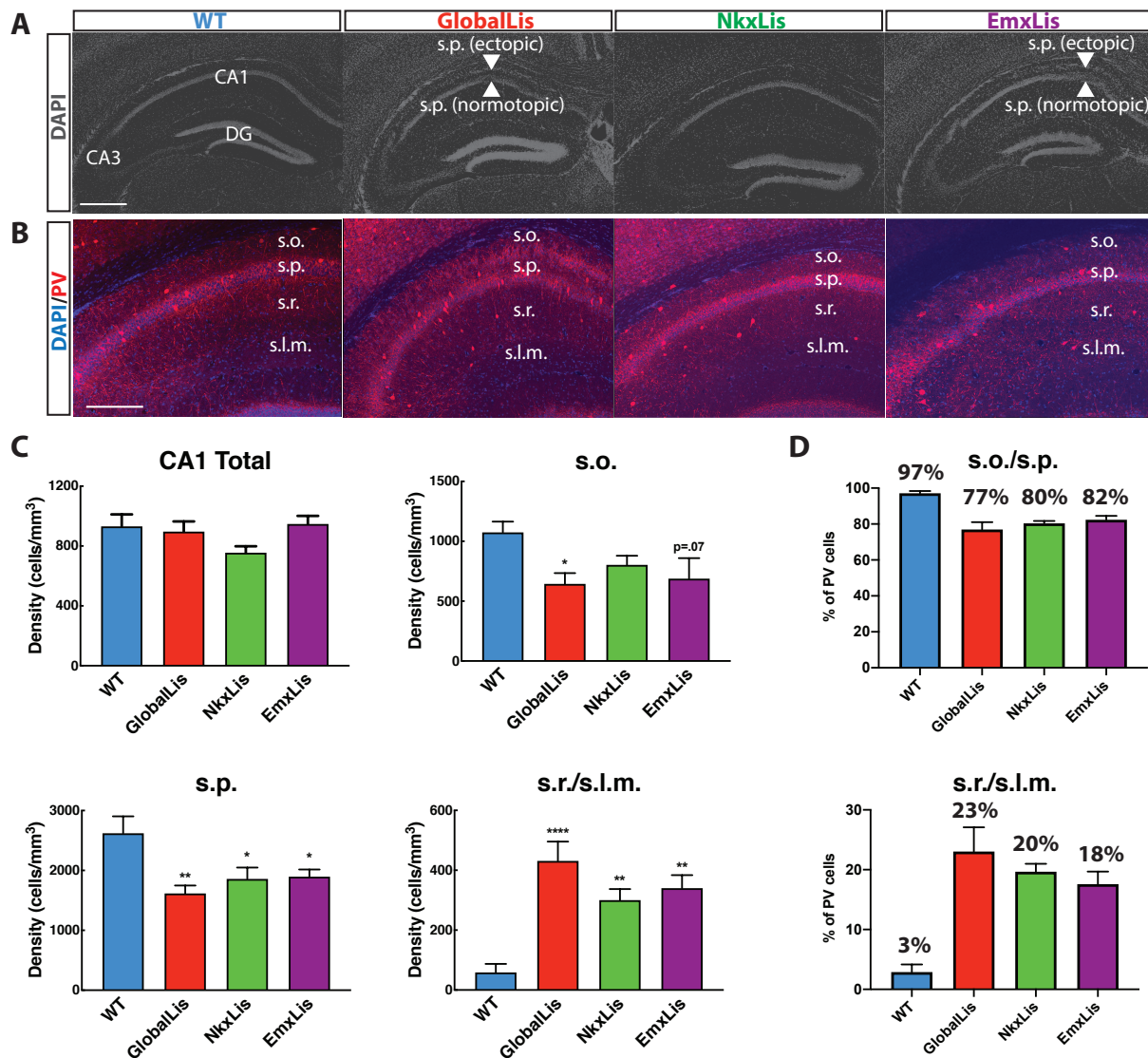
Figure 1

Figure 1. Cell-autonomous and non-autonomous effects of *LIS1* heterozygous loss on radial migration of PV+INTs. **A** DAPI-stained hippocampus of WT, GlobalLis (global mutation), NkxLis (IN-specific mutation), and EmxLis (PC-specific mutation) mice. **B** Images of PV-immunostaining in WT, GlobalLis, NkxLis, and EmxLis CA1. **C** Quantified densities of PV+INTs in CA1 and each sublayer. Counting was performed on four hippocampal sections from each animal ($n = 5$ animals per genotype). For statistical analysis * $p < 0.05$, ** $p < 0.01$, *** $p < 0.001$, **** $p < 0.0001$. **D** Percentage of PV+INTs in deep (s.o./s.p.) or superficial (s.r./s.l.m.) layers. Scale bar A = 600 μm , scale bar B = 200 μm .

Radial migration of inhibitory interneurons is disrupted in *LIS1* mutants

Previous studies have demonstrated severe cellular disorganization in rodent models of lissencephaly, including impaired of parvalbumin-containing inhibitory interneurons (PV+INTs; Fleck et al., 2000; Jones and Baraban, 2009; D'Amour et al., 2020). To investigate the nature of the aberrant migration of PV+INTs we first quantified their relative densities using immunohistochemistry. GlobalLis mutants exhibited no overall change in PV density in the CA1 subfield. However, as we reported previously (D'Amour et al 2020) PV+INT density was reduced in both s.o. and s.p. and increased in stratum radiatum (s.r.) and stratum lacunosum-moleculare (s.l.m.; Figure 1B-C). In WT CA1, an overwhelming majority (>95%) of PV+INTs are found in s.o. and s.p., while less than 5% reside in s.r. or s.l.m., indicating a strong preference for PV+INTs to typically inhabit deeper regions of the hippocampus. In contrast, in GlobalLis 77% of PV+INTs were found in s.o./s.p, with the proportion of cells in s.r./s.l.m. expanded to 23% of the total PV population (Figure 1D).

We next used the NkxLis and EmxLis lines, where *LIS1* is eliminated only in MGE-derived interneurons and pyramidal neurons respectively, to assay the impact of cell-autonomous and non-autonomous mutations on PV+INT migration. Interestingly, both genotypes had similar patterns of PV+INT somatic distribution to that observed in the GlobalLis CA1. In these mutants there was a significantly decreased density of PV+INTs in s.o./s.p. and increased density in s.r./s.l.m., with ~80% of PV+INTs found in deep regions (s.o./s.p.) and ~20% found in superficial regions (s.r./s.l.m.; Figure 1B-D). Thus, proper migration and lamination of PV+INTs requires both Lis1-dependent cell-intrinsic mechanisms (as revealed by the disruption in NkxLis PV cells) and

non-cell-autonomous cues from pyramidal neurons (demonstrated by the disruption in Emx18 PV cells).

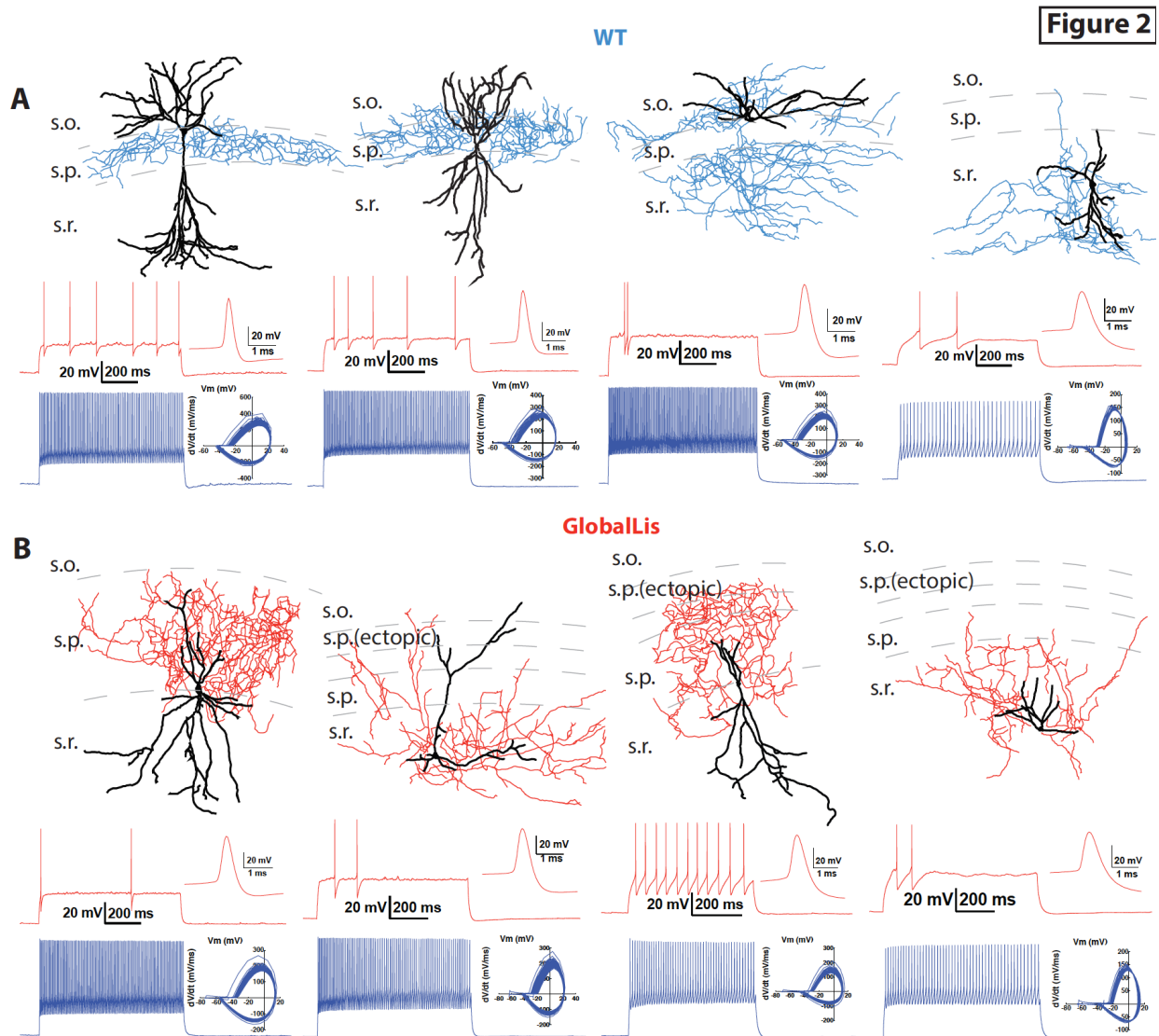


Figure 2. Morphological reconstructions and firing profiles of WT and GlobalLis PV+INTs. **A** Examples of WT PV+INTs with reconstructed cells on top (dendrite in black, axon in blue) and firing traces on bottom. Firing in response to threshold current is shown in red, with the first action potential shown expanded on the right. The blue trace displays firing at 2x threshold current and shows a phase plot on the right. Cell types from left to right: basket cell, axo-axonic cell, bistratified cell, radiatum-targeting cell. **B** Examples of GlobalLis PV+INTs. Dendrite is shown in black and axon in red. Cells can no longer be neatly parsed into the four morphological PV+INT subtypes found in WT CA1.

***LIS1* heterozygous mutation alters PV+INT morphophysiological development**

The vast majority of parvalbumin-containing inhibitory interneurons are classified as “fast-spiking” (FS) cells, due to their ability to sustain high-frequency discharges of action potentials (Pelkey et al., 2017). In cortical circuits, FS cells contribute to both feedforward and feedback inhibition and are essential in generating network oscillations; as such, disrupted FS cell function can lead to uncontrolled excitation and seizures (Hu et al., 2014).

To functionally characterize hippocampal PV+INTs we first examined the intrinsic electrophysiological properties of TdTomato+ (TdT) WT CA1 PV cells (Figure 2A). Accuracy of TdT labeling of PV+INTs was confirmed by quantifying the percentage of TdT and PV-immunostaining overlap: 92% of WT and 93% of Globalis hippocampal TdT+ cells were immunopositive for PV, and 97% of the immunopositive PV cells were labeled by TdT, enabling reliable targeting of PV+INTs (Figure 2—figure supplement 1).

WT fast-spiking PV+INTs have stereotypical intrinsic properties that include a low input resistance (75-90 M Ω), high rheobase (330-400 pA), high firing frequency at 2x (130-150 Hz) and 3x threshold (160-180 Hz), narrow action potential half-width (0.40-0.44 ms) and minimal spike-frequency-adaptation (0.75-0.85; Table 1). Surprisingly, we routinely observed an additional population (~15-20%) of WT TdT-labeled PV+INTs that did not possess stereotypical fast-spiking firing properties. This NFS subpopulation also displayed numerous intrinsic properties distinct from canonical FS cells, including a low firing frequency, high input resistance and low rheobase (i.e. Figure 2A top right). Clusters of atypical PV+INTs have been previously reported in subiculum

(“quasi fast-spiking interneurons”; Nassar et al., 2015) and striatum (“fast-spiking-like cells”; Munoz-Manchado et al., 2018).

To independently verify whether WT hippocampal PV+INTs could be functionally segregated into distinct clusters in an unbiased fashion we performed principal component analysis (PCA) using several key intrinsic physiological features (action potential half-width, firing frequency at 2x threshold, firing frequency at 3x threshold, adaptation ratio at 2x threshold, input resistance, rheobase, sag index). WT PV+INTs neatly parsed into two subtypes comprised of a large majority FS cohort, and a small minority atypical subset (Figure 3A-D). Due to their intrinsic physiological differences from FS cells and inability to sustain high frequencies of action potentials, for ease of discussion we designate this unique subpopulation of PV+INTs as “non-fast-spiking” (NFS) cells. PV+NFS cells have lower firing frequencies at 2x (55-75 Hz) and 3x (85-105 Hz) threshold, lower adaptation ratios (0.60-0.75) broader action potential half-widths (0.55-0.65 ms), larger input resistances (120-170 M Ω), and lower rheobases (120-180 pA) than standard PV+FS cells (Figure 3E; Table 1).

With respect to their morphology, hippocampal PV+INTs are routinely parsed into three primary subtypes based on axonal arborization: basket cells (BCs; which target cell pyramidal cell (PC) bodies and proximal dendrites), axo-axonic cells (AACs; which target PC axon initial segments), and bistratified cells (BiCs; which target PC apical and basal dendrites; Pelkey et al., 2017). Post-hoc anatomical recoveries of recorded cells regularly revealed these three standard morphologies, and additionally a unique hippocampal PV+INT, which we designate “radiatum-targeting cells” (RTC) as this subtype confines its axon to s.r. and is presumably a subtype of dendrite-targeting cell. Figure 2A shows typical morphologies and firing patterns at threshold

(with expanded action potentials; red) and at 2x threshold current injection (phase plots in blue) of WT CA1 PV+INTs (from left to right: BC, AAC, BiC, PV+RTC).

Hippocampal layers differ in their composition of PV+INT morphophysiological subtypes. In WT deeper regions (s.o./s.p.) are populated primarily by PV+FS cells (~90%), consisting of all of the morphological forms (BC, AAC, BiC, RTC). In contrast, all PV+NFS cells residing in s.o./s.p. had BC morphologies (Figure 3F-G). The small number of PV+FS and NFS cells found in superficial layers (s.r.) all had RTC morphology (Figure 3F-G). In summary, WT hippocampal CA1 PV+INTs consist of two physiological (FS and NFS) and four morphological subtypes (BC, AAC, BiC, RTC), and the overwhelming majority of PV+INTs are found in deep hippocampal layers, consistent with previous reports (Pelkey et al 2017).

Figure 3

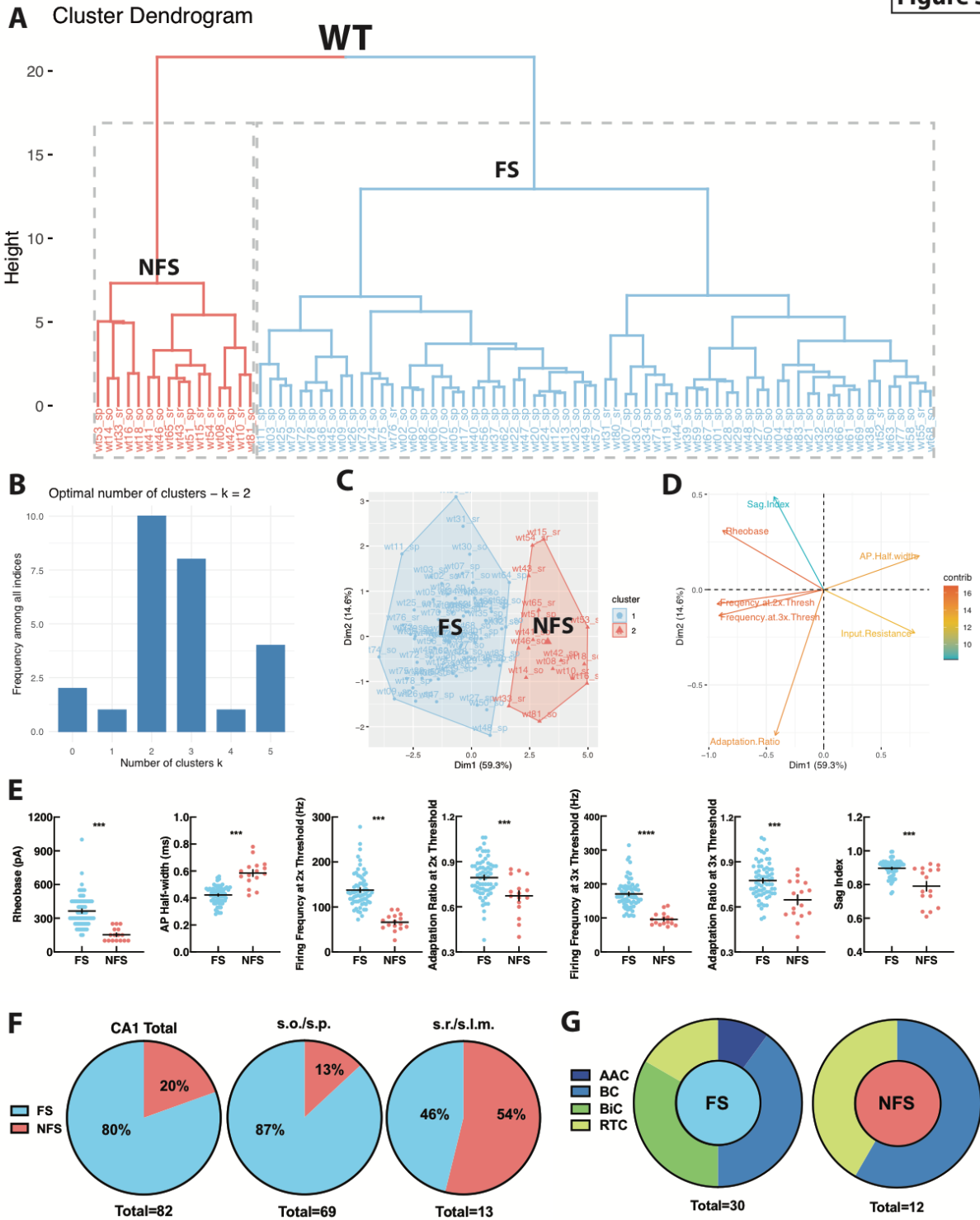


Figure 3. WT PV+INTs consist of two physiological subtypes: FS and NFS cells. **A** Unbiased cluster analysis dendrogram displays 83 PV+INTs sorted into two clusters that represent fast-spiking (FS) and non-fast-spiking (NFS) cells. **B** Indicates optimal detection of two clusters (FS and NFS). **C** Cluster plot of the same 83 PV+INTs. Nonoverlap indicates clear segregation of FS/NFS clusters. **D** Contributions of each intrinsic physiological property used in the

cluster analysis. **E** Plots displaying and FS/NFS cell intrinsic properties. For statistical analysis * $p < 0.05$, ** $p < 0.01$, *** $p < 0.001$, **** $p < 0.0001$. **F** Percentages of FS/NFS cells in CA1 and in each sublayer. **G** Distributions of FS and NFS cell morphological subtypes. FS cells consisted of BCs, AACs, BiCs, and RTCs, while all recovered NFS cells were identified as BCs or RTCs.

Using the same strategy, we next targeted PV+INTs in the GlobalLis mouse line and utilized PCA to cluster GlobalLis PV+INTs by their intrinsic physiological properties. Unlike WT PV+INTs, GlobalLis cells segregated into three clusters. (Figure 4A-D). In addition to the FS and NFS cell clusters, a third entirely new cluster of PV+INTs emerged (Figure 4A-D). GlobalLis FS cells had identical intrinsic properties as WT FS cells with the exception of shorter action potential half-widths (0.32-0.37 ms vs 0.41-0.44 ms; Table 1). GlobalLis NFS cells were indistinguishable from WT NFS cells. A number of intrinsic physiological properties of the third group of cells fell between those of FS and NFS cells, including firing frequency at 2x (90-110 Hz) and 3x threshold (120-140 Hz), adaptation ratio (0.65-0.85), AP half-width (0.45-0.50 ms) and input resistance (80-100 M Ω ; Figure 4E; Table 1). Consequently, we refer to this emergent physiological PV+INT subtype as “intermediate spiking” (IS) cells. Of particular interest 47% of all GlobalLis PV+INTs consisted of the IS subtype and only 44% consisted of FS cells (Figure 4F) compared the 80% observed in WT CA1 PV+INTs. Within CA1, superficial layers had proportionally more IS cells (~60%) than deeper layers (~25%; Figure 4F).

In addition to somatic misplacement and physiological disruption, the morphological development of GlobalLis PV+INTs is radically disrupted. Many cells did not resemble stereotypical morphologies of any WT PV+INT subtype (Figure 2A) and often had ectopic axonal branching that extended in all directions, rather than forming the tight plexus seen in WT. Other mutant PV+INTs took on combinations of hippocampal PV cell features including bistratified-like

cells with baskets, and radiatum-targeting cells with axons that also extended into the s.l.m. (Figure 2B).

Sholl analyses of digitally reconstructed axonal and dendritic arbors or recorded PV+INTs revealed that WT and GlobalLis FS cells and GlobalLis IS cells had larger and more complex axonal and dendritic trees than NFS cells of both genotypes (Figure 2—figure supplement 2A-D). The smaller axonal arbors of NFS cells (WT: 131 Sholl intersections, GlobalLis: 133 intersections) relative to FS (WT: 222 Sholl intersections, GlobalLis: 271 intersections) and IS cells (224 intersections) may imply lower synaptic connectivity of this subtype (Figure 2—figure supplement 2D ; Table 1). In conclusion, global mutations to *LIS1* disrupt morphophysiological identity in a large number of PV+INTs, however overall axonal and dendritic growth is not inhibited.

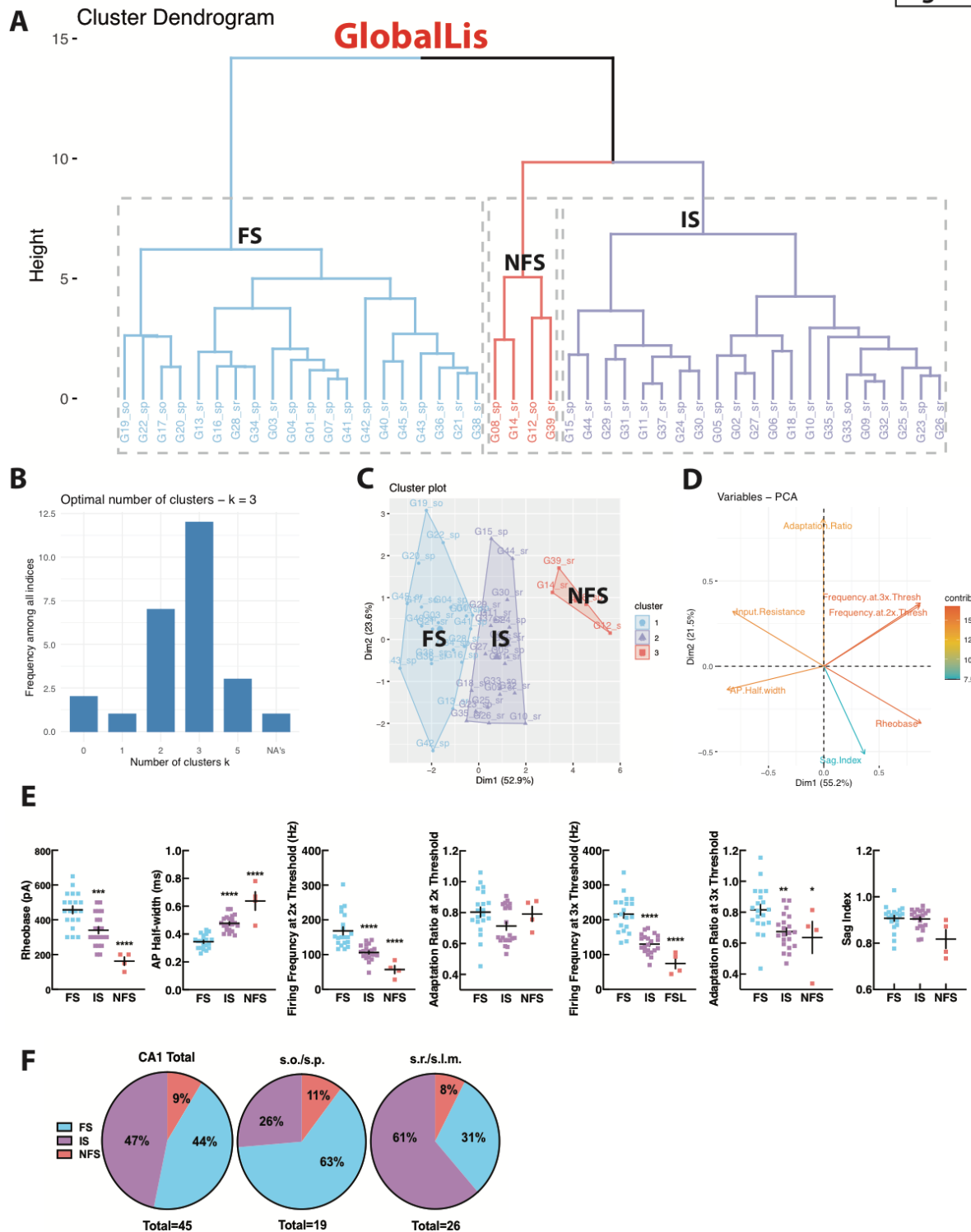


Figure 4. *GlobalLis* PV+INTs consist of three physiological subtypes: FS, IS and NFS cells. **A** Unbiased cluster analysis indicates emergence of an additional cluster in *GlobalLis* CA1, displayed in the dendrogram of 45 PV+INTs. **B** Indicates optimal detection of three clusters (FS, IS, NFS). **C** Cluster plot of the same 45 PV+INTs. **D** Contributions of each intrinsic physiological property used in the cluster analysis. **E** Plots displaying FS/IS/NFS cell intrinsic

properties. For statistical analysis * $p < 0.05$, ** $p < 0.01$, *** $p < 0.001$, **** $p < 0.0001$. F Percentage of FS/IS/NFS cells in CA1 and in each sublayer.

Cell-autonomous *LIS1* mutation within interneurons disrupts PV+INT development

We next recorded from PV+INTs in both the EmxLis and NkxLis mutants to determine if the disruption of PV+INT morphophysiological development emerges from interactions in a malformed hippocampus (EmxLis, Figure 1B-D) or from selective disruption of inhibitory interneuron intrinsic developmental programs (NkxLis, Figure 1B-D). PCA of intrinsic physiological properties of PV+INTs from the EmxLis hippocampus identified 2 clusters (corresponding to FS and NFS), consistent with WT (Figure 3—figure supplement 1A). To increase the power of the PCA and confirm accurate clustering, we combined and analyzed the WT and EmxLis datasets together. Combining WT and EmxLis cells resulted in identical clusters of FS and NFS cells, indicating the ease of identifying normally developed FS and NFS cell types (Figure 3—Figure supplement 1B). The total ratio of FS/NFS cells in CA1 as well as in each individual layer remains relatively unchanged in the EmxLis hippocampus (Figure 3—figure supplement 1C). Furthermore, morphological development of PV+INTs was relatively unaffected by non-autonomous *LIS1* mutation: PV+ cells developed into identifiable BCs, BiCs, AACs, and RTCs (Figure 3—figure supplement 1D). In conclusion, in EmxLis mutants PV+INTs develop into canonical morphophysiological subtypes despite disorganized pyramidal cell layers.

We next examined PV+INTs in the NkxLis (interneuron-specific mutation) hippocampus and used PCA to analyze the physiological properties. Similar to the GlobalLis mutant, we detected 3 clusters of PV+INTs, however clustering accuracy was not optimal (i.e. occasional IS cells were classified as NFS cells etc.; Figure 4—figure supplement 1A). To increase analytical

power and improve clustering accuracy, we combined the NkxLis and GlobalLis datasets and again found three clusters: FS, IS and NFS cells (Figure 4—figure supplement 1B). The novel IS cell subtype accounts for ~50 percent of total PV+INTs in both the NkxLis and GlobalLis genotypes, with more IS cells found in superficial hippocampal layers (Figure 4—figure supplement 1C). Thus, with cell-autonomous *LIS1* mutations within interneurons, the overall distribution of PV+INT physiological subtypes shifts away from the 80% FS, 20% NFS distribution in WT (and EmxLis) to 44% FS, 56% IS/NFS in the GlobalLis mutant and 29% FS, 71% IS/NFS in the NkxLis mutant. Despite the normal lamination of pyramidal cell layers in the NkxLis hippocampus, the morphology of NkxLis PV+INTs appear similar to the GlobalLis mutants; cells take on hybrid combinations of morphological features and distinguishing meaningful subtypes becomes nontrivial, if not impossible (Figure 4—figure supplement 1D).

Finally, we tested whether subtypes of PV+INTs (FS, IS, NFS) shared intrinsic physiological properties across genotypes. Similar to our observation of shorter action potential half-widths in GlobalLis FS cells, half-width was also shorter than WT in NkxLis (0.32-0.38 ms) and EmxLis (0.34-0.39 ms) genotypes (Table 1). All other intrinsic properties of PV+INT physiological subtypes were preserved across all genotypes (Figure 4—figure supplement 2; Table 1). Taken together, these results indicate that while both cell-autonomous and non-autonomous *LIS1* mutations can disrupt somatic positioning, only cell-autonomous mutations within interneurons perturb the morphophysiological identity of PV+INTs.

Table 1: Membrane, firing and morphological properties of PV+INTs	WT FS 67 cells	GlobalLis FS 20 cells	NkxLis FS 12 cells	EmxLis FS 30 cells	WT IS 0 cells	GlobalLis IS 21 cells	NkxLis IS 21 cells	EmxLis IS 0 cells	WT NFS 16 cells	GlobalLis NFS 4 cells	NkxLis NFS 8 cells	EmxLis NFS 8 cells
Input Resistance (M Ω)	82.5 \pm 3.6	63.5 \pm 4.2	61.1 \pm 6.3	75.0 \pm 4.7	n/a	88.5 \pm 4.9	85.5 \pm 7.0	n/a	143.1 \pm 11.9	132.0 \pm 14.4	200.7 \pm 17.0	173.2 \pm 9.0
Rheobase (pA)	364.2 \pm 17.3	457.5 \pm 22.2	533.3 \pm 42.3	463.3 \pm 24.8	n/a	340.5 \pm 20.0	342.9 \pm 21.1	n/a	153.1 \pm 14.8	162.5 \pm 20.0	125.0 \pm 13.4	143.8 \pm 11.3
Firing Freq 2x Threshold (Hz)	137.6 \pm 4.7	168.5 \pm 11.2	173.2 \pm 14.8	155.4 \pm 7.4	n/a	106.2 \pm 4.8	95.6 \pm 3.5	n/a	66.0 \pm 4.5	57.0 \pm 11.6	72.3 \pm 4.4	58.0 \pm 3.5
Adaptation Ratio 2x Threshold	0.79 \pm 0.02	0.80 \pm 0.03	0.72 \pm 0.04	0.71 \pm 0.02	n/a	0.71 \pm 0.03	0.65 \pm 0.03	n/a	0.67 \pm 0.03	0.79 \pm 0.05	0.79 \pm 0.06	0.52 \pm 0.05
Firing Freq 3x Threshold (Hz)	170.9 \pm 5.1	216.5 \pm 11.5	213.0 \pm 15.3	195.7 \pm 10.3	n/a	130.2 \pm 6.0	131.1 \pm 5.1	n/a	96.1 \pm 4.6	74.5 \pm 15.1	100.8 \pm 5.7	77.8 \pm 6.9
Adaptation Ratio 3x Threshold	0.78 \pm 0.01	0.82 \pm 0.03	0.71 \pm 0.05	0.71 \pm 0.02	n/a	0.67 \pm 0.02	0.57 \pm 0.03	n/a	0.65 \pm 0.03	0.64 \pm 0.10	0.73 \pm 0.05	0.47 \pm 0.05
AP Threshold (mV)	-39.9 \pm 0.7	-41.2 \pm 1.2	-39.9 \pm 1.3	-37.8 \pm 1.1	n/a	-40.4 \pm 1.1	-35.9 \pm 1.2	n/a	-40.6 \pm 1.2	-38.6 \pm 2.8	-36.8 \pm 1.2	-36.8 \pm 1.3
AP Half-width (ms)	0.42 \pm 0.01	0.34 \pm 0.01	0.35 \pm 0.01	0.36 \pm 0.01	n/a	0.48 \pm 0.01	0.44 \pm 0.01	n/a	0.59 \pm 0.02	0.64 \pm 0.07	0.56 \pm 0.04	0.58 \pm 0.04
AP Amplitude (mV)	61.1 \pm 1.0	61.2 \pm 2.7	55.8 \pm 3.0	57.5 \pm 2.0	n/a	62.1 \pm 2.3	53.6 \pm 2.0	n/a	65.4 \pm 3.2	64.8 \pm 7.0	55.1 \pm 5.7	64.9 \pm 4.8
AP Max Rise Slope (mV/ms)	259.9 \pm 5.2	248.3 \pm 13.5	268.6 \pm 11.7	217.0 \pm 12.1	n/a	261.4 \pm 10.7	231.0 \pm 10.3	n/a	228.6 \pm 11.5	210.3 \pm 25.0	197.9 \pm 18.3	241.0 \pm 26.0
AP Max Decay Slope (mV/ms)	-188.7 \pm 5.5	-176.0 \pm 14.3	-201.6 \pm 9.1	-211.4 \pm 12.6	n/a	-198.1 \pm 12.6	-149.2 \pm 7.1	n/a	-136.5 \pm 11.5	-131.3 \pm 20.6	-119.2 \pm 14.7	-125.4 \pm 16.8
AHP Amplitude (mV)	-16.8 \pm 0.6	-17.5 \pm 0.9	-15.3 \pm 0.9	-16.7 \pm 0.7	n/a	-16.3 \pm 0.8	-16.0 \pm 1.0	n/a	-15.7 \pm 1.2	-16.9 \pm 1.1	-17.0 \pm 1.2	-11.3 \pm 1.7
Membrane Time Constant (ms)	8.5 \pm 0.5	7.5 \pm 0.4	6.7 \pm 0.4	8.6 \pm 0.4	n/a	8.7 \pm 0.4	8.5 \pm 0.7	n/a	10.9 \pm 0.6	12.9 \pm 0.6	14.8 \pm 1.6	17.1 \pm 1.0
Membrane Capacitance (pF)	104.4 \pm 5.0	117.7 \pm 6.6	116.8 \pm 18.6	123.9 \pm 7.7	n/a	103.7 \pm 8.6	105.7 \pm 8.3	n/a	91.3 \pm 6.4	88.6 \pm 6.4	73.8 \pm 4.8	97.0 \pm 4.3
Sag Index	0.90 \pm 0.01	0.91 \pm 0.01	0.95 \pm 0.01	0.92 \pm 0.01	n/a	0.90 \pm 0.01	0.91 \pm 0.01	n/a	0.8 \pm 0.03	0.82 \pm 0.04	0.86 \pm 0.02	0.85 \pm 0.02
Total Sholl Intersections (Dendrite)	48 \pm 7 (19 cells)	65 \pm 6 (6 cells)	43 \pm 8 (8 cells)	56 \pm 7 (11 cells)	n/a	43 \pm 7 (7 cells)	61 \pm 11 (8 cells)	n/a	26 \pm 4 (10 cells)	28 \pm 8 (2 cells)	34 \pm 11 (3 cells)	38 \pm 10 (4 cells)
Total Sholl Intersections (Axon)	222 \pm 22	271 \pm 44	206 \pm 44	324 \pm 51	n/a	224 \pm 56	224 \pm 41	n/a	131 \pm 15	133 \pm 3	97 \pm 21	95 \pm 26

PV+INT microcircuit rearrangements in the GlobalLis hippocampus

We next investigated the impact of *LIS1* haploinsufficiency on microcircuit formation by examining unitary inhibitory post synaptic currents (uIPSCs) using dual whole-cell recordings between synaptically coupled pairs of PV+INTs and CA1 pyramidal cells (Figure 5A-B).

In general, the connection probability of WT FS cells onto PCs was higher than that observed between NFS cells and PCs (32% vs 14% connected). Connectivity rates of GlobalLis FS cells (27%; 11/41 cells) were similar to WT FS cells. IS cells had a 27% connection probability (8/30 cells) onto PCs and 0/3 NFS cells were connected to PCs (Figure 5C).

WT FSBCs connected to PCs with high potency synapses (170 \pm 75 pA) which had an extremely high neurotransmitter release probability (0.99 \pm 0.01) and quick latency to release (1.2 \pm 0.1 ms). Compared to FSBCs, WT FSBC-PC connections had weaker synapses (25 \pm 5 pA), slightly lower release probability (0.89 \pm 0.05) and a nearly identical latency (1.1 \pm 0.1 ms), while NFSBCs also had weaker connections (50 \pm 15 pA), they also had lower release probability (0.83 \pm 0.12) but longer transmission latency (2.4 \pm 0.3 ms). In the GlobalLis mutant, FS-PC

connections were weaker (70 ± 15 pA) than WT FSBCs, but not significantly different when we pooled the datasets of WT FSBC and FSBiC-PC connections (110 ± 45 pA). GlobalLis FS cell release probability (0.97 ± 0.02) and latency (0.9 ± 0.1 ms) were indistinguishable from WT FS cells. Similar to NFS cells, IS cells had lower release probability (0.83 ± 0.06) and longer latency (1.7 ± 0.2 ms), contrasting FS-PC connections (Figure 5D; Table 2). Unfortunately, no GlobalLis NFS-PC connections were obtained.

We next investigated short-term transmission dynamics using high-frequency trains of presynaptic action potentials (Figure 5B). All PV-PC pairs showed characteristic synchronous neurotransmitter release and marked synaptic depression across a 50 Hz, 25 pulse train. In WT FSBCs, by the end of the train, uIPSC amplitude at the end of the 50 Hz train was reduced by 70% and the failure rate increased to 29%. Transmission at WT FSBiC connections fell by 61% and possessed a higher failure rate (58%). Unitary connections at WT NFS cells fell to 82% of the first pulse and the failure rate was 73%. In the GlobalLis mutant, FS-PC connection strength dropped by 70% and the failure rate increased to 32% by the end of the train; values close to those seen in WT FS cells. Similarly, GlobalLis IS connections dropped by 71% but the failure rate increased to 62%, similar to NFS cells (Figure 5E). Collectively, these results confirm that at the monosynaptic level, both the unitary synaptic amplitudes and the short-term dynamics of transmission are unchanged in GlobalLis FS-PC connections, however IS-PC synapses resemble those of NFS cells.

Figure 5

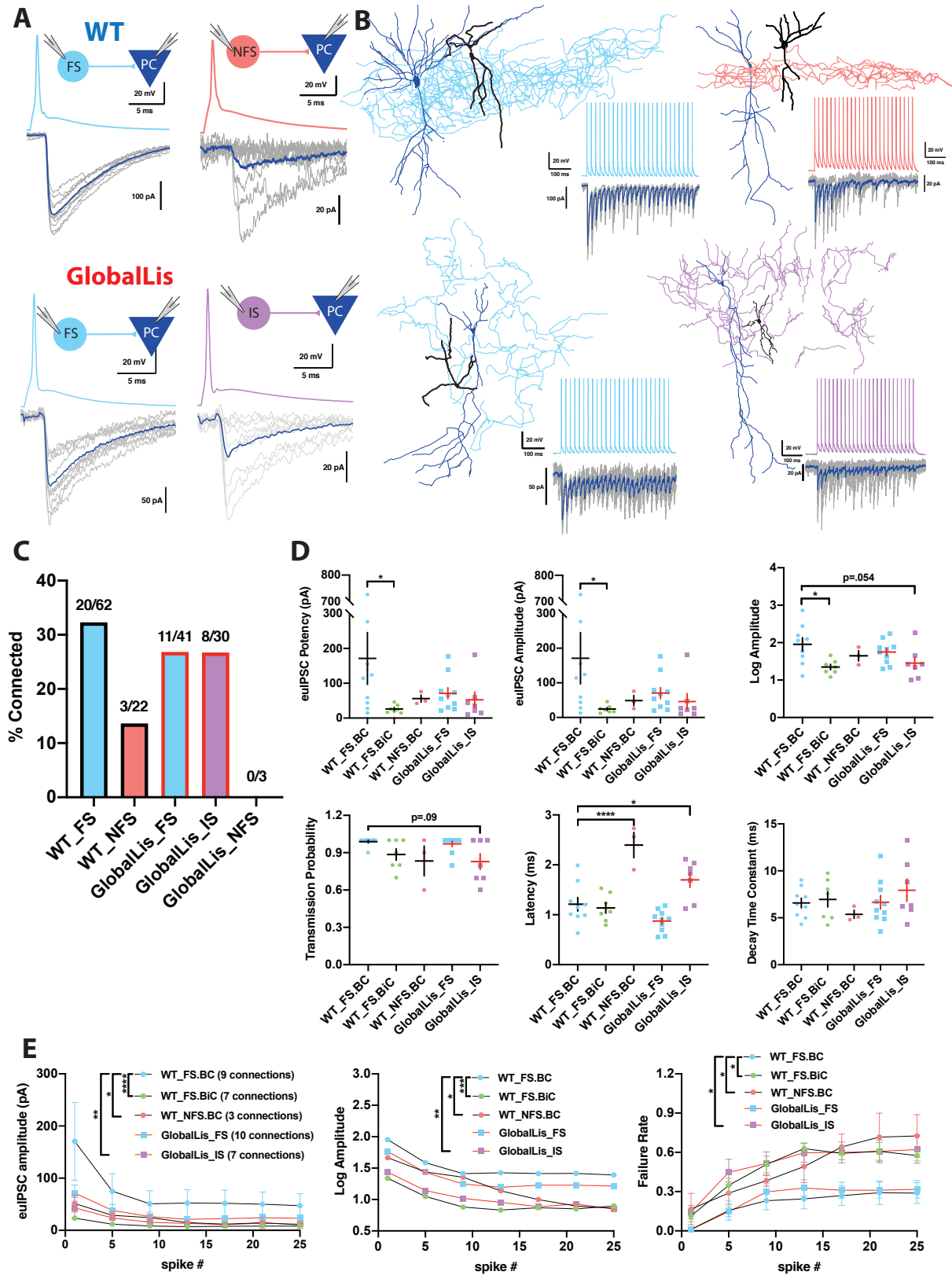


Figure 5. Connectivity and microcircuitry PV+INTs. **Ai** Examples of paired whole-cell recordings between synaptically connected presynaptic PV+INTs (top traces) and postsynaptic CA1 PCs (bottom traces). 10 individual traces (grey) and an averaged trace (navy) are shown for the postsynaptic cells. Note that a high [Cl⁻] internal solution was used in the PCs, resulting in GABAergic inward currents when PCs were clamped at -70 mV. **B** Reconstructions of PV+INTs (dendrite/cell body in black, axon in light blue, pink or purple) and PCs (dendrite/cell body in navy) and sample traces of a 50 Hz, 25 pulse stimulation. **C** Connectivity of PV+INT to PCs. Note the lower connectivity of NFS cells. **D** Unitary transmission properties between PV+INTs and PCs. **E** Short-term plasticity of PV+INT microcircuits during a 50 Hz, 25 pulse train. For statistical analysis *p<0.05, **p<0.01, ***p<0.001, ****p<0.0001.

Table 2: Unitary transmission properties by PV+INT subtype	WT FS.BC 9 connections	WT FS.DTC 7 connections	WT NFS.BC 3 connections	GlobalLis FS 10 connections	GlobalLis IS 7 connections
eulPSC Potency (pA)	171±74	26±5	56±10	71±16	56±20
eulPSC Amplitude (pA)	171±74	24±4	49±15	66±15	48±20
Transmission Probability	0.99±0.01	0.89±0.05	0.83±0.12	0.97±0.02	0.83±0.05
Latency (ms)	1.2±0.1	1.1±0.1	2.4±0.3	0.9±0.1	1.6±0.1
Decay Time Constant (ms)	6.6±0.5	7.0±0.8	5.4±0.4	6.5±0.7	7.7±1.1

Depolarization block of action potential firing is a common feature of IS/NFS but not FS cells

PV+INTs are critical regulators of network excitability, such that their rapid action potential and transmission kinetics act to generate both feedforward and feedback inhibition and local oscillations, as well as preventing cortical network activity from disintegrating into electrographic events that are the underpinnings of seizure activity. Recent evidence suggests that in epileptic human patients, PV+INT function becomes compromised, and overactivation of PV+INTs can drive action potentials into depolarization block, causing a temporary loss of their action potential initiation, consequently resulting in a net decrease in inhibitory tone, and precipitation of seizure propagation (Ahmed et al., 2014; Sudhakar et al., 2019)

We were struck by our observation that the majority of PV+INTs in the GlobalLis mouse are IS/NFS cells (56%) compared to FS, which represent only 44% of the total PV+INT population (cf. 80% in WT). Both IS and NFS cells possess lower maximal firing frequencies and longer

duration action potentials compared to FS cells. This relative shift in the overall PV+ cell population and their network dynamics may compromise PV+INT network control over network excitability in the *LIS1* mutant and promote lower seizure thresholds observed in previous studies (Fleck et al., 2000).

FS PV+INTs are endowed with both voltage-gated Na⁺ and K⁺ channels that enable rapid action potential repolarization and conductance deinactivation, permitting repetitive high frequency firing with little firing accommodation and a resistance to depolarizing block (Rudy & McBain, 2001; and Hu et al., 2014; Pelkey et al., 2017). However, it is unclear whether either NFS or IS PV+INTs share the same resistance to firing accommodation or depolarization block of AP firing during sustained excitation.

Depolarization block susceptibility of WT and GlobalLis PV+INTs was first assayed by injecting PV+INTs with increasing suprathreshold currents (500 ms duration; Figure 6A). Due to their low input resistance, FS cells in both WT and GlobalLis can sustain large current injections before action potentials enter into a depolarization block, with the vast majority of cells (70-77%) fully retaining the ability to fire at high frequencies (>250Hz) even after a maximal current injection of 1500 pA (Figure 6B). In contrast, 100% of NFS in both WT and GlobalLis mice and 92% of GlobalLis IS cells were driven into depolarizing block, and required less current to do so (respectively 690±110 pA, 700±200 pA, 990±80 pA) than the 23-30% of FS cells that we did observe to enter depolarizing block (WT: 1230±180 pA, GlobalLis: 1280±110 pA; Figure 6B).

In our previous study (Fleck et al., 2000), we demonstrated that the CA1 hippocampus in *LIS1* mutant mice had a lowered threshold for electrographic events in the 8.5mM K⁺ mouse model of epilepsy (Traynelis & Dingledine, 1988). In this model a modest 5mM elevation of

extracellular K^+ promotes cellular depolarization coupled to a change in the E_K of +23mV. Previously we did not explore the cellular underpinnings for this change in seizure threshold but now consider that the change in extracellular K^+ may drive the expanded noncanonical PV+INT network into a more depolarized state that reduces their propensity for sustained action potential activity. Therefore, we revisited this mouse model of epilepsy to determine whether either hippocampal pyramidal cells or PV+INTs enter depolarization block under conditions of elevated extracellular K known to drive electrographic activity.

We recorded evoked and spontaneous action potentials in WT and GlobalLis PV+INTs and pyramidal neurons during a 15-minute exposure period to elevated extracellular $[K^+]$ (8.5 mM; Figure 6C). We found that no recorded WT FS cells (0/10) and only 1/7 GlobalLis FS cells (14%) lost the ability to sustain repetitive action potential firing in the face of elevated $[K^+]$. In contrast, 25% of IS cells (2/8), and 33% of both WT (1/3) and GlobalLis NFS cells (1/3) entered depolarization block following exposure to elevated $[K^+]$. No WT (0/5) or GlobalLis (0/4) hippocampal pyramidal neurons lost the capability to repetitively fire action potentials in 8.5 mM $[K^+]$ (Figure 6D). Taken together, these data demonstrate that relative to FS cells, IS and NFS PV+INTs have a strong propensity to enter depolarization block in response to elevated $[K^+]$ and suprathreshold depolarizing current injection.

Figure 6

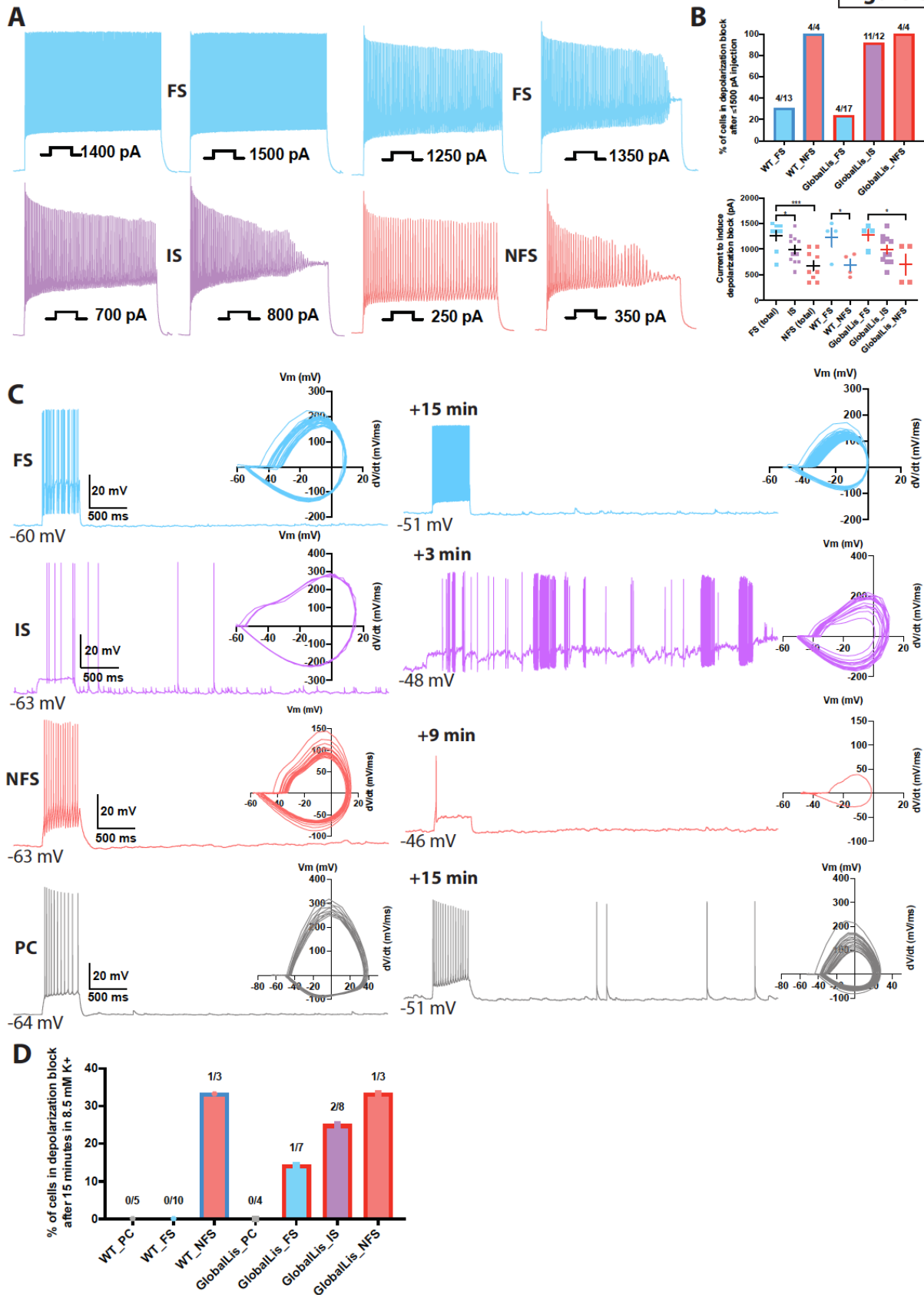


Figure 6. Depolarization block in PV+INTs. **A** Maximum firing frequencies and depolarizing block in subtypes of PV+INTs. Top left shows FS cell which showed no reduction in firing frequency after current injection of 1500 pA. Top right displays FS cell, bottom left displays IS cell, and bottom right displays NFS cell, all of which blocked. **B** Percentages of PV+INT subtypes that went into depolarization block with current injection of 1500 pA or less. For statistical analysis * $p < 0.05$, ** $p < 0.01$, *** $p < 0.001$. **C** Traces of PV+INTs in 3.5 mM extracellular [K⁺] (left) and after 8.5 mM extracellular [K⁺] (right) with inset phase plots. The IS cell example (second from top) shows the cell transitioning into depolarizing block and losing the ability to initiate action potentials. The NFS cell example (third from top) trace in 8.5 mM K⁺ shows the last action potential this cell was able fire before completely entering depolarization block. **D** Left side displays percentages of PCs and PV cells in depolarization block after 15 minutes or less in 8.5 mM extracellular [K⁺]. Right side displays percentages of PV+INT physiological subtypes.

Single-cell nuclear RNAsequencing (snRNA-seq) reveals molecular changes in response to *LIS1* loss

Finally, we used snRNA-seq sequencing to understand how *LIS1* haploinsufficiency impacts gene expression in the subtypes of PV+INTs. GlobalLis mice were crossed to PVCre;Sun1-GFP mice to enable targeting of single PV+INT nuclei. We microdissected hippocampi of p20 WT and GlobalLis mice, lysed the cells, and performed snRNA-seq on fluorescence-sorted GFP⁺ PV+INT nuclei (Figure 7A). As a first pass, to establish the identities of the PV+ subtypes, we integrated and aligned this dataset with other established single-cell RNAseq profiles of **(i)** a publicly available pan-GABAergic Allen Brain Institute mouse dataset (Tasic et al., 2018), and **(ii)** *Nkx2.1*-cre, MGE-derived cortical and hippocampal interneurons (Mahadevan et al., 2020) using Seurat v3 (Butler et al., 2018, Stuart et al., 2019). We assigned the putative identities of *Gad1*⁺ *Pvalb*⁺ subtypes as fast-spiking basket cells (BC), axo-axonic cells (AAC) or bistratified (BiC) subtypes, using the marker expressions *Tac1*, *Pthlh* or *Sst* respectively, and these marker expressions mapped well with the reference datasets indicating a high confidence in the quality of snRNAseq (Figure 7—figure supplements 1-2). Focusing on the PV+INTs from WT and GlobalLis datasets (1781 and 1623 single-nuclei respectively) for subsequent analysis, we first observed that the entirety of the UMAP space aligns well between WT and GlobalLis (Figure 7B_i), and the cell recovery

numbers of the BC, AAC and BiC subtypes matches well between the genotypes (Figure 7Bii). This indicates that *LIS1* haploinsufficiency does not lead to gross differences in the fundamental transcriptomic identities or the overall cell recoveries of PV+INT subtypes (Figure 7B).

Because we observed robust disruption in the morphophysiological development and laminar positioning of GlobalLis PV+INTs, we examined the full range of transcriptional impairments triggered by *LIS1* haploinsufficiency in PV+INT subtypes, by performing differential gene expression testing. At a stringent false-discovery rate (FDR) <0.01, 376 genes passed the 10%-foldchange (FC) threshold across the PV+INT subtypes of which, 126 genes were commonly differentially expressed (DE) between the subtypes and the remaining 250 genes were uniquely DE across the subtypes (Figure 7C; Supplemental Table 1). To assess the broad biological impact of the DE genes (DEG), we applied the Ingenuity Pathway Analysis (IPA) framework. These analyses revealed that the DEGs primarily serve to regulate synaptogenesis signaling pathways, glutamatergic/GABAergic neurotransmission, different distinct guidance cues, cell-cell adhesion, and maintenance of extracellular matrix (ECM; Figure 7D; Supplemental Table 2).

First, we observed misregulated expressions of cell-adhesion molecules (CAMs) belonging to cadherin family (*Cdh8-13*), contactin and related family (*Cntn3-6, Cntnap3,5b*), IgCAM family (*Alcam, Dscam, Dscaml1, Ncam2, Kirrel1,3, Igsf11*), including multiple CAM-modifiers (*St3gal4, St6gal1*) (Figure 7E). It is notable that multiple members of the CAM family are established regulators of interneuron synapse assembly, axonal and dendritic arborization (Brenneman and Maness 2008, Brenneman et al., 2013, Guan and Maness 2010, Gomez-Climent et al., 2011, Krocher et al., 2014, Gao et al., 2018). Next, we also observed several members of signaling pathways belonging to netrin family (*Ntn1, Unc5b, Dcc, Ntn4*), ephrin family (*Efna5, Eph3,*

Epha4), robo family (*Slit1*, *Slit3*) and semaphorin family (*Sema5a*, *Sema6a*, *Neto1*, *Neto2*), are robustly downregulated subsequent to *LIS1* haploinsufficiency (Figure 7F), many of which have well-defined functions in MGE-derived interneuron migration and morphological development (Andrews et al., 2006, 2008, Tran et al, 2007, van den Berghe et al., 2013, Steinecke et al., 2014). This collectively indicates that multiple cellular mechanisms can converge towards regulating PV+INT morphology in a *LIS1*-dependant cell-autonomous manner.

Based on the *LIS1* haploinsufficiency associated changes in PV+INT firing properties and propensity for depolarization block we further scrutinized our transcriptome datasets for cell-autonomous changes that could impact membrane excitability. Several critical regulators of PV+INT excitability (Pelkey et al., 2017) including members of potassium channel family (*Kcnj3*, *Kcnq5*, *Kcnh7*, *Kcnb2*, *Kcnk2*, *Kcnp1*, *Kcnp2*) were misregulated in GlobalLis PV+INTs (Figure 7G; Supplemental Table 1). In addition, two GlobalLis PV+INT clusters displayed altered levels of the key neurotransmitter release regulator *Syt2* (Supplemental Table 1), potentially reflecting the increased contribution of IS PV+INTs which display reduced unitary amplitudes and release probability in combination with longer latencies. We also observe that the chloride loader NKCC1 (*Slc12a2*) appears to be decreased in subset of basket cells which might also influence somatic chloride extrusion during high-frequency firing in PV+INTs, thereby influencing PV+INT excitability (Otsu et al., 2020). Finally, we observed altered expression patterns of glutamate receptors and associated auxiliary subunits (*Grik1-4*, *Neto1*, *Neto2*) (Figure 7H) that are previously established to regulate excitatory recruitment of PV+INTs (Pelkey et al., 2017, Christensen et al., 2004, Wyeth et al., 2017, Mulle et al., 2000).

FIGURE 7

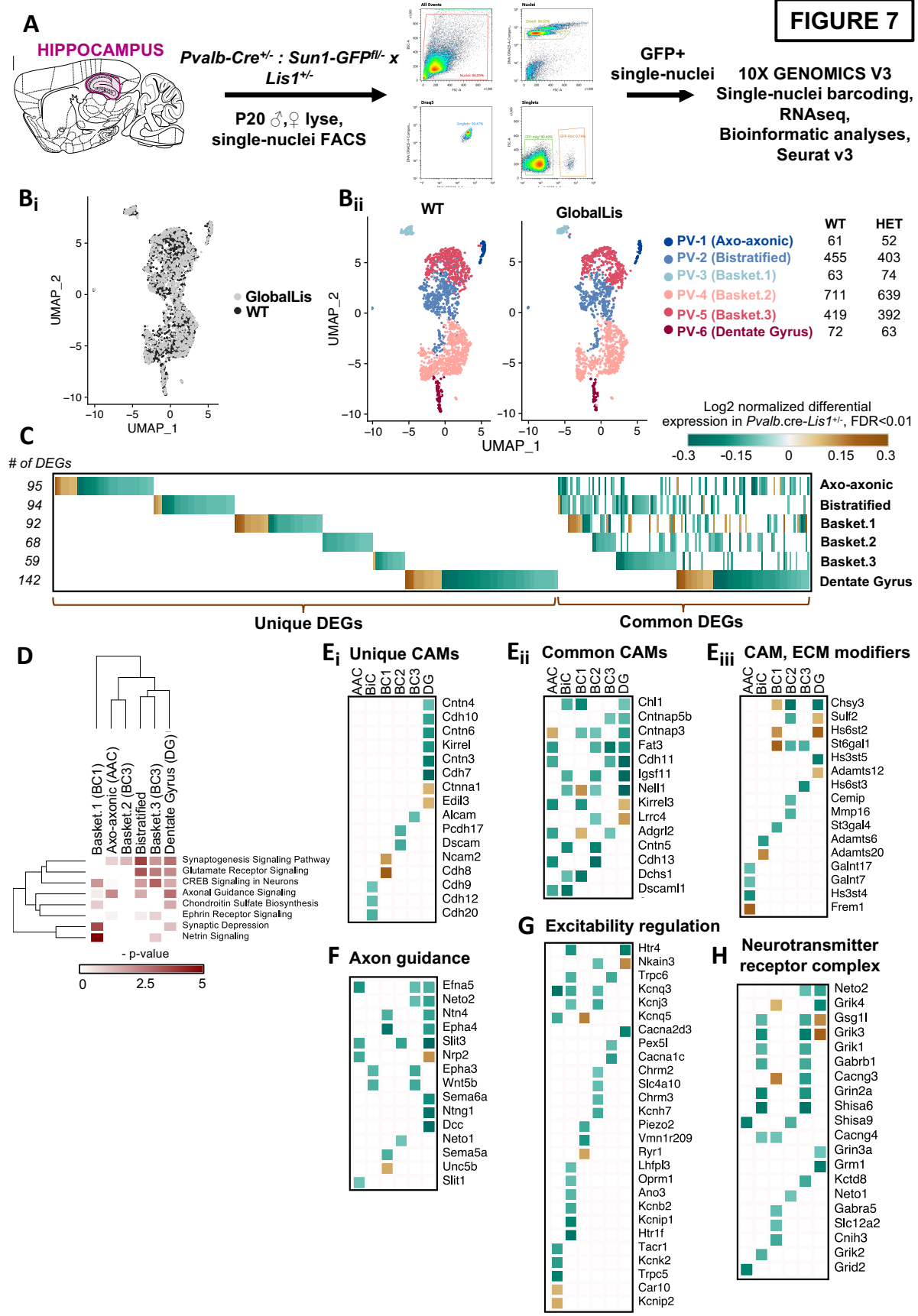


Figure 7. Examination of *LIS1* haploinsufficiency on PV+INTs using single nucleus RNAseq. **A** Overview of the experimental workflow. **Bi** Uniform Manifold Approximation and Projection (UMAP) dimensional reduction of single-nuclei transcriptomes of hippocampal PV+INTs, highlighting similar enrichments of the clusters between genotypes. **Bii** UMAP visualization of Axo-axonic, Bistratified and Fast-spiking PV+INT subtypes, and table indicating the number of Gad1/Pvalb+ cells recovered in each PV+INT. Cell clusters were color coded and annotated post hoc based on their transcriptional profile identities (Abbreviations: FS, Fast-spiking; DG, Dentate gyrus). **C** Combined heatmap representing the 376 differentially expressed (DE) in hippocampal PV+INTs upon *LIS1* haploinsufficiency, at FDR <0.01 and Fold Change (FC)>10%, as determined by MAST analysis. **D** Ingenuity Pathway Analysis of significantly overrepresented molecular pathways in each PV+INT subtype. **E-H** Heatmap of log₂ FC of significant DE genes in each PV+INT subtype, showing a subset of **Ei**, uniquely DE cell-adhesion molecules (CAMs), **Eii**, commonly DE CAMs, **Eiii**, DE extracellular matrix modifying genes; **F**, genes regulating axon guidance; **G**, regulators of neuronal excitability, and **H**, postsynaptic glutamate receptor subunits and associated auxiliary subunits.

CONCLUSIONS

LIS1 haploinsufficiency disrupts numerous genetic programs controlling PV+INT migration, morphogenesis, synapse formation and cellular excitability. We report that global heterozygous *LIS1* loss (GlobalLis) and heterozygous loss within interneurons (NkxLis) but not within pyramidal cells (EmxLis) results in the emergence of the non-canonical “intermediate-spiking” (IS) subtype of PV+INTs, despite the disruption of radial migration observed in all three genotypes.

While WT (and EmxLis) FS cells consist of four morphological subtypes (BC, AAC, BiC, RTC) and NFS cells consisted of two subtypes (BC, RTC), clear morphology of GlobalLis and NkxLis PV+INTs could not be resolved. Interestingly, the emergence of IS cells and alteration of morphology in the GlobalLis mutant did not correlate with any additional PV+INT clusters in the snRNA-seq analysis. However, the snRNA-seq presents only a snapshot of the transcriptomic aberrations in PV+INTs due to Global *LIS1* haploinsufficiency. Therefore, the lack of a distinct IS population in the snRNA-seq analysis could imply that alterations of a very small number of genes are responsible for changes, which would not result in any additional clustering. It is possible that the cellular changes observed may arise from epigenetic changes, changes in protein expression levels, or changes in modifications of proteins that would not be detectable in this dataset. A third

possibility is that changes during development alter the circuit integration and maturation of PV+INTs and these changes might not be evident in their mature transcriptome. Finally, it is possible that the morphological aberrations in PV+INTs are further shaped by the transcriptomic aberrations in other cell types. Because *LIS1*-disruption in pyramidal cells does not seem to affect PV+INT morphological maturation, future studies could examine *LIS1*-disruption exclusive to glial cells to examine such non-autonomous mechanisms of regulation of interneuron functions. For example, glial cells that are also impacted by *LIS1* haploinsufficiency, also secrete several guidance cues that shape the assembly, lamination and morphology of interneurons (Vallee and Tsai 2006, Yokota et al., 2007). Therefore, such cell-autonomous and non-autonomous mechanisms could converge to regulate PV+INT morphological maturation.

We observed that both WT and *EmxLis* CA1 are composed of 79-80% FS cells (preferentially found in deep layers) and 19-20% NFS cells (preferentially in superficial layers). In contrast, FS cells make up only 44% of *GlobalLis* and 29% of *NkxLis* PV+INTs, with the majority (56-71%) consisting of IS/NFS (which are also preferentially found in superficial layers). Compared to FS cells, IS and NFS cells have lower firing rates and provide less potent, less reliable inhibitory output to pyramidal cells. Thus, the expansion of these non-canonical cell types will erode the precise inhibition usually provided by FS cells, placing network excitability on the precipice for electrographic seizure activity. Finally, due to their propensity to enter depolarization block, IS and NFS cells will likely lose the ability to initiate action potentials and control runaway excitation during seizure episodes, allowing epileptic activity to spread from the hippocampus to other brain regions. Until now, the disrupted neuronal migration in classical lissencephaly has been paradigmatically linked to the generation of epileptiform activity, however our *EmxLis* and *NkxLis*

experiments challenge this assumption. We propose that it is not disrupted neuronal migration perse that underlies the origin of epilepsy, but rather disruptions to intrinsic developmental programs that result in the emergence of a less efficient PV+INT cell type.

METHODS

Animals

All experiments were conducted in accordance with animal protocols approved by the National Institutes of Health. *LIS1*^{+/*fl*} male mice (provided by Anthony Wynshaw-Boris, Case Western Reserve University) were crossed with Sox2-Cre female mice (provided by National Human Genome Research Institute transgenic core, Tg(Sox2-Cre)1Amc/J). Sox2-Cre females exhibit Cre-recombinase activity in gamete tissues, which allow for genotyping and selection of non-conditional *LIS1*^{+/*-*} mutants without the Cre allele in a single cross. These mice were bred to wild-type C57BL/6J mice (Jackson Labs stock no. 00064) to maintain global *LIS1*^{+/*-*} colonies. To obtain cell-type-specific *LIS1* mutations, we crossed *LIS1*^{+/*fl*} mice to Nkx2.1-Cre (Jackson Labs stock no. 008661, C57BL/6J-Tg(Nkx2-1-cre)2Sand/J) and Emx1-Cre (Jackson Labs stock no. 005628, B6.129S2-Emx1^{tm1(cre)Krj}/J) lines.

To enable genetic access and targeting of PV+ cells, *Lis1* mutant lines were crossed to PV-tdTomato reporters. *LIS1*^{+/*-*} mice were crossed to PV-Cre (Jackson Labs stock no. 017320, B6.129P2-Pvalb^{tm1(cre)Arbr}/J) and tdTomato mice (Jackson Labs stock no. 007909, B6.Cg-Gt(ROSA)26Sor^{tm9(CAG-tdTomato)Hze}/J). *LIS1*^{fl/+}:Nkx2.1Cre and *Lis1*^{fl/+}::Emx1Cre lines were crossed to Cre-independent PV-TdTom mice (Jackson Labs stock no. 027395, Tg(Pvalb-tdTomato15Gfng).

For single-cell nuclear RNAseq experiments, Lis1+/-:PV-Cre mice were crossed to Sun1-GFP mice (Jackson Labs stock no. 030952, B6.129-Gt(ROSA)26Sor^{tm5(CAG-Sun1/sfGFP)Nat}/MmbeJ).

Male and female mice from p19-p60 were used. Mice were housed and bred in a conventional vivarium with standard laboratory chow and water in standard animal cages under a 12 h circadian cycle.

Immunohistochemistry on perfused tissue

Mice were deeply anesthetized, and tissue was fixed via transcardial perfusion with 30mL of phosphate-buffered saline (PBS) followed by 50 mL of 4% paraformaldehyde (PFA) in 0.1 M phosphate buffer (PB, pH 7.6). Brains were post-fixed overnight at 4°C when processed for immunostaining for PV and NeuN. Brains were cryopreserved in 30% sucrose and sectioned on a freezing microtome at 50 µm. Sections were rinsed in PB, blocked for 2 hours in 10% normal goat serum with 0.5% Triton X-100, and then incubated in primary antibody for 2 hours at room temperature or overnight at 4°C. Sections were then rinsed with PB and incubated in secondary antibodies (1:1000) and DAPI (1:2000) for 2 hours at room temperature. All antibodies were diluted in carrier solution consisting of PB with 1% BSA, 1% normal goat serum, and 0.5% Triton X-100. Sections were then rinsed, mounted on Superfrost glass slides, and coverslipped using Mowiol mounting medium and 1.5 mm cover glasses.

Image acquisition and analysis

Confocal images were taken using a Zeiss 780 confocal microscope. For all slices with immunostained or genetically reported somatic signal, 50 µm thin sections were imaged using a

Nikon spinning disk (Yokogawa CSU-X) confocal microscope. Counting was performed on four hippocampal sections from each animal. Quantitative analysis of PV+ cell density in each CA1 layer was performed using ImageJ software (NIH, Bethesda, MD, USA).

Slice preparation

Mice (p19-p60) were anesthetized with isoflurane and then decapitated. The brain was dissected out in ice-cold sucrose artificial cerebrospinal fluid (aCSF) containing the following (in mM): 130 NaCl, 3.5 KCl, 24 NaHCO₃, 1.25 NaH₂PO₄, 1.5 MgCl₂, 2.5 CaCl₂, and 10 glucose, saturated with 95% O₂ and 5% CO₂. Mice older than p30 were dissected in sucrose-substituted artificial cerebrospinal fluid (SSaCSF) containing the following (in mM): 90 sucrose, 80 NaCl, 3.5 KCl, 24 NaHCO₃, 1.25 NaH₂PO₄, 4.5 MgCl, 0.5 CaCl₂, and 10 glucose, saturated with 95% O₂ and 5% CO₂. Coronal hippocampal slices (300 μm) were cut using a VT-1200S vibratome (Leica Microsystems) and incubated submerged in the above solution at 32-34°C for 30 min and then maintained at room temperature until use. Slices were incubated for at least 45 minutes before conducting electrophysiological recordings.

Whole-cell electrophysiology

For patch-clamp recordings following recovery slices were transferred to an upright microscope (Zeiss Axioskop), perfused with aCSF (with or without SCZD as indicated) at 2-3 ml/min at a temperature of 32°C-34°C. Individual cells were visualized using a 40x objective using fluorescence and IR-DIC video microscopy. Electrodes were pulled from borosilicate glass (World Precision Instruments) to a resistance of 3–5 MΩ using a vertical pipette puller (Narishige, PP-

830). Whole-cell patch-clamp recordings were made using a Multiclamp 700B amplifier (Molecular Devices), and signals were digitized at 20 kHz (Digidata 1440A, filtered at 3 kHz) for collection on a Windows computer equipped with pClamp 10.4 software (Molecular Devices). Uncompensated series resistance ranged from 10 to 35 M Ω and was monitored continuously throughout recordings with -5 mV voltage steps. For current-clamp and voltage-clamp recordings of PV-Cre-tdTom⁺ interneurons and CA1 pyramidal cells, two different internal solutions containing (in mM) were used: A) 130 K-gluconate, 5 KCl, 10 HEPES, 3 MgCl₂, 2 Na₂ATP, 0.3 NaGTP, , 0.6 EGTA, and 0.2% biocytin (calculated chloride reversal potential (E_{Cl}⁻) of -67 mV) or B) 130 K-Gluconate, 10 KCl, 10 HEPES, 3 MgCl₂, 2 Na₂ATP, 0.3 NaGTP, 0.6 EGTA and .2% biocytin (calculated E_{Cl}⁻ = -27 mV).

Input resistance (R_{in}) was measured using a linear regression of voltage deflections in response to 500 ms-long current steps of four to six different amplitudes (-200 to $+50$ pA, increments of 50 pA). Membrane time constant (τ_m) was calculated from the mean responses to 20 successive hyperpolarizing current pulses (-20 pA; 400 ms) and was determined by fitting voltage responses with a single exponential function. Action potential (AP) threshold was defined as the voltage at which the slope trajectory reaches 10 mV/ms. AP amplitude was defined as the difference in membrane potential between threshold and the peak. AP half-width was measured at the voltage corresponding to half of the AP amplitude. Afterhyperpolarization (AHP) amplitude was defined as the difference between action potential threshold and the most negative membrane potential attained during the AHP. These properties were measured for the first action potential elicited by a depolarizing 500 ms-long current pulse of amplitude just sufficient to bring the cell to threshold for AP generation. The adaptation ratio was defined as the ratio of

the average of the last 3 interspike intervals relative to the first 3 interspike intervals during a 500 ms-long spike train elicited using twice the current injection necessary to obtain a just suprathreshold response. Firing patterns were investigated by a series of 500 to 800 ms-long current injections (step size 50 pA) until 3x threshold current was reached or depolarization-block was induced. Firing frequency was calculated from the number of spikes observed during the first 500 ms of the spike train. Firing frequency at 3x threshold was substituted by maximum firing frequency in cells with depolarization-block. Ihyp Sag index of each cell was determined by a series of 500 ms-long negative current steps to create V-I plots of the peak negative voltage deflection (V_{hyp}) and the steady-state voltage deflection (average voltage over the last 200 ms of the current step; V_{sag}) and used the ratio of $V_{rest}-V_{sag}/V_{rest}-V_{hyp}$ for current injections corresponding closest to $V_{sag}=-80\text{mV}$.

For PV+INT-CA1PC paired recordings, the presynaptic PV+INT was held in current clamp with membrane potential biased to -70 mV, while the postsynaptic cell was held voltage clamp at -70 mV. Synaptic transmission was monitored by producing action potentials in presynaptic PV+INTs (held in current-clamp around -70 mV) every 10s by giving 2 ms 1-2 nA current steps. Presynaptic trains to probe unitary transmission dynamics consisted of 25 presynaptic action potentials at 50 Hz. Basal unitary event properties for each cell were analyzed using 10 consecutive events obtained 4-5 minutes after establishing the postsynaptic whole-cell configuration. Amplitudes reflect the average peak amplitude of all events including failures, potency is the average peak amplitude excluding failures. Decay kinetics were measured by single exponential fit of uIPSC potency. The latency of synaptic transmission was defined as the time from the peak of the AP to 5% of the uIPSC potency.

For depolarization block experiments, WT and GlobalLis TdT+PV+INTs were recorded in current-clamp mode. Rheobase, input resistance, AP half-width, firing frequency at 2 threshold x and maximum firing frequency were recorded (and used to identify physiological subtype) using above protocols. Further depolarizing current was injected in 500 ms sweeps with a step size of 50 pA until cells were subject to depolarizing block or 1500 pA of current were injected. Following this, 10 second sweeps of spontaneous activity with 500 ms of evoked firing (with ~1.5x threshold current) were taken. After obtaining a stable baseline (~10 sweeps), the extracellular solution was switched to a solution with 8.5 mM [K+] the same 10 second (500 ms evoked firing) sweeps were taken for up to 15 minutes.

Clustering Analysis

To identify potential subclusters of PV+INTs, we performed principal components analysis (PCA) and hierarchical clustering based on Euclidean distance of normalized (log transformed) intrinsic electrophysiological parameters using R-studio version 0.99.451 and R version 3.4.2.

Anatomical Reconstructions

After biocytin filling during whole-cell recordings, slices were fixed with 4% paraformaldehyde and stored at 4°C then permeabilized with 0.3 % Triton X-100 and incubated with Alexa Fluor 488 or Alexa Fluor 555-conjugated streptavidin. Resectioned slices (75 μ m) were mounted on gelatin-coated slides using Mowiol mounting medium. Cells were visualized using epifluorescence microscopy and images for representative examples were obtained with confocal microscopy.

Cells were reconstructed and analyzed with Sholl analysis using NeuroLucida software (MBF Bioscience).

Statistical Analysis

All data were tested for normality and then tested with parametric or nonparametric t-test or ANOVA, as appropriate (Graphpad Prism). Quantification and error bars display standard error of the mean. Intrinsic electrophysiological parameters in the text are values for the upper and lower 95% confidence intervals of the mean. Values shown for unitary synaptic transmission properties consist of mean and standard error of the mean.

Single nucleus isolation

Hippocampus from seven mutant (*Lis^{+/-};PV-Cre^{+/-};Sun1-GFP^{+/-}*) and six WT (*Lis^{-/-};PV-Cre^{+/-}; Sun1-GFP^{+/-}*) P21 mice were quickly dissected in ice-cold DPBS, immediately frozen on dry ice and stored at -80°C. We pooled mutant or WT hippocampus into a Dounce Homogenizer containing 1 mL freshly prepared ice-cold lysis buffer (low sucrose buffer with 1 mM DTT, 0.1% NP-40), applying 10 strokes with pestle A followed by 10 strokes with the pestle B. The homogenate was filtered through a 40 µm cell strainer, transferred to a DNA low bind 2 mL microfuge tube and centrifuged at 300 g for 5 min at 4°C. The supernatant was removed, the pellet was gently resuspended in a low sucrose buffer (320 mM sucrose, 10 mM HEPES-pH 8.0, 5 mM CaCl₂, 3 mM Mg-acetate, 0.1 mM EDTA) and centrifuged for another 5 min. The nuclei were resuspended in 500 µl 1xPBS with 1% BSA and 0.2 U/µl SUPERaseIn RNase Inhibitor (ThermoFisher, #AM2696) and loaded on top of 900 µl 1.8 M Sucrose Cushion Solution (Sigma, NUC-201). The sucrose

gradient was centrifuged at 13,000 g for 45 min at 4°C. The supernatant was discarded, and the nuclei were resuspended in 500ul Pre-FACS buffer (1xPBS with 1% BSA, 0.2 U/μl SUPERaseIn RNase Inhibitor and 0.2 M sucrose). Before sorting, nucleus from the six WT or seven mutant mice were pooled together and 5ul of 5 mM DRAQ5 were added.

Samples were processed on a Sony SH800 Cell Sorter with a 100 mm sorting chip. 15,000 GFP+/DRAQ5+ nuclei from mutant and WT samples were collected directly into 1.5 ml centrifuge tubes containing 10ul of the Pre-FACS buffer. PCR cycles were conducted for cDNA amplification, and the subsequent library preparation and sequencing were carried out in accordance with the manufacturer recommendation (Chromium™ Single Cell 3' Library & Gel Bead Kit 10X v3, 16 reactions). Sequencing of the libraries were performed on the Illumina HiSeq2500 at the NICHD, Molecular Genomics Core facility. The cell number estimates, mean reads per cell (raw), median genes per cell respectively, are as follows *LIS1*^{+/+}: 8470, 22,289, 2024; *LIS1*^{+/-}: 8185, 24,652, 2142. Demultiplexed samples were aligned to the mouse reference genome (mm10). The end definitions of genes were extended 4k bp downstream (or halfway to the next feature if closer) and converted to mRNA counts using the Cell Ranger Version 2.1.1, provided by the manufacturer.

RNAseq data processing & analyses, differential expression testing, and visualization

Processing (load, align, merge, cluster, differential expression testing) and visualization of the scRNAseq datasets were performed with the R statistical programming environment (v3.5.1) (R Core Team 2013), and Seurat package (v3.1.5) (Butler et al., 2018, Stuart et al., 2019). The *LIS1*^{+/+} and *LIS1*^{+/-} datasets were first merged with the Allen Institute reference and in-house MGE interneuron reference datasets. To analyze the Allen Institute mouse dataset of the single-cell

transcriptomes of ~76,000 cells from >20 areas of mouse cortex and hippocampus, we downloaded the transcriptome/HDF5 file (<https://portal.brain-map.org/atlas-and-data/rnaseq>) and subsequently converted into Seurat v3-compatible format based on the instructions provided in the Allen Institute Portal (<https://portal.brain-map.org/atlas-and-data/rnaseq/protocols-mouse-cortex-and-hippocampus>) and custom scripts in R package as previously described (Chittajallu et al., 2020). Single-cell transcriptomes from *Nkx2.1-cre:Ai14*, MGE-derived cortical and hippocampal interneurons (postnatal day 18-20) were processed as previously described (Mahadevan et al., 2020). To perform integrated analyses, we identified a common set of genes between *LIS1*^{+/+}, *LIS1*^{+/-}, *Nkx2.1*-MGE cortical and hippocampal interneurons and Allen datasets, and utilized these for the initial analyses in Figure 7—figure supplements 1-2. Data set preprocessing, normalization, identification of variable genes, canonical correlation analyses were performed according to default Seurat parameters, unless otherwise mentioned. Quality control filtering was performed by only including cells that had between 200-20000 unique genes, and that had <5% of reads from mitochondrial genes. Clustering was performed on the top 25 PCs using the function `FindClusters()` by applying the shared nearest neighbor modularity optimization with clustering resolution of 0.5. Phylogenetic tree relating the 'average' cell from each identity class based on a distance matrix constructed in gene expression space using the `BuildClusterTree()` function. Overall, we identified 36 clusters using this approach, among which clusters 12, 13, 16, 17 are highly enriched in the *LIS1*^{+/+}, *LIS1*^{+/-}, datasets and aligned well in their corresponding UMAP spaces with the reference datasets. The identities of clusters 12, 13, 16, 17 are matched with the top gene markers identified by the `FindAllMarkers()`. These 4 clusters are *Gad1*⁺, *Pvalb*⁺ and *Vip*⁻, and were putatively annotated as Bistratified.1/2, Fast-spiking and Axo-axonic subsets of PV+INTs, based on marker expression of *Sst*, *Tac1* and *Pthlh* respectively, as indicated in interneuron literature and previous scRNAseq studies (Fishell and Kepecs, 2020; Hodge et al., 2019; Paul et al., 2017; Pelkey et al., 2017; Saunders et al., 2018; Tasic et al., 2016, 2018; Yao et al., 2020; Harris et al., 2018). Subsequent to dataset validation using references, the *LIS1*^{+/+} and *LIS1*^{+/-} datasets

reanalyzed by subsetting the cells that expressed *Gad1*, *Pvalb* expression > 0.1 and by excluding the cells containing non-PV+INT genes *Slc17a7*, *Ttr*, *Scn3a*, *Gpc5*, *Slc1a2*, *Htr2c*, *Trpm3* expressions < 0.1. Clustering was performed on the top 25 PCs using the function `FindClusters()` by applying the shared nearest neighbor modularity optimization with clustering resolution of 0.5. Similar to prior analyses, we recovered Bistratified, Fast-spiking and Axo-axonic subsets of PV+INTs. Additionally, a minor population of *Nos1+* cells clearly segregated, which represents putative dentate gyrus-expressed PV+INTs (Vaden and Gonzalez et al., 2020, Shen et al., 2019, Jinno and Kosaka 2002).

Differential gene expression testing were performed using the MAST package within the `FindMarkers()` function to identify the differentially expressed genes between two subclusters (Finak et al., 2015). We applied a stringent false-discovery rate <0.01, and minimum logFC in our DEGs as ± 0.1 , since MAST has been previously reported to underestimate the magnitude of fold change (Ximerakis et al., 2019, Mahadevan et al., 2020). Moreover, previous studies have demonstrated the MAST approach for DEG testing to be powerful in determining subtle changes in highly transcribed genes, and among abundant populations, additional to underrepresenting changes among weakly transcribed genes (Finak et al., 2015; Ximerakis et al., 2019). Molecular and functional annotation of the DEGs were conducted using Ingenuity Pathway Analyses platform, to identify the biological pathways and disease pathways over-represented. IPA was also used to annotate genes with their known cellular functional classes. Heatmaps for the DEGs were generated using the Morpheus package (<https://software.broadinstitute.org/morpheus>) within the R framework.

Acknowledgements

We thank Dr. Carolina Bengtsson-Gonzales for developing the code for cluster analysis. We thank Drs. Kenneth Pelkey and Ramesh Chittajallu for discussing project ideas and technical details of experiments. We thank Dr. Gülcan Akgül for developing *LIS1* primers for genotyping. We thank Steven Hunt for genotyping and cell processing for microscopy. We thank Daniel Abebe for

animal support. We thank Dr. Vincent Schram and the NICHD imaging core for confocal microscopy support. We thank Drs. Steven L. Coon, Tianwei Li and James R. Iben at the Molecular Genomics Core, NICHD, for RNA sequencing and bioinformatics support. We thank Drs. Apratim Mitra and Ryan Dale (NICHD Bioinformatics and Scientific Programming Core) for assistance with integrated analysis using the Allen Brain scRNAseq dataset. These analyses utilized the computational resources of the NIH HPC Biowulf cluster (<http://hpc.nih.gov>). We thank Dr. Anthony Wynshaw-Boris for providing the heterozygous floxed *LIS1* mouse.

Funding

Chris McBain was supported by an NICHD Intramural Research Award

Competing Interests

None.

References

- Ahmed**, O. J., Kramer, M. A., Truccolo, W., Naftulin, J. S., Potter, N. S., Eskandar, E. N., ... Cash, S. S. (2014). Inhibitory single neuron control of seizures and epileptic traveling waves in humans. *BMC Neuroscience*, *15*(Suppl 1), F3. <https://doi.org/10.1186/1471-2202-15-S1-F3>
- Andrews**, W., Barber, M., Hernandez-Miranda, L. R., Xian, J., Rakic, S., Sundaresan, V., ... Parnavelas, J. G. (2008). The role of Slit-Robo signaling in the generation, migration and morphological differentiation of cortical interneurons. *Developmental Biology*, *313*(2), 648–658. <https://doi.org/10.1016/j.ydbio.2007.10.052>
- Andrews**, W., Liapi, A., Plachez, C., Camurri, L., Zhang, J., Mori, S., ... Richards, L. J. (2006). Robo1 regulates the development of major axon tracts and interneuron migration in the forebrain. *Development*, *133*(11), 2243–2252. <https://doi.org/10.1242/dev.02379>
- Bartolini**, G., Ciceri, G., & Marín, O. (2013). Integration of GABAergic Interneurons into Cortical Cell Assemblies: Lessons from Embryos and Adults. *Neuron*, *79*(5), 849–864. <https://doi.org/10.1016/j.neuron.2013.08.014>
- Brenneman**, L. H., Zhang, X., Guan, H., Triplett, J. W., Brown, A., Demyanenko, G. P., ... Maness, P. F. (2013). Polysialylated NCAM and EphrinA/EphA regulate synaptic development of

gabaergic interneurons in prefrontal cortex. *Cerebral Cortex*, 23(1), 162–177.
<https://doi.org/10.1093/cercor/bhr392>

Brenneman, L. H., & Maness, P. F. (2008). Developmental regulation of GABAergic interneuron branching and synaptic development in the prefrontal cortex by soluble neural cell adhesion molecule. *Molecular and Cellular Neuroscience*, 37(4), 781–793.
<https://doi.org/10.1016/j.mcn.2008.01.006>

Butler, A., Hoffman, P., Smibert, P., Papalexi, E., & Satija, R. (2018). Integrating single-cell transcriptomic data across different conditions, technologies, and species. *Nature Biotechnology*, 36(5), 411–420. <https://doi.org/10.1038/nbt.4096>

Chittajallu, R., Auville, K., Mahadevan, V., Lai, M., Hunt, S., Calvigioni, D., ... McBain, C. J. (2020). Activity-dependent tuning of intrinsic excitability in mouse and human neurogliaform cells. *eLife*, 9, 1–25. <https://doi.org/10.7554/eLife.57571>

Christensen, J. K., Paternain, A. V., Selak, S., Ahring, P. K., & Lerma, J. (2004). A mosaic of functional kainate receptors in hippocampal interneurons. *Journal of Neuroscience*, 24(41), 8986–8993. <https://doi.org/10.1523/JNEUROSCI.2156-04.2004>

Corbo, J. C., Deuel, T. A., Long, J. M., LaPorte, P., Tsai, E., Wynshaw-Boris, A., & Walsh, C. A. (2002). Doublecortin is required in mice for lamination of the hippocampus but not the neocortex. *The Journal of Neuroscience : The Official Journal of the Society for Neuroscience*, 22(17), 7548–7557. <https://doi.org/22/17/7548> [pii]

D'amour, J. A., Ekins, T., Ganatra, S., Yuan, X., & McBain, C. J. (2020). Aberrant sorting of hippocampal complex pyramidal cells in type I lissencephaly alters topological innervation. *eLife*, 9, 1–26. <https://doi.org/10.7554/eLife.55173>

Di Donato, N., Chiari, S., Mirzaa, G. M., Aldinger, K., Parrini, E., Olds, C., ... Dobyns, W. B. (2017). Lissencephaly: Expanded imaging and clinical classification. *American Journal of Medical Genetics, Part A*, 173(6), 1473–1488. <https://doi.org/10.1002/ajmg.a.38245>

Drexel, M., Romanov, R. A., Wood, J., Weger, S., Heilbronn, R., Wulff, P., ... Sperk, G. (2017). Selective Silencing of Hippocampal Parvalbumin Interneurons Induces Development of Recurrent Spontaneous Limbic Seizures in Mice. *The Journal of Neuroscience : The Official Journal of the Society for Neuroscience*, 37(34), 8166–8179.
<https://doi.org/10.1523/JNEUROSCI.3456-16.2017>

Fishell, G., & Kepecs, A. (2020). Interneuron Types as Attractors and Controllers. *Annual Review of Neuroscience*, 43, 1–30. <https://doi.org/10.1146/annurev-neuro-070918-050421>

Fleck, M. W., Hirotsune, S., Gambello, M. J., Phillips-Tansey, E., Soares, G., Mervis, R. F., ... McBain, C. J. (2000). Hippocampal abnormalities and enhanced excitability in a murine

model of human lissencephaly. *Journal of Neuroscience*, 20(7), 2439–2450.
<https://doi.org/10729324>

- Gao, R.,** Piguel, N. H., Melendez-Zaidi, A. E., Martin-de-Saavedra, M. D., Yoon, S., Forrest, M. P., ... Penzes, P. (2018). CNTNAP2 stabilizes interneuron dendritic arbors through CASK. *Molecular Psychiatry*, 23(9), 1832–1850. <https://doi.org/10.1038/s41380-018-0027-3>
- Gómez-Climent, M. Á.,** Guirado, R., Castillo-Gómez, E., Varea, E., Gutierrez-Mecinas, M., Gilabert-Juan, J., ... Nacher, J. (2011). The polysialylated form of the neural cell adhesion molecule (PSA-NCAM) is expressed in a subpopulation of mature cortical interneurons characterized by reduced structural features and connectivity. *Cerebral Cortex*, 21(5), 1028–1041. <https://doi.org/10.1093/cercor/bhq177>
- Gouwens, N. W.,** Sorensen, S. A., Baftizadeh, F., Budzillo, A., Lee, B. R., Jarsky, T., ... Zeng, H. (2020). Toward an Integrated Classification of Cell Types: Morphoelectric and Transcriptomic Characterization of Individual GABAergic Cortical Neurons. *BioRxiv*. <https://doi.org/10.2139/ssrn.3544405>
- Gouwens, N. W.,** Sorensen, S. A., Berg, J., Lee, C., Jarsky, T., Ting, J., ... Koch, C. (2019). Classification of electrophysiological and morphological neuron types in the mouse visual cortex. *Nature Neuroscience*, 22(7), 1182–1195. <https://doi.org/10.1038/s41593-019-0417-0>
- Greenwood, J. S. F.,** Wang, Y., Estrada, R. C., Ackerman, L., Ohara, P. T., & Baraban, S. C. (2009). Seizures, enhanced excitation, and increased vesicle number in Lis1 mutant mice. *Annals of Neurology*, 66(5), 644–653. <https://doi.org/10.1002/ana.21775>
- Guan, H., & Maness, P. F.** (2010). Perisomatic GABAergic innervation in prefrontal cortex is regulated by ankyrin interaction with the L1 cell adhesion molecule. *Cerebral Cortex*, 20(11), 2684–2693. <https://doi.org/10.1093/cercor/bhq016>
- Harris, K. D.,** Hochgerner, H., Skene, N. G., Magno, L., Katona, L., Bengtsson Gonzales, C., ... Hjerling-Leffler, J. (2018). Classes and continua of hippocampal CA1 inhibitory neurons revealed by single-cell transcriptomics. In *PLoS Biology* (Vol. 16). <https://doi.org/10.1371/journal.pbio.2006387>
- Herbst, S. M.,** Proepper, C. R., Geis, T., Borggraefe, I., Hahn, A., Debus, O., ... Hehr, U. (2016). LIS1-associated classic lissencephaly: A retrospective, multicenter survey of the epileptogenic phenotype and response to antiepileptic drugs. *Brain and Development*, 38(4), 399–406. <https://doi.org/10.1016/j.braindev.2015.10.001>
- Hirotsune, S.,** Fleck, M. W., Gambello, M. J., Bix, G. J., Chen, a, Clark, G. D., ... Wynshaw-Boris, a. (1998). Graded reduction of Pafah1b1 (Lis1) activity results in neuronal migration defects

and early embryonic lethality. *Nature Genetics*, 19(4), 333–339.
<https://doi.org/10.1038/1221>

Hodge, R. D., Bakken, T. E., Miller, J. A., Smith, K. A., Barkan, E. R., Graybuck, L. T., ... Lein, E. S. (2019). Conserved cell types with divergent features in human versus mouse cortex. *Nature*, 573(7772), 61–68. <https://doi.org/10.1038/s41586-019-1506-7>

Hu, H., Gan, J., & Jonas, P. (2014). Fast-spiking, parvalbumin+ GABAergic interneurons: From cellular design to microcircuit function. *Science*, 345(6196), 1255263–1255263.
<https://doi.org/10.1126/science.1255263>

Jinno, S., & Kosaka, T. (2002). Patterns of expression of calcium binding proteins and neuronal nitric oxide synthase in different populations of hippocampal GABAergic neurons in mice. *Journal of Comparative Neurology*, 449(1), 1–25. <https://doi.org/10.1002/cne.10251>

Jones, D. L., & Baraban, S. C. (2009). Inhibitory inputs to hippocampal interneurons are reorganized in Lis1 mutant mice. *Journal of Neurophysiology*, 102(2), 648–658.
<https://doi.org/10.1152/jn.00392.2009>

Kato, M., & Dobyns, W. B. (2003). Lissencephaly and the molecular basis of neuronal migration. *Human Molecular Genetics*, 12(REV. ISS. 1), 89–96. <https://doi.org/10.1093/hmg/ddg086>

Kohus, Z., Káli, S., Rovira-Esteban, L., Schlingloff, D., Papp, O., Freund, T. F., ... Gulyás, A. I. (2016). Properties and dynamics of inhibitory synaptic communication within the CA3 microcircuits of pyramidal cells and interneurons expressing parvalbumin or cholecystinin. *Journal of Physiology*, 594(13), 3745–3774.
<https://doi.org/10.1113/JP272231>

Kröcher, T., Röckle, I., Diederichs, U., Weinhold, B., Burkhardt, H., Yanagawa, Y., ... Hildebrandt, H. (2014). A crucial role for polysialic acid in developmental interneuron migration and the establishment of interneuron densities in the mouse prefrontal cortex. *Development (Cambridge)*, 141(15), 3022–3032. <https://doi.org/10.1242/dev.111773>

Lim, L., Mi, D., Llorca, A., & Marín, O. (2018). Development and Functional Diversification of Cortical Interneurons. *Neuron*. <https://doi.org/10.1016/j.neuron.2018.10.009>

Mahadevan, V., Mitra, A., Zhang, Y., Peltekian, A., Chittajallu, R., Esnault, C., ... McBain, C. J. (2020). NMDAR-mediated transcriptional control of gene expression in the specification of interneuron subtype identity. *BioRxiv*. <https://doi.org/10.1101/2020.06.10.144295>

McCormick, D. A., & Contreras, D. (2001). On the Cellular and Network Bases of Epileptic Seizures. *Annual Review of Physiology*, 63(1), 815–846.

- Mcmanus, M. F., Nasrallah, I. M., Pancoast, M. M., Wynshaw-boris, A., & Golden, J. A. (2004).** Lis1 Is Necessary for Normal Non-Radial Migration of Inhibitory Interneurons. *The American Journal of Pathology*, *165*(3), 775–784. [https://doi.org/10.1016/S0002-9440\(10\)63340-8](https://doi.org/10.1016/S0002-9440(10)63340-8)
- Menascu, S., Weinstock, A., Farooq, O., Hoffman, H., & Cortez, M. A. (2013).** EEG and neuroimaging correlations in children with lissencephaly. *Seizure*, *22*(3), 189–193. <https://doi.org/10.1016/j.seizure.2012.12.001>
- Miyoshi, G., & Fishell, G. (2010).** GABAergic interneuron lineages selectively sort into specific cortical layers during early postnatal development. *Cerebral Cortex*, *21*(4), 845–852. <https://doi.org/10.1093/cercor/bhq155>
- Mulle, C., Sailer, A., Swanson, G. T., Brana, C., O’Gorman, S., Bettler, B., & Heinemann, S. F. (2000).** Subunit composition of kainate receptors in hippocampal interneurons. *Neuron*, *28*(2), 475–484. [https://doi.org/10.1016/S0896-6273\(00\)00126-4](https://doi.org/10.1016/S0896-6273(00)00126-4)
- Muñoz-Manchado, A. B., Bengtsson Gonzales, C., Zeisel, A., Munguba, H., Bekkouche, B., Skene, N. G., ... Hjerling-Leffler, J. (2018).** Diversity of Interneurons in the Dorsal Striatum Revealed by Single-Cell RNA Sequencing and PatchSeq. *Cell Reports*, *24*(8), 2179–2190.e7. <https://doi.org/10.1016/j.celrep.2018.07.053>
- Otsu, Y., Donneger, F., Schwartz, E. J., & Poncer, J. C. (2020).** Cation–chloride cotransporters and the polarity of GABA signalling in mouse hippocampal parvalbumin interneurons. *Journal of Physiology*, *598*(10), 1865–1880. <https://doi.org/10.1113/JP279221>
- Panthi, S., & Leitch, B. (2019).** The impact of silencing feed-forward parvalbumin-expressing inhibitory interneurons in the cortico-thalamocortical network on seizure generation and behaviour. *Neurobiology of Disease*, *132*(August), 104610. <https://doi.org/10.1016/j.nbd.2019.104610>
- Paul, A., Crow, M., Raudales, R., He, M., Gillis, J., & Huang, Z. J. (2017).** Transcriptional Architecture of Synaptic Communication Delineates GABAergic Neuron Identity. *Cell*, *171*(3), 522–539.e20. <https://doi.org/10.1016/j.cell.2017.08.032>
- Paylor, R., Hirotsune, S., Gambello, M. J., Yuva-Paylor, L., Crawley, J. N., & Wynshaw-Boris, A. (1999).** Impaired Learning and Motor Behavior in Heterozygous Pafah1b1 (Lis1) Mutant Mice. *Learning & Memory*, *6*(5), 521–537. <https://doi.org/10.1101/lm.6.5.521>
- Pelkey, K. A., Chittajallu, R., Craig, M. T., Tricoire, L., Wester, J. C., & McBain, C. J. (2017).** Hippocampal gabaergic inhibitory interneurons. *Physiological Reviews*, *97*(4), 1619–1747. <https://doi.org/10.1152/physrev.00007.2017>

- Que, L., Lukacsovich, D., & Földy, C. (2020).** Transcriptomic homogeneity and an age-dependent onset of hemoglobin expression characterize morphological PV types. *BioRxiv*.
<https://doi.org/10.1101/2020.01.21.913103>
- Rudy, B., & McBain, C. J. (2001).** Kv3 channels: Voltage-gated K⁺ channels designed for high-frequency repetitive firing. *Trends in Neurosciences*, *24*(9), 517–526.
[https://doi.org/10.1016/S0166-2236\(00\)01892-0](https://doi.org/10.1016/S0166-2236(00)01892-0)
- Saunders, A., Macosko, E. Z., Wysoker, A., Goldman, M., Krienen, F. M., de Rivera, H., ... McCarroll, S. A. (2018).** Molecular Diversity and Specializations among the Cells of the Adult Mouse Brain. *Cell*, *174*(4), 1015–1030.e16. <https://doi.org/10.1016/j.cell.2018.07.028>
- Shen, J., Wang, D., Wang, X., Gupta, S., Ayloo, B., Wu, S., ... Ge, S. (2019).** Neurovascular Coupling in the Dentate Gyrus Regulates Adult Hippocampal Neurogenesis. *Neuron*, *103*(5), 878–890.e3. <https://doi.org/10.1016/j.neuron.2019.05.045>
- Steinecke, A., Gampe, C., Zimmer, G., Rudolph, J., & Bolz, J. (2014).** EphA/ephrin A reverse signaling promotes the migration of cortical interneurons from the medial ganglionic eminence. *Development (Cambridge)*, *141*(2), 460–471.
<https://doi.org/10.1242/dev.101691>
- Stuart, T., Butler, A., Hoffman, P., Hafemeister, C., Papalexi, E., Mauck, W. M., ... Satija, R. (2019).** Comprehensive Integration of Single-Cell Data. *Cell*, *177*(7), 1888–1902.e21.
<https://doi.org/10.1016/j.cell.2019.05.031>
- Sudhakar, S. K., Choi, T. J., & Ahmed, O. J. (2019).** Biophysical Modeling Suggests Optimal Drug Combinations for Improving the Efficacy of GABA Agonists after Traumatic Brain Injuries. *Journal of Neurotrauma*, *36*(10), 1632–1645. <https://doi.org/10.1089/neu.2018.6065>
- Tasic, B., Menon, V., Nguyen, T. N., Kim, T. K., Jarsky, T., Yao, Z., ... Zeng, H. (2016).** Adult mouse cortical cell taxonomy revealed by single cell transcriptomics. *Nature Neuroscience*, *19*(2), 335–346. <https://doi.org/10.1038/nn.4216>
- Tasic, B., Yao, Z., Graybuck, L. T., Smith, K. A., Nguyen, T. N., Bertagnolli, D., ... Zeng, H. (2018).** Shared and distinct transcriptomic cell types across neocortical areas. *Nature*, *563*(7729), 72–78. <https://doi.org/10.1038/s41586-018-0654-5>
- Tissir, F., & Goffinet, A. M. (2003).** Reelin and brain development. *Nature Reviews Neuroscience*, *4*(6), 496–505. <https://doi.org/10.1038/nrn1113>
- Tran, T. S., Kolodkin, A. L., & Bharadwaj, R. (2007).** Semaphorin regulation of cellular morphology. *Annual Review of Cell and Developmental Biology*, *23*, 263–292.
<https://doi.org/10.1146/annurev.cellbio.22.010605.093554>

- Traynelis, S. F., & Dingledine, R. (1988).** Potassium-induced spontaneous electrographic seizures in the rat hippocampal slice. *Journal of Neurophysiology*, *59*(1), 259–276. <https://doi.org/10.1152/jn.1988.59.1.259>
- Vaden, R. J., Gonzalez, J. C., Tsai, M. C., Niver, A. J., Fusilier, A. R., Griffith, C. M., ... Overstreet-Wadiche, L. (2020).** Parvalbumin interneurons provide spillover to newborn and mature dentate granule cells. *eLife*, *9*, 1–23. <https://doi.org/10.7554/eLife.54125>
- Vallee, R. B., & Tsai, J. W. (2006).** The cellular roles of the lissencephaly gene LIS1, and what they tell us about brain development. *Genes and Development*, *20*(11), 1384–1393. <https://doi.org/10.1101/gad.1417206>
- van den Berghe, V., Stappers, E., Vandesande, B., Dimidschstein, J., Kroes, R., Francis, A., ... Seuntjens, E. (2013).** Directed Migration of Cortical Interneurons Depends on the Cell-Autonomous Action of Sip1. *Neuron*, *77*(1), 70–82. <https://doi.org/10.1016/j.neuron.2012.11.009>
- Wester, J. C., Mahadevan, V., Rhodes, C. T., Calvigioni, D., Venkatesh, S., Maric, D., ... McBain, C. J. (2019).** Neocortical Projection Neurons Instruct Inhibitory Interneuron Circuit Development in a Lineage-Dependent Manner. *Neuron*, *102*(5), 960-975.e6. <https://doi.org/10.1016/j.neuron.2019.03.036>
- Wyeth, M. S., Pelkey, K. A., Yuan, X., Vargish, G., Johnston, A. D., Hunt, S., ... McBain, C. J. (2017).** Neto Auxiliary Subunits Regulate Interneuron Somatodendritic and Presynaptic Kainate Receptors to Control Network Inhibition. *Cell Reports*, *20*(9), 2156–2168. <https://doi.org/10.1016/j.celrep.2017.08.017>
- Wynshaw-Boris, A., & Gambello, M. J. (2001).** LIS1 and dynein motor function in neuronal migration and development. *Genes and Development*, *15*(6), 639–651. <https://doi.org/10.1101/gad.886801>
- Yao, Z., Nguyen, T. N., Van Velthoven, C. T. J., Goldy, J., Sedeno-Cortes, A. E., Baftizadeh, F., ... Zeng, H. (2020).** A taxonomy of transcriptomic cell types across the isocortex and hippocampal formation. *BioRxiv*.
- Ye, Z., Mostajo-Radji, M. A., Brown, J. R., Rouaux, C., Tomassy, G. S., Hensch, T. K., & Arlotta, P. (2015).** Instructing Perisomatic Inhibition by Direct Lineage Reprogramming of Neocortical Projection Neurons. *Neuron*, *88*(3), 475–483. <https://doi.org/10.1016/j.neuron.2015.10.006>
- Yokota, Y., Ghashghaei, H. T., Han, C., Watson, H., Campbell, K. J., & Anton, E. S. (2007).** Radial glial dependent and independent dynamics of interneuronal migration in the developing cerebral cortex. *PLoS ONE*, *2*(8). <https://doi.org/10.1371/journal.pone.0000794>

Figure 2 -- Supplement 1

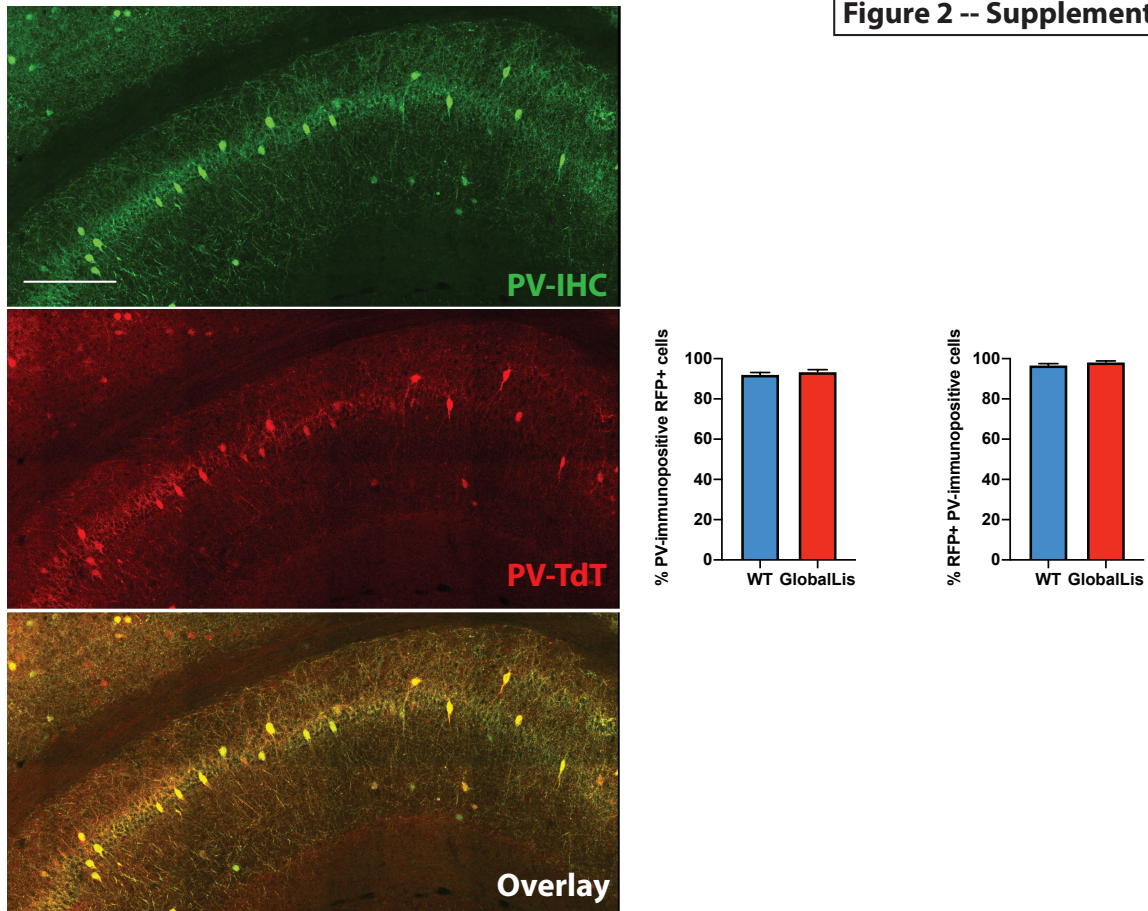


Figure 2 – figure supplement 1. PV-TdTomato/PV-IHC colocalization. GlobalLis mutant hippocampus. Top image displays PV-IHC, middle displays PV-TdTomato, bottom displays superimposition, in a representative GlobalLis hippocampus. There is high level of colocalization: most TdTomato+ cells were PV-IHC+ and most PV-IHC+ cells were PV-TdTomato+. Counting was performed on 2-4 hippocampal sections from each animal (n = 3-6 animals per genotype). Scale bar = 250 μ m.

Figure 2 -- Supplement 2

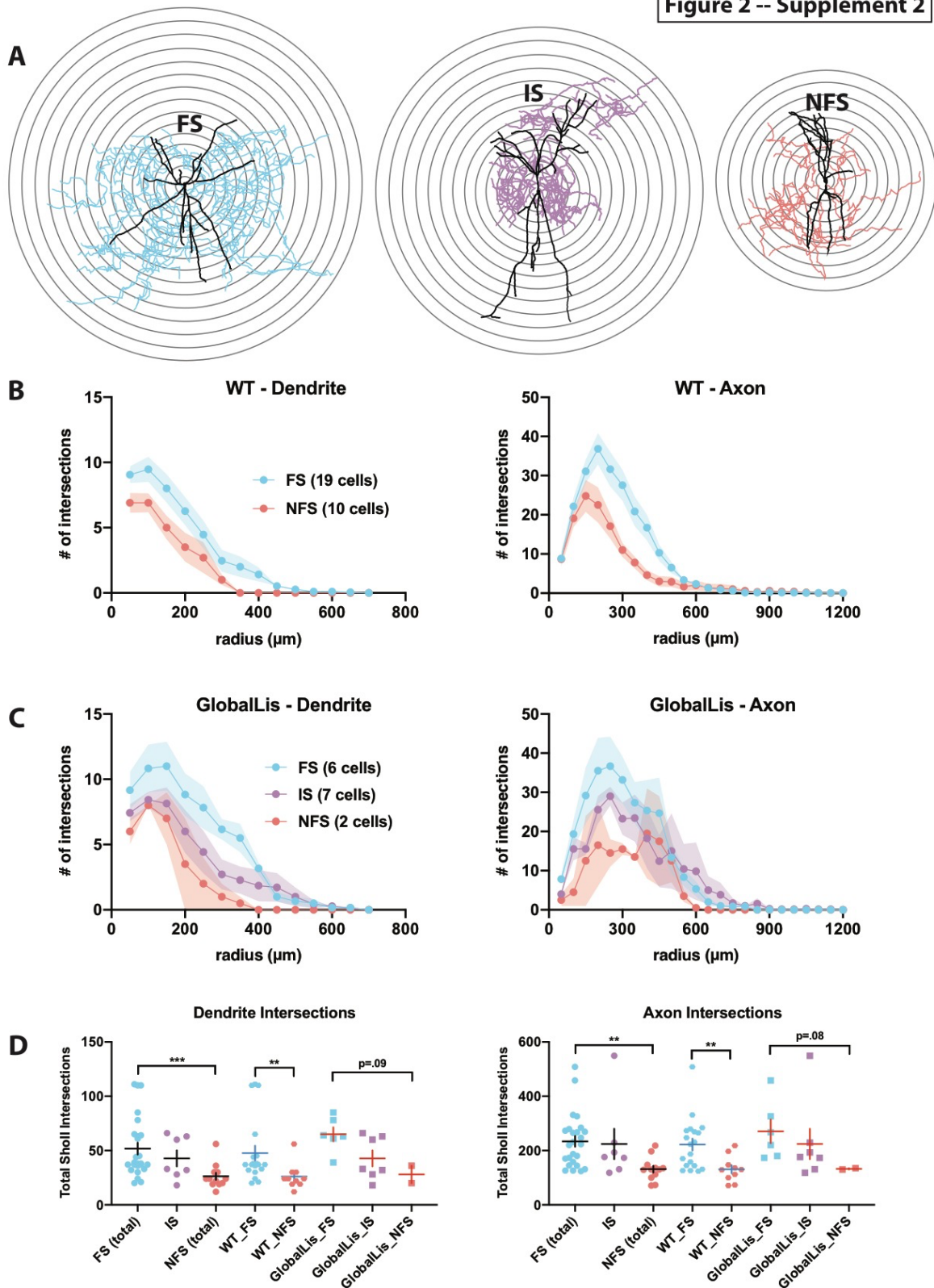


Figure 2—figure supplement 2. Morphological analysis of PV+INT physiological subtypes. **A** Reconstructions of FS (left), IS (middle) and NFS (right) PV+INTs. Concentric circles (superimposed in black) with a radius interval of 50 μm were used for Sholl analysis. **B** Plots of Sholl intersections in WT FS/NFS cells at 50 μm intervals for dendrites

(left) and axon (right). **C** Plots of Sholl intersections in GlobalLis FS/IS/NFS cells at 50 μm intervals for dendrites (left) and axon (right). **D** Quantification of the total number of Sholl intersections for FS/IS/NFS cells independent of genotype (“total”) and by genotype (WT or GlobalLis) for dendrites (left) and axons (right). For statistical analysis * $p < 0.05$, ** $p < 0.01$, *** $p < 0.001$.

Figure 3 -- Supplement 1

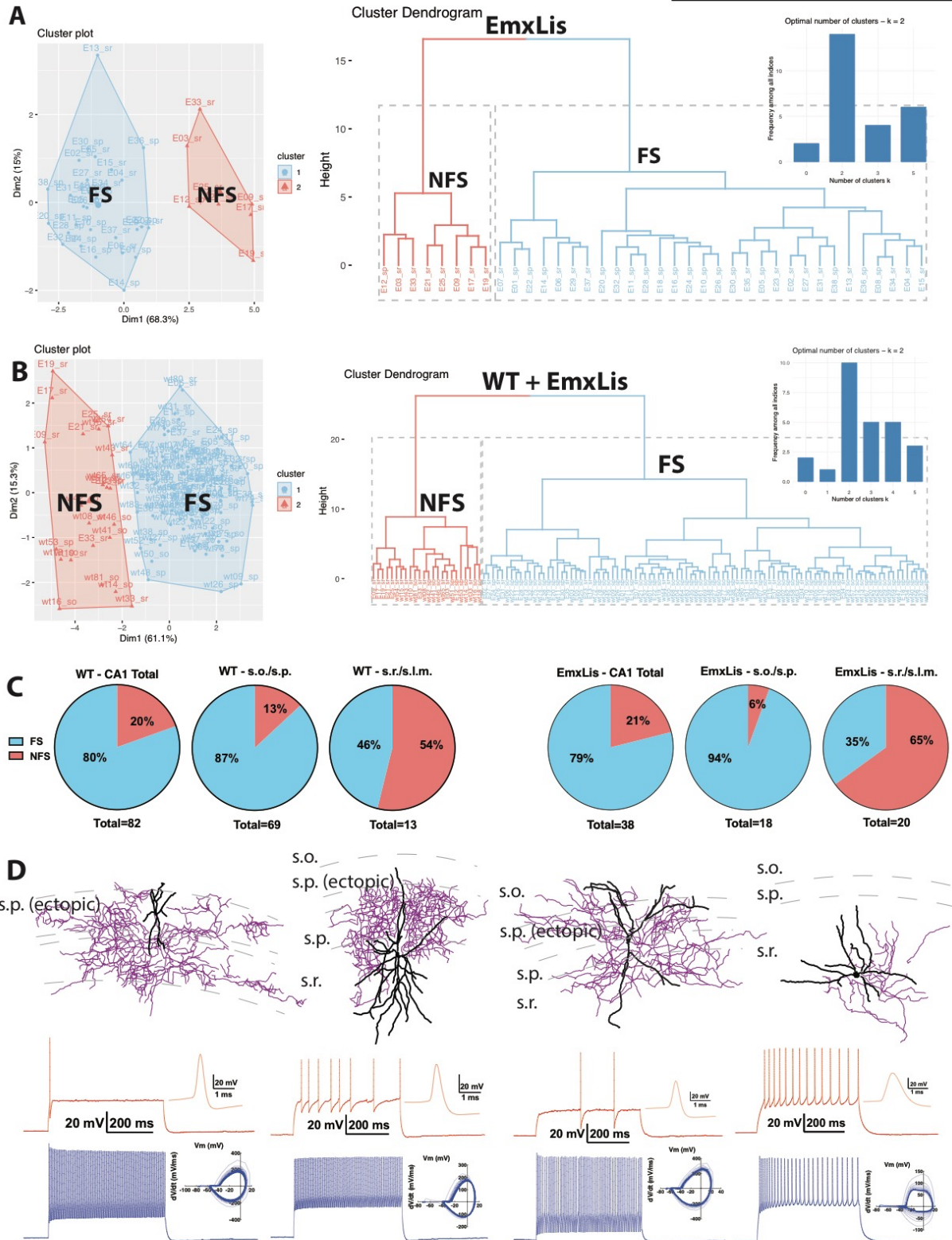


Figure 3—figure supplement 1. Cluster analysis and morphophysiology of EmxLis PV+INTs. A Cluster plot (left) and dendrogram (right) of 38 EmxLis PV+INTs. The dendrogram inset indicates 2 optimal clusters which correspond to FS and NFS cells. **B** Due to similar sorting, WT and EmxLis datasets were analyzed together, which resulted in

identical classification of every FS/NFS cell. **C** Percentages of FS/NFS cells in CA1 and each sublayer. For reference, the WT distributions (left) are repeated alongside the EmxLis distributions (right). **D** Examples of EmxLis PV+INTs reconstructed cells (dendrite in black, axon in blue) and firing traces on bottom (as described in Fig. 2). Cell types from left to right: FS basket cell, FS basket cell, FS bistratified cell, NFS radiatum-targeting cell.

Figure 4 -- Supplement 1

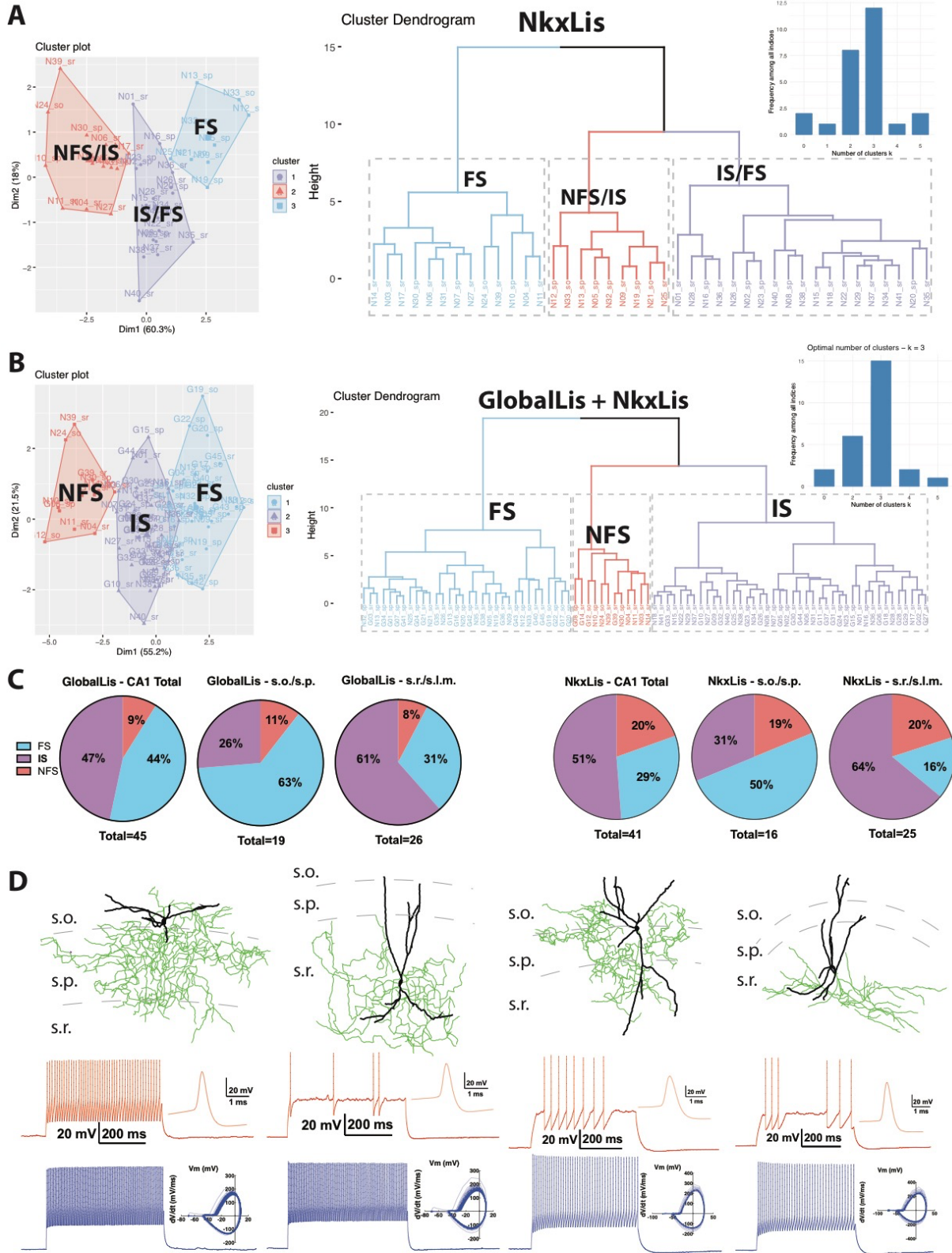


Figure 4—figure supplement 1. *Cluster analysis and morphophysiology of NkxLis PV+INTs.* **A** Cluster plot (left) and dendrogram (right) of 41 NkxLis PV+INTs. The dendrogram inset indicates 3 optimal clusters which correspond to FS and NFS cells. **B** Due to similar sorting, as well as the obvious misclassification some cell types, NkxLis and GlobalLis datasets were analyzed together, which resulted in more reliable classification cell types. **C** Percentages of FS/IS/NFS cells in CA1 and each sublayer. For reference, the GlobalLis distributions (left) are repeated alongside the NkxLis distributions (right). **D** Examples of NkxLis PV+INTs reconstructed cells (dendrite in black, axon in blue) and firing traces on bottom (as described in Fig. 2). Physiological cell types from left to right: FS, FS, IS, NFS.

Figure 4 -- Supplement 2

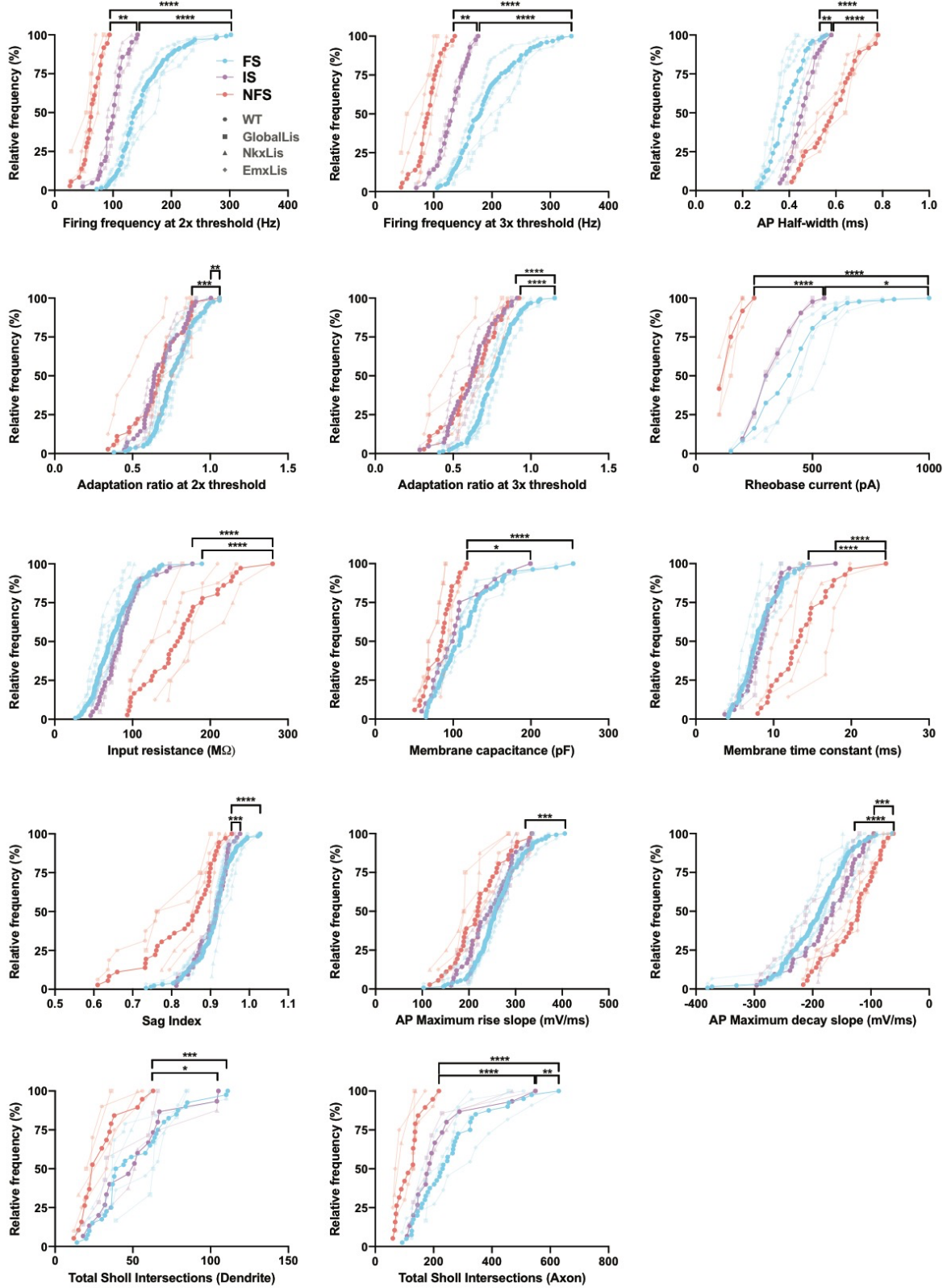


Figure 4—figure supplement 2. Membrane, firing, and morphological properties of PV+INT physiological subtypes. Frequency distributions of physiological and morphological properties PV+INTs. FS cells are shown in blue, IS cells in purple, NFS cells in pink. The full color circles connecting lines display the average of all genotypes for each physiological subtype. The faded shapes/lines represent distributions for WT (hexagons), Globallis (squares), NkxLis (triangles), and EmxLis (diamonds). Note that with the exception of AP half-width, there were no significant differences between genotypes. Almost every property shown here had significant differences between physiological subtype, independent of genotype. See also Table 1. For statistical analysis * $p < 0.05$, ** $p < 0.01$, *** $p < 0.001$, **** $p < 0.0001$.

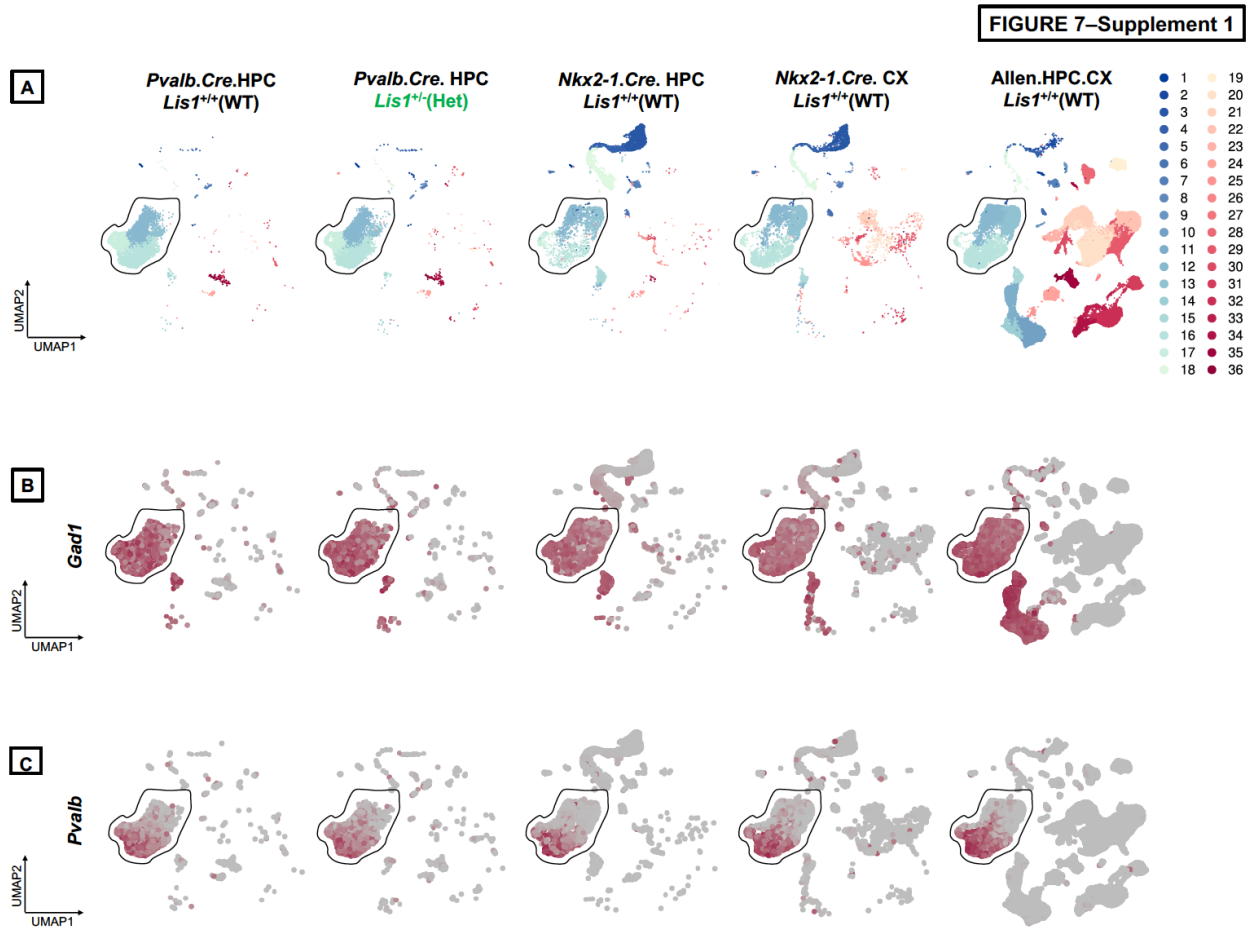


Figure 7— figure supplement 1. Integrated analyses of single-cell/nucleus transcriptomes from PV+INTs from *Lis1^{+/+}*, *Lis1^{+/-}*, and reference datasets. **A** UMAP plots of the PV+INTs from *Lis1^{+/+}*, *Lis1^{+/-}*, cortical and hippocampal MGE-derived interneurons and pan-GABAergic Allen Institute datasets indicating robust alignments of the PV+INT clusters. UMAP plots representing the expression of **B**, *Gad1* and **C**, *Pvalb* across all datasets.

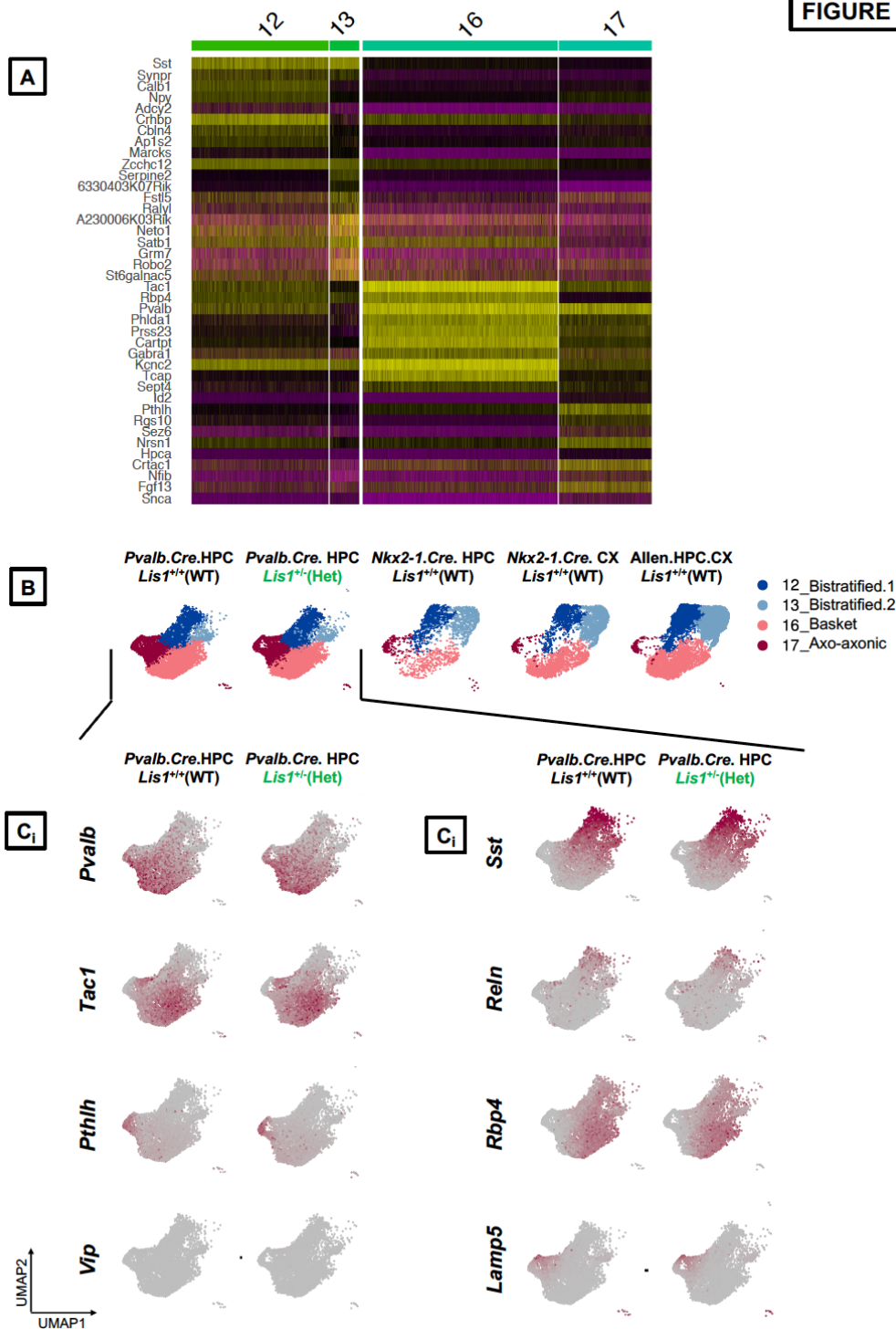


Figure 7—figure supplement 2. Annotation of PV+INT subtypes based on discrete marker gene expressions. **A** Single cell heatmap showing scaled expression values for the top 10 transcriptomic markers in each of the PV+INTs clusters across *Lis1*^{+/+}, *Lis1*^{+/-}, and reference datasets. **B** UMAP plots depicting the bistratified, axo-axonic and fast-spiking clusters across all datasets. **C** Merged UMAP plots representing the expression of top transcriptomic markers across the PV+INT subtypes across all datasets.

Chapter 4.

Discussion

4.0 Overview

This project has increased understanding of hippocampal lamination and inhibitory circuit development. I identified uncharacterized morphophysiological subtypes of WT PV+INTs and determined the consequences of cell-autonomous and non-cell-autonomous heterozygous mutations of *LIS1* on PV+INT development and function. An increased propensity for depolarization block in subtypes of GlobalLis PV+INTs is expected to interfere with their ability to control epileptic seizures. In short, disrupted developmental programs due to *LIS1* heterozygous loss within PV+INTs, rather than disrupted migration/lamination itself, may contribute to the spontaneous seizures observed in Type I lissencephaly.

4.1 The Type I lissencephaly mouse model as a proxy for the human condition

This mouse model of Type I lissencephaly captured several important aspects of the human disease including motor impairments, enhanced excitation and spontaneous seizures (Paylor et al. 1999; Fleck et al. 2000; Greenwood et al., 2009; Saillour et al., 2009). Although mouse brains lack gyrfication, there are identifiable disruptions to brain lamination in the *LIS1* mutant that reflect the human condition: cortical layers are poorly organized and boundaries between layers are blurred, in hippocampus stratum pyramidale fractures into multiple pyramidal cell layers, and cerebellar organization is disrupted (Hirotsune et al., 1998; Fleck et al., 2000; Di Donato et al.,

2017). This combination of similar morphological disruptions and neurological impairments make the mouse model of lissencephaly a powerful tool for studying Type I lissencephaly.

Recent research confirms the validity of using animal models to better understand human physiology. Work on human brain tissue using snRNAseq has demonstrated conservation of cell types between human and mice (Hodge et al., 2019). However, differences were noted in cellular features such as morphology, laminar distribution and gene expression (Hodge et al., 2019). Fortunately, recent work in human brain tissue has demonstrated that PV+INTs can be targeted and manipulated using viruses, and human FS cells have similar firing properties to mouse FS cells (Vormstein-Schneider et al., 2020). Taken together, we can reasonably assume that findings in this study should be translatable across species.

4.2 Impact of *LIS1* heterozygous loss on hippocampal lamination and connectivity

LIS1 heterozygous loss has a dramatic effect on the migration and cellular positioning of both excitatory pyramidal cells and inhibitory interneurons (Fleck et al., 2000; Jones & Baraban, 2009). In chapter 2, we identify that the majority of CA1 late-born, calbindin-expressing (CB+) PCs are mispositioned in the GlobalLis hippocampus. The majority of CA1 mutant CB+PCs cells occupy the deep/ectopic layers of stratum pyramidale rather than the superficial positions of WT CB+PCs. The later birthdate of CB+PCs may explain their ectopic positioning: late arriving CB+PCs deficient in *Lis1* protein may not have the ability to penetrate the already formed dense layer of CB-PCs.

Radial migration of GlobalLis PV+ and CCK+ INTs was disrupted such that there was an increased percentage of these mutant cells present in superficial layers (stratum radiatum and

stratum lacunosum-moleculare) with a corresponding reduction in deeper layers. This was correlated with a disrupted preference for CCK+INT perisomatic targeting of CB+PCs in the GlobalLis mutant. Furthermore, complex PCs (morphological correlate of CB expression) that were in ectopic positions had reduced levels of CCK+INT input (as demonstrated by the conotoxin experiments). This is perhaps unsurprising, considering the increased distance between ectopic CB+PCs and mispositioned CCK+INTs. The wiring cost may be too great to connect to the most ectopic of CB+PC somata.

In chapter 3, I utilized cell type-specific mutations to selectively remove one copy of *LIS1* from PCs (EmxLis) or from medial ganglionic eminence-derived INTs (NkxLis). The overall CA1 structure in the EmxLis mutation resembled the GlobalLis CA1 (disrupted formation of PC layer), while the NkxLis mutation was indistinguishable from WT. In contrast, disruption of PV+INT radial migration was observed in both the EmxLis and NkxLis genotypes. In conclusion, in order to achieve successful radial migration, PV+INTs require both cell-autonomous *LIS1*-dependent processes, and non-cell-autonomous interactions with pyramidal neurons.

4.3 Characterization of PV+IN subtypes and emergence of intermediate spiking cells

In order to fully appreciate the differences to subtypes of neurons caused by genetic mutations, it is essential to first comprehensively characterize the WT population. I found that 80-85% of WT PV+INs were fast-spiking (FS) cells and the remaining 15-20% were non-fast-spiking (NFS) cells. Compared to FS cells, NFS cells had lower rheobases, higher input resistances, longer action potential half-widths, and lower firing rates. NFS cells consisted of two morphological subtypes: the commonly identified basket cells and a newly identified subtype I have labeled “radiatum-

targeting” PV+ cells, as their axons are confined to stratum radiatum. FS cells consisted of basket cells, axo-axonic cells, bistratified cells and radiatum-targeting cells.

In the GlobalLis mutant, clear morphological labels are difficult to assign to recovered PV+INs. Cellular morphology was radially disrupted, with axon patterns resembling combinations of the common morphological subtypes as well as branching into new patterns that have no resemblance to any WT PV+INT, including the newly identified radiatum-targeting cells. Despite the morphological disruption to PV+INTs, clusters of FS and NFS cells with essentially unaltered electrical properties were detected in the GlobalLis mutant. An additional cluster of PV+ cells emerged in this dataset. As the membrane and firing properties of the emergent cluster fell between values of both FS and NFS cells, I refer to this population as “intermediate-spiking” (IS) cells.

Although pyramidal cell layer organization and radial migration of PV+INTs was disrupted in the EmxLis mutant, PV+ cells were able to develop into normal morphophysiological subtypes. EmxLis PV+INs cleanly parsed into two clusters: FS and NFS cells. Surprisingly, neither the fractured banding of PCs or ectopic positioning of INTs interfered with the ability to form cells identifiable as basket, axo-axonic, bistratified, or radiatum-targeting cells. There were some differences in morphology relative to WT cells, such as basket cells with somata in stratum radiatum projecting axon into heterotopic pyramidal cell bands. Similar to GlobalLis PV+INTs, the NkxLis hippocampus was composed of FS, IS and NFS cells. Despite the normal development of the pyramidal cell layer, NkxLis PV+INTs experienced morphological disruptions, again rendering classification dubious.

Physiological properties of FS cells were largely unchanged in all mutant genotypes. The only observed difference was wider action potential half-widths in WT cells than GlobalLis, EmxLis and NkxLis cells. Although we did not detect IS cells in WT and EmxLis genotypes, GlobalLis and NkxLis IS cells had identical intrinsic properties. Similarly, NFS cells of all genotypes had indistinguishable physiological properties.

The WT hippocampus PV+INT population is composed of 80% FS and 20% NFS cells. This was also found to be the case in the EmxLis hippocampus (81% FS, 19% NFS), despite increased density of PV+INTs in stratum radiatum. Hence, ectopic positioning of PV+INTs and overall disorganization of pyramidal cell layers does not greatly disrupt overall morphophysiological development of PV+INTs. Contrastingly, heterozygous removal of *LIS1* within PV+INTs in the GlobalLis and NkxLis genotypes impacts developmental programs within these cells, disrupting morphology and causing the emergence of IS cells. In these genotypes, FS cells now constitute only 29-44% of PV+INTs and IS/NFS cells make up 56-71%.

4.4 Synaptic transmission, depolarization block and implications for network dynamics and epileptiform activity

In the WT hippocampus, the presynaptic PV+INT subtype determines unitary synaptic transmission dynamics. In general, FS cells had higher connectivity rates and made stronger connections with pyramidal cells (PCs) than did NFS cells. Further differences are found when considering morphological as well as physiological subtype, with FS basket cells making much stronger (higher potency/amplitude), and more reliable synapses (lower failure rates across the

25-pulse train) than connections from both FS bistratified cells and NFS basket cells. In addition, transmission latency was longer in NFS-PC connections.

As morphological disruptions eliminated the ability to parse GlobalLis PV+INTs into clear morphological subtypes, we analyzed by physiological subtype and found that connectivity rates and unitary transmission properties of GlobalLis FS cells were not significantly different from combined (basket and bistratified cell) WT FS-PC cell connections. GlobalLis IS cells had transmission properties that resembled WT NFS-PC synapses: lower amplitudes, higher failure rates, and longer latencies relative to FS cell outputs. No GlobalLis NFS-PC connections were obtained.

The reduction in number of FS cells and the emergence of IS cells in the GlobalLis mutant, with their lower firing rates and longer delay/lower potency/less reliable synapses, likely pushes hippocampal networks to the edge of control. This may be a major contributor to the hyperexcitability and lower-seizure threshold observed in these mice. Furthermore, IS and NFS cells are less able to control runaway excitation and epileptiform activity due to their propensity for depolarizing block. While many FS cells can continue to fire at extremely high frequencies even after large injections of suprathreshold depolarizing current and many retain their ability to fire in the High [K⁺] model of epilepsy (Traynelis & Dingledine, 1988), IS and NFS cells readily enter depolarization block, presumably eroding their ability to control electrographic activity and allowing seizures to propagate. It should be noted that that FS cell function in other models of epilepsy and in long-term epilepsy patients can become compromised, rendering these cells susceptible to depolarization block (Karlócai et al., 2014; Ahmed et al., 2015).

4.5. Outstanding questions and future directions

LIS1^{+/-} haploinsufficiency is one type of many neuronal migration/cortical malformation disorders. Mutations to other genes coding cytoskeletal elements such as microtubule-related proteins actin components and binding proteins, extracellular matrix proteins, and others disrupt neuronal migration, resulting in lissencephaly spectrum disorders and epilepsy (Stouffer et al., 2015). Although epilepsy is a common feature of cortical malformation disorders, lamination is impacted differently in the animal models, depending on the mutated genes.

Mutations to *DCX* (a microtubule stabilizing factor) show many similarities to the GlobalLis mouse; however, CA3 pyramidal cells are preferentially affected in the *DCX* mutant (Stouffer et al., 2015). Mutations to the extracellular matrix protein *RELN* cause similar effects as *LIS1* heterozygous mutation: mislamination of cortex, hippocampus and cerebellum (Chevassus-au-Louis et al., 1999). A similar pattern is also found in *CDK5* (a master regulator similar to *LIS1*) mutant mice, although this mutation has not been identified in human populations (Stouffer et al., 2015). It would be interesting to examine PV+INT development in other migration disorders to discover if IS cells emerge in these conditions.

In the snRNAseq experiments, no additional clusters of PV+INTs were detected. We can conclude that IS cells do not represent a transcriptionally distinct population of PV+INTs, at least from our analysis of PV+INTs at postnatal day 20. Despite this, transcriptomic changes were seen in all PV+INT clusters. It is possible that transcriptional differences are more drastic at earlier timepoints. Future experiments could examine transcriptomic profiles of WT and GlobalLis PV+INTs at earlier postnatal days to determine developmental transcription trajectories. In addition, patch-seq could be utilized to definitively assign physiological subtype to sequenced

cells and identify molecular markers for IS cells. A recent study utilized this combinatorial approach to investigate the diversity of striatal interneurons and found that PV+INTs are part of a gradient of PTHLH-expressing cells and have a continuum of electrophysiological properties ranging from fast-spiking to “fast-spiking-like” (Munoz-Manchado et al., 2018).

Although IS cells emerge in the *Globalis* and *Nkx1is* mutants, physiologically typical FS and NFS cells also develop in these mice. A full understanding as to why some PV+INTs develop into FS cells while others become IS cells remains elusive. One factor that may influence PV+INT development is the embryonic birth date and the level of excitatory and/or inhibitory drive (Donato et al., 2015). Indeed, analysis of spontaneous excitatory post synaptic currents (sEPSCs) in PV+INTs reveals that FS cells receive a much higher level of spontaneous excitatory input than both IS and NFS cells (Figure 1A). This pattern was present in all genotypes (Figure 1B). It is a possibility that PV precursors destined to become NFS cells require a low level of excitatory input to drive their development, while FS cells require a high level of spontaneous excitatory drive. A former study found that PV+INTs in visual cortex are composed of various subclusters of cells, and the cluster with the lowest sEPSC frequencies had low firing rates, high input resistances, low rheobases, and wide action potential half-widths, reminiscent of PV+NFS cells (Helm et al., 2013). Another study found that overexpressing synapse-associated protein 97 (SAP97) in PV+INTs increases sEPSC frequency, with a corresponding increase in firing rate and decrease in AP half-width (Akgul & Wollmuth, 2013). It is possible that IS cells are PV precursors which failed to develop into FS cells due to insufficient excitatory recruitment.

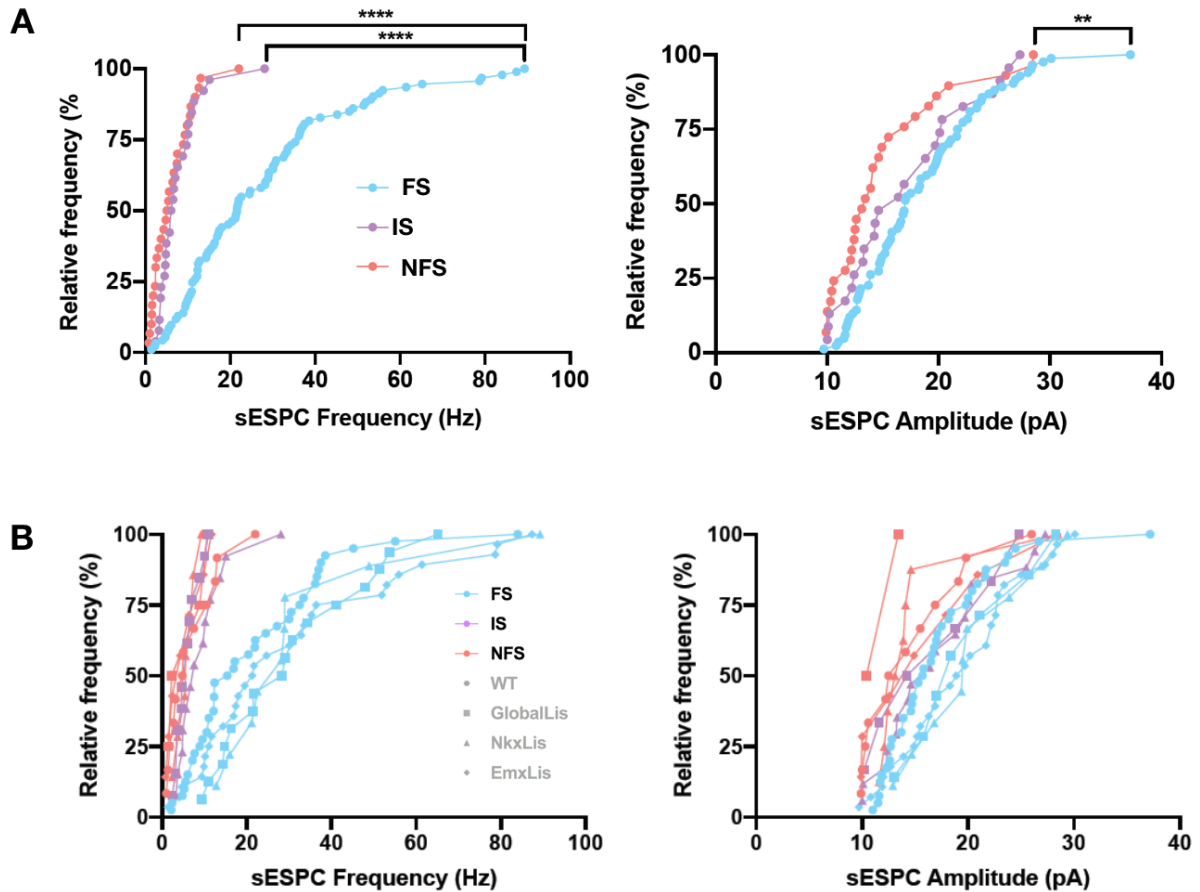


Figure 1. Spontaneous excitatory inputs to PV+INTs. **A** Frequency distribution of spontaneous excitatory post synaptic current (sEPSC) frequency and amplitude for PV+INT physiological subtypes, independent of genotype. **B** Frequency distributions of sEPSC frequency and amplitude by genotype and physiological subtype.

Another possibility considers that cells produce variable amounts of proteins and protein levels change in response to intracellular and extracellular signals (Dorrbaum et al. 2018). Cells that either synthesize lower amounts of LIS1 protein and/or have more disruptions to LIS1 turnover due to internal and external environmental interactions are expected to have more difficulty with cellular migration and protein trafficking and could consequently develop into IS instead of FS cells. Additionally, or alternatively, the different environments encountered

migrating early-born or late-born PV+INTs could interact with *LIS1* intracellular signaling pathways to differentially affect development of these two populations of cells. As the present study did not investigate the role of cellular birth-dating on PV+INT development, future experiments could examine this using BrdU fate mapping in combination with immunohistochemistry and with other techniques that allow labeling of isochronic cells for electrophysiological recording (Govindan et al., 2018).

The findings in this study imply that intrinsic changes to subtypes of PV+INTs, rather than ectopic positioning is a major contributor to epileptogenesis. A prediction from this is that *NkxLis* mice should have a lower threshold for seizures compare to WT and *EmxLis* mice. Future experiments could test this hypothesis *in vivo* by monitoring for spontaneous seizures and inducing them with hyperthermia and *in vitro* with the High [K⁺] model.

4.6 Conclusion

The epilepsy commonly observed in cortical malformation disorders such as lissencephaly has been considered to be a result of the disrupted neuronal migration/lamination (Chevassus-Au-Louis et al., 1999; Barkovich et al., 2015). While we do see evidence of dysfunctional targeting of ectopic CB+PCs by CCK+INTs, this is unlikely to be the source of epileptic seizures, as these ectopic PCs were still innervated by other inhibitory interneurons such as PV+INTs. The *EmxLis* experiments demonstrate that disrupted radial migration and ectopic positioning of PV+INTs do not impact their morphophysiological development. In contrast, the *NkxLis* experiments illustrated that heterozygous removal of *LIS1* within interneurons disrupts intrinsic developmental programs of PV+INTs and causes the emergence of IS cells. Distinct intrinsic

changes to subtypes of neurons rather than dysfunctional targeting or global inefficiency of synapses should be considered among the causes of epilepsy in lissencephaly, and perhaps in other migration disorders. Reprogramming of IS cells to FS cells may be a feasible goal for treating epileptic seizures in lissencephaly patients.

4.7 References

- Ahmed, O. J., Kramer, M. A., Truccolo, W., Naftulin, J. S., Potter, N. S., Eskandar, E. N., ... Cash, S. S. (2014).** Inhibitory single neuron control of seizures and epileptic traveling waves in humans. *BMC Neuroscience, 15*(Suppl 1), F3. <https://doi.org/10.1186/1471-2202-15-S1-F3>
- Akgul, G., & Wollmuth, L. P. (2013).** Synapse-associated protein 97 regulates the membrane properties of fast-spiking parvalbumin interneurons in the visual cortex. *Journal of Neuroscience, 33*(31), 12739–12750. <https://doi.org/10.1523/JNEUROSCI.0040-13.2013>
- Barkovich, A. J., Dobyns, W. B., & Guerrini, R. (2015).** Malformations of Cortical Development and Epilepsy. *Cold Spring Harbor Perspectives in Medicine, 5*, 1–23. <https://doi.org/10.1101/cshperspect.a022392>
- Chevassus-Au-Louis, N., Baraban, S. C., Gaiarsa, J. L., & Ben-Ari, Y. (1999).** Cortical malformations and epilepsy: New insights from animal models. *Epilepsia, 40*(7), 811–821. <https://doi.org/10.1111/j.1528-1157.1999.tb00786.x>
- Di Donato, N., Chiari, S., Mirzaa, G. M., Aldinger, K., Parrini, E., Olds, C., ... Dobyns, W. B. (2017).** Lissencephaly: Expanded imaging and clinical classification. *American Journal of Medical Genetics, Part A, 173*(6), 1473–1488. <https://doi.org/10.1002/ajmg.a.38245>
- Donato, F., Chowdhury, A., Lahr, M., & Caroni, P. (2015).** Early- and Late-Born Parvalbumin Basket Cell Subpopulations Exhibiting Distinct Regulation and Roles in Learning. *Neuron, 85*(4), 770–786. <https://doi.org/10.1016/j.neuron.2015.01.011>
- Dörrbaum, A. R., Kochen, L., Langer, J. D., & Schuman, E. M. (2018).** Local and global influences on protein turnover in neurons and glia. *ELife, 7*, 1–24. <https://doi.org/10.7554/eLife.34202>
- Fleck, M. W., Hirotsune, S., Gambello, M. J., Phillips-Tansey, E., Soares, G., Mervis, R. F., ... McBain, C. J. (2000).** Hippocampal abnormalities and enhanced excitability in a murine

model of human lissencephaly. *Journal of Neuroscience*, 20(7), 2439–2450.
<https://doi.org/10729324>

Govindan, S., Oberst, P., & Jabaudon, D. (2018). In vivo pulse labeling of isochronic cohorts of cells in the central nervous system using FlashTag. *Nature Protocols*, 13(10), 2297–2311.
<https://doi.org/10.1038/s41596-018-0038-1>

Greenwood, J. S. F., Wang, Y., Estrada, R. C., Ackerman, L., Ohara, P. T., & Baraban, S. C. (2009). Seizures, enhanced excitation, and increased vesicle number in Lis1 mutant mice. *Annals of Neurology*, 66(5), 644–653. <https://doi.org/10.1002/ana.21775>

Helm, J., Akgul, G., & Wollmuth, L. P. (2012). Subgroups of parvalbumin-expressing interneurons in layers 2/3 of the visual cortex. *Journal of Neurophysiology*, 109(6), 1600–1613. <https://doi.org/10.1152/jn.00782.2012>

Hirotsune, S., Fleck, M. W., Gambello, M. J., Bix, G. J., Chen, a, Clark, G. D., ... Wynshaw-Boris, a. (1998). Graded reduction of Pafah1b1 (Lis1) activity results in neuronal migration defects and early embryonic lethality. *Nature Genetics*, 19(4), 333–339.
<https://doi.org/10.1038/1221>

Hodge, R. D., Bakken, T. E., Miller, J. A., Smith, K. A., Barkan, E. R., Graybuck, L. T., ... Lein, E. S. (2019). Conserved cell types with divergent features in human versus mouse cortex. *Nature*, 573(7772), 61–68. <https://doi.org/10.1038/s41586-019-1506-7>

Jones, D. L., & Baraban, S. C. (2009). Inhibitory inputs to hippocampal interneurons are reorganized in Lis1 mutant mice. *Journal of Neurophysiology*, 102(2), 648–658.
<https://doi.org/10.1152/jn.00392.2009>

Karlócai, M. R., Kohus, Z., Káli, S., Ulbert, I., Szabó, G., Máté, Z., ... Gulyás, A. I. (2014). Physiological sharp wave-ripples and interictal events in vitro: What's the difference? *Brain*, 137(2), 463–485. <https://doi.org/10.1093/brain/awt348>

Muñoz-Manchado, A. B., Bengtsson Gonzales, C., Zeisel, A., Munguba, H., Bekkouche, B., Skene, N. G., ... Hjerling-Leffler, J. (2018). Diversity of Interneurons in the Dorsal Striatum Revealed by Single-Cell RNA Sequencing and PatchSeq. *Cell Reports*, 24(8), 2179-2190.e7.
<https://doi.org/10.1016/j.celrep.2018.07.053>

Paylor, R., Hirotsune, S., Gambello, M. J., Yuva-Paylor, L., Crawley, J. N., & Wynshaw-Boris, A. (1999). Impaired Learning and Motor Behavior in Heterozygous Pafah1b1 (Lis1) Mutant Mice. *Learning & Memory*, 6(5), 521–537. <https://doi.org/10.1101/lm.6.5.521>

Saillour, Y., Carion, N., Quelin, C., Leger, P.-L., Boddaert, N., Elie, C., ... Bahi-Buisson, N. (2009). LIS1-Related Isolated Lissencephaly. *Arch Neurol.*, 66(8), 1007–1015.

Stouffer, M. A., Golden, J. A., & Francis, F. (2016). Neuronal migration disorders: Focus on the cytoskeleton and epilepsy. *Neurobiology of Disease, 92*(Part A), 18–45. <https://doi.org/10.1016/j.nbd.2015.08.003>

Traynelis, S. F., & Dingledine, R. (1988). Potassium-induced spontaneous electrographic seizures in the rat hippocampal slice. *Journal of Neurophysiology, 59*(1), 259–276. <https://doi.org/10.1152/jn.1988.59.1.259>

Vormstein-Schneider, D., Lin, J. D., Pelkey, K. A., Chittajallu, R., Guo, B., Arias-Garcia, M. A., ... Dimidschstein, J. (2020). Viral manipulation of functionally distinct interneurons in mice, non-human primates and humans. *Nature Neuroscience*. <https://doi.org/10.1038/s41593-020-0692-9>